Author:
Trilov, Stoyan M

Title:
Measurement of the branching fractions of semileptonic K+ decays at the NA62 experiment

Measurement of the branching fractions of semileptonic K^+ decays at the NA62 experiment

by

Stoyan Miroslavov Trilov

A thesis submitted to the University of Bristol for the degree of Doctor of Philosophy

in the
Faculty of Science
School of Physics

September 2019

Abstract

The NA62 experiment based at CERN aims to make a precision measurement of the ultra-rare kaon decay, $K^+ \to \pi^+ \nu\bar{\nu}$. To allow the safe operation of the NA62 CEDAR with hydrogen, several hardware and software modifications to the detector were completed. An assessment of the contribution of the current radiator gas, nitrogen, towards downstream detector rates was made, finding it to be comparable to that of beam related effects.

The ratios amongst the branching fractions of the semileptonic kaon decays, $K^+ \to \pi^0 \mu^+ \nu_\mu$ ($K_{\mu 3}$), $K^+ \to \pi^0 e^+ \nu_e$ (K_{e3}), and the hadronic decay $K^+ \to \pi^+ \pi^0$ ($K_{2\pi}$) were measured to be:

$$\frac{BF(K_{\mu 3})}{BF(K_{2\pi})} = 0.1610(2)_{\text{stat}}(10)_{\text{sys}}$$

$$\frac{BF(K_{e3})}{BF(K_{2\pi})} = 0.2431(3)_{\text{stat}}(9)_{\text{sys}}$$

$$\frac{BF(K_{\mu 3})}{BF(K_{e3})} = 0.6623(11)_{\text{stat}}(36)_{\text{sys}}$$

The precision of the results is limited by systematic effects, however the low statistical errors of the measurement demonstrate the successful application of the Barlow-Beeston method to NA62 data and simulation, and its potential for making precision measurements. With further undertaking, the systematic effects can be driven down, allowing the branching fractions measurement to reach potentially world-beating precision.

Declaration of authorship

I, Stoyan Trilov, declare that the work in this dissertation was carried out in accordance with the requirements of the University's Regulations and Code of Practice for Research Degree Programmes and that it has not been submitted for any other academic award. Except where indicated by specific reference in the text, the work is the candidate's own work. Work done in collaboration with, or with the assistance of, others, is indicated as such. Any views expressed in the dissertation are those of the author.

Signed: _____

Date: _____

Acknowledgements

I would like to thank my supervisor Helen Heath for the invaluable guidance and support throughout these last four years. Many thanks also go to Radoslav Marchevski and Matthew Moulson for the many fruitful discussions covering a range of topics.

To the class of 2015, and colleagues at CERN, thank you for making my PhD a fun and enjoyable experience. To Mum, Dad, Paolina, thank you, this would not have been possible without you.

Author's contribution

The design and implementation of the WinCC OA module described in section 2.12.2 is the result of my own work. The module from section 2.12.2 is based on an already existing component, however all modifications and enhancements are my own work.

I was not involved in the design or installation of the KTAG or the rest of the detectors described in chapter 2, however I installed the CEDAR hardware interlocks discussed in section 3.3.

The event selection described in 4.1 is my own work, however it is based around algorithms and tools, developed by the NA62 collaboration, and available in the NA62 software framework. The analyses presented in section 3.4, chapters 5 and 6, are the products of my own work.

No other qualifications have been achieved with the work reported in this thesis.

Contents

List of Figures

List of Tables

Abbreviations

BF	Branching fraction
CERN	European Organisation for Nuclear Research
CDA	Closest distance of approach
CEDAR	Čerenkov differential counter with achromatic ring focus
CHANTI	Charged anti-coincidence detector
CHOD	Charged particle hodoscope
CKM	Cabbibo-Kobayasji-Maskawa
DCS	Detector control system
DCR	Dry contact relay
FV	Fiducial volume
FSM	Finite state machine
GCS	Gas control system
GTK	Gigatracker
HASC	Hadronic sampling calorimeter
IRC	Intermediate ring calorimeter
KTAG	Kaon tagger
LAV	Large angle veto
LEL	Lower explosive limit
LKr	Liquid krypton calorimeter
LOTP	L0 trigger processor
LSF	Least squares fit
MC	Monte Carlo
PDG	Particle data group
PDU	Power distribution unit
PET	Polyethylene terephthalate

PLC	Programmable logic controller
PoT	Protons on target
PM	Photo multipliers
$\pi\nu\bar{\nu}$	$K^+ \to \pi^+\nu\bar{\nu}$
RICH	Ring imaging Čerenkov detector
RO	Readout
SM	Standard model
SAC	Small angle calorimeter
SAV	Small angle veto
SiPM	Silicon photomultipliers
SNMP	Simple network management protocol
SPS	Super proton synchrotron
TDAQ	Trigger and data acquisition
UEL	Upper explosive limit
WLS	Wavelength shifting

Chapter 1

Introduction

Interactions between elementary particles are currently best described by the Standard Model (SM), a theoretical framework developed over the last fifty years. While the Standard Model has had many successes and has been tested to high precision, there are a number of experimental observations which can not be accommodated within it, e.g. the oscillation of neutrinos [1] [2] and the matter-antimatter asymmetry of the universe [3] [4]. Such findings suggest that the SM is not the whole picture. Any experimental evidence which deviates from the prediction given by the SM can give clues to the physics which could lie beyond it.

1.1 CKM unitarity and V_{us}

The coupling between quarks in the SM is governed by the Cabbibo-Kobayasji-Maskawa (CKM) matrix [5], V_{CKM}:

$$\begin{pmatrix} d' \\ s' \\ b' \end{pmatrix} = V_{CKM} \begin{pmatrix} d \\ s \\ b \end{pmatrix} = \begin{pmatrix} V_{ud} & V_{us} & V_{ub} \\ V_{cd} & V_{cs} & V_{cb} \\ V_{td} & V_{ts} & V_{tb} \end{pmatrix} \begin{pmatrix} d \\ s \\ b \end{pmatrix}. \tag{1.1}$$

Within the SM, V_{CKM}, is unitary, hence it must satisfy the relation:

$$V^{\dagger}V = I, \tag{1.2}$$

where I is the identity matrix, and $V^{\dagger}$ is the Hermitian conjugate of V. Any experimental observation of departure from unitarity can serve to constrain new physics scenarios [6]. The CKM unitarity is currently best constrained by the first row sum [7] [8] [9]:

$$|V_{ud}|^2 + |V_{us}|^2 + |V_{ub}|^2 = 1 + \Delta_{CKM}, \tag{1.3}$$

where Δ_{CKM} serves to parameterise the deviation from unitarity.

The most precise value of $|V_{ud}|$ comes from measurements of superallowed nuclear beta-decays ($0^+ \rightarrow 0^+$) [10]:

$$|V_{ud}| = 0.97420 \pm 0.00021. \tag{1.4}$$

The parameter $|V_{us}|$ can be extracted from kaon decays, hyperon decays, and tau decays. Historically, most previous measurements have used semileptonic kaon decays, $K \rightarrow \pi l \nu$, where $l = e, \mu$. This set of decays is known as K_{l3} decays.

The two most precise measurements of V_{us} come from K_{l3} decays, where the values from several different modes are averaged together, and from the ratio of the decay rates for $K \rightarrow \mu\nu(\gamma)$ and $\pi \rightarrow \mu\nu(\gamma)$. The different measurements from the K_{l3} decays used in the calculation are listed in table 1.1 [11].

Decay mode	$\lvert V_{us}\rvert f_+(0)$
$K^{\pm}e3$	0.2171 ± 0.0008
$K^{\pm}\mu3$	0.2170 ± 0.0011
$K_L e3$	0.2163 ± 0.0006
$K_L \mu3$	0.2166 ± 0.0006
$K_S e3$	0.2155 ± 0.0013
Average (including correlations)	0.2165 ± 0.0004

Table 1.1: The values, and their average, of the product $|V_{us}|f_+(0)$ which are used for the calculation of $|V_{us}|$. $f_+(0)$ is the form factor at zero momentum transfer for the lepton system.

Using, $f_+(0) = 0.9704 \pm 0.0032$, as given by lattice QCD calculations [12], and the average from table 1.1, one obtains $|V_{us}|$ as

$$|V_{us}| = 0.2231 \pm 0.0008. \tag{1.5}$$

The ratio between radiative kaon and pion decays gives $|V_{us}|$ as [7]:

$$|V_{us}| = 0.2253 \pm 0.0007. \tag{1.6}$$

Combining 1.5 and 1.6 results in a value of $|V_{us}|$:

$$|V_{us}| = 0.2243 \pm 0.0005. \tag{1.7}$$

The magnitude of $|V_{ub}|^2$ is around three orders of magnitude lower than that of $|V_{ud}|^2$ and $|V_{us}|^2$, meaning its contribution in equation 1.3 is negligible. Considering this fact, and the values from 1.4 and 1.7, one obtains a value for $1 + \Delta_{CKM}$ of

$$|V_{ud}|^2 + |V_{us}|^2 + |V_{ub}|^2 = 1 + \Delta_{CKM} = 0.9994 \pm 0.0004 \pm 0.0002, \tag{1.8}$$

where the first error comes the uncertainty of $|V_{ud}|^2$, and the second is from $|V_{us}|^2$. If the scale factors stemming from the differences between the two values used to calculate $|V_{us}|$ are accounted for, the uncertainty from $|V_{us}|$ climbs to 0.0004 [7].

The tension between the values of $|V_{us}|$ extracted from K_{l3} and $K \to \mu\nu(\gamma)/\pi \to \mu\nu(\gamma)$ decays motivates reducing the error on $|V_{us}|$ in order to allow a better comparison between the two methods of calculation. This could eventually lead to a more precise final value of $|V_{us}|$, constraining CKM unitarity even further.

The agreement between the values of $|V_{us}|f_+(0)$ in table 1.1 could be improved. The uncertainties in the $K^\pm$ and K_S measurements are dominated by the error on the measurements of the branching fractions. Improving the precision on the K_{l3} decay rates could help resolve the inconsistencies present within the $K^\pm$ dataset.

To extract $|V_{us}|$ from semileptonic decays of charged kaons, one can use the relation for the K_{l3} decay rate, $\Gamma_{K_{l3}}$ [13]:

$$\Gamma_{Kl3} = \frac{G_F^2 m_K^5}{192\pi^3} C_K^2 S_{EW} \left(|V_{us}| f_+^{K^0\pi^-}(0)\right)^2 \cdot I_{Kl} \cdot \left(1 + \delta_{EM}^{Kl} + \delta_{SU(2)}^{K\pi}\right)^2, \tag{1.9}$$

where G_F is the Fermi constant, m_K is the kaon mass, C_K is a Clebsch-Gordan coefficient (1 for K^0 and $\frac{1}{\sqrt{2}}$ for $K^\pm$), S_{EW} is the short-distance electroweak correction, $f_+^{K^0\pi^-}(0)$ is the form factor zero momentum transfer for $K^0 \to \pi^-$, I_{Kl} is the phase-space integral, δ_{EM}^{Kl} is electromagnetic corrections, and $\delta_{SU(2)}^{K\pi}$ is the isospin breaking correction. The Fermi constant, G_F, is determined from muon decays. The hadronic matrix element can be written in terms of form factors as [13]:

$$\langle \pi(p_\pi)|\bar{s}\gamma_\mu u|K(p_k)\rangle = (p_\pi + p_K)_\mu f_+^{K\pi} + (p_K - p_\pi)_\mu f_-^{K\pi}(t), \tag{1.10}$$

where $t = (p_K - p_\pi)^2 = (p_l + p_\nu)^2$.

$f_+(t)$ and $f_0(t)$ are the vector and scalar form factors respectively. The vector form factor represents the P-wave projection of the crossed channel matrix element, $\langle 0|\bar{s}\gamma^\mu u|K\pi\rangle$. The S-wave projection is given by the scalar form factor, and can be expressed as [13]:

$$f_0(t) = f_+(t) + \frac{t}{m_K^2 - m_\pi^2} f_-(t). \tag{1.11}$$

Due to the fact that $f_+^{K^-\pi^0}(0)$ cannot be determined experimentally, it is convenient to factorise it out, as done in equation 1.9, and write expressions for the normalised factors:

$$\bar{f_+}(t) = \frac{f_+(t)}{f_+(0)}, \quad \bar{f_0}(t) = \frac{f_0(t)}{f_+(0)}, \quad \bar{f_+}(0) = \bar{f_0}(0) = 1, \tag{1.12}$$

where we adopt the notation $f_+(0) \equiv f_+^{K^-\pi^0}(0)$. Averaged values of $f_+(0)$ from lattice QCD calculations from the FlaviaNet Lattice Averaging Group (FLAG) give a form factor value of 0.9704 ± 0.0032 [12].

The phase-space integral, I_{Kl}, is calculated by evaluating the expression [8]:

$$I_{Kl} = \int_{m_l^2}^{t_{max}} \frac{1}{m_K^8} \lambda^{3/2} \left(1 + \frac{m_l^2}{2t}\right) \left(1 - \frac{m_l^2}{2t}\right)^2 \cdot \left(\bar{f_+}^2(t) + \frac{3m_l^2 \Delta_{K\pi}^2}{(2t + m_l^2)\lambda} \bar{f_0}^2(t)\right) dt, \tag{1.13}$$

where $\lambda = \left[t - (m_K + m_\pi)^2\right]\left[t - (m_K - m_\pi)^2\right]$, $t_{\max} = (m_K - m_\pi)^2$, and $\Delta_{K\pi} = m_K^2 - m_\pi^2$. The computation of I_{Kl} requires knowledge of the normalised factors from equation 1.12. These can be extracted from fits to the experimental distributions of K_{l3} decays, where the energy of the lepton is plotted against the energy of the pion [14].

Since the same normalisation factor, $f_+^{K^0\pi^-}(0)$, is factored out in equation 1.9 for both charged and neutral K_{l3} decays; we require the terms, $\delta_{SU(2)}^{K\pi}$, which take the values of:

$$\delta_{SU(2)}^{K^0\pi^-} = 0, \quad \delta_{SU(2)}^{K^+\pi^0} = \frac{f_+^{K^+\pi^0}(0)}{f_+^{K^0\pi^-}(0)} - 1 \tag{1.14}$$

This isospin-breaking correction can be calculated via the means of chiral perturbation theory [15].

The corrections arising from the long-distance electromagnetic contributions to the fully inclusive $K_{l3(\gamma)}$ decay rates are included via the term, δ_{EM}^{Kl}. The values for δ_{EM}^{Kl} are calculated to leading non-trivial order in chiral effective theory, using a fully inclusive prescription of real photon emission [16]. The term S_{EW} represents a short distance electroweak correction to the charged current process, common to $K^\pm$ and K^0 decays [17].

1.2 $K^+ \to \pi^+\nu\bar{\nu}$ at NA62

The NA62 experiment at CERN was designed and built to measure the branching fraction of the ultra rare decay, $K^+ \to \pi^+\nu\bar{\nu}$ (referred to as $\pi\nu\bar{\nu}$ throughout this work) to 10% precision [18]. The theoretical prediction for the SM branching fraction is $(8.4\pm1.0)\times10^{-11}$ [19], whereas the experiment measurement stands at $(17.3^{+11.5}_{-10.5}\times10^{-11})$ [20]. The gap between the precision of the theoretical prediction and the experimental measurement is what drives the experiment. To achieve a measurement with similar precision to that of the prediction, NA62 plans to collect 100 $\pi\nu\bar{\nu}$ events by recording 10^{13} protons on target (PoT) with a signal-to-background ratio of around 10:1. For this purpose, the experiment must achieve background suppression of the order of 10^8 against the main K^+ decay modes listed in table 1.2 [7]. There are four main ways in which this is done: kinematic rejection, particle identification redundancy, excellent timing resolution, and a hermetic photon veto [21].

K^+ decay mode	Shorthand	Branching fraction
$K^+ \to \mu^+\nu_\mu$	$K_{\mu2}$	0.6356 ± 0.0011
$K^+ \to \pi^+\pi^0$	$K_{2\pi}$	0.2067 ± 0.00008
$K^+ \to \pi^+\pi^+\pi^-$	$K_{3\pi}$	0.05583 ± 0.00024
$K^+ \to \pi^0 e^+\nu_e$	K_{e3}	0.0507 ± 0.0004
$K^+ \to \pi^0\mu^+\nu_\mu$	$K_{\mu3}$	0.03352 ± 0.00033
$K^+ \to \pi^+\pi^0\pi^0$	$K_{3\pi0}$	0.01760 ± 0.00023
$K^+ \to e^+\nu_e$	K_{e2}	$(1.582 \pm 0.007) \times 10^{-5}$

Table 1.2: The branching fractions of the main K^+ decay modes, together with the shorthand notation for each decay channel.

The dataset collected by NA62 also allows for a rich physics programme beyond $\pi\nu\bar{\nu}$, which includes precision measurements of the branching fractions of the two decays: $K^+ \to \pi^0 e^+\nu_e$ and $K^+ \to \pi^0\mu^+\nu_\mu$, in the context of extracting $|V_{us}|f_+(0)$. The ratio of these two branching fractions would also serve to test $e-\mu$ universality. The measurement of the K_{e3} and $K_{\mu3}$ branching fractions forms the main impetus behind the work presented in this thesis.

The experimental setup of NA62 is described in chapter 2, where details of the beam, the trigger and data acquisition (TDAQ), and the detector and its control system (DCS) are given.

The kaon tagger (KTAG) detector is used in NA62 to identify incoming beam kaons. The detector is composed of a Čerenkov differential counter with achromatic ring focus (CEDAR) [22], which is traversed by the beam, producing Čerenkov radiation [23]. The Čerenkov light is then focussed, and collected by a set of photomultipliers. The CEDAR is currently filled and operated with nitrogen. The effect of the multiple scattering caused by the N_2, and the modifications of the CEDAR allowing it to operate safely with hydrogen are discussed in chapter 3.

The strategy to measure the branching fractions of the two K^+_{l3} decays is outlined in chapter 4, which gives details of the event selection and the branching fraction extraction method. Chapter 5 discusses the data and simulation samples used for the analysis, and the agreement between the two. The results of the branching fraction measurement including systematic effects are discussed in chapter 6.

Chapter 2

NA62 experimental setup

NA62 was built to perform a 10% measurement of the branching fraction of the ultra rare decay, $K^+ \to \pi^+\nu\bar{\nu}$, $BF = (8.4 \pm 1.0) \times 10^{-11}$ [19]. The signature of a $K^+ \to \pi^+\nu\bar{\nu}$ decay is a single π^+ matched to an incoming K^+. The experiment must achieve $\mathcal{O}(10^{12})$ background suppression against the other kaon decay modes, that are listed in table 1.2. To achieve its goal, NA62 adopted four guiding principles for the design of the experiment:

- excellent kinematic resolution;
- complementary particle identification (PID) systems;
- hermetic photon vetoes;
- precise timing.

The experimental setup of NA62 is described in detail in reference [21]. This chapter is intended to give an overview of the different components which together compose the NA62 experiment. The detector layout is illustrated in figure 2.1. The hadron beam used in the experiment is produced using a beryllium target ($z = 0$), and then propagates through the experiment in the positive z direction. The KTAG and Gigatracker (GTK) detectors measure the beam composition and direction, and are followed by the

approximately 60 m long fiducial volume (FV), where around 10% of kaons decay. Decay products are measured by a set of detectors downstream of the FV, which provide tracking, particle identification, and photon detection.

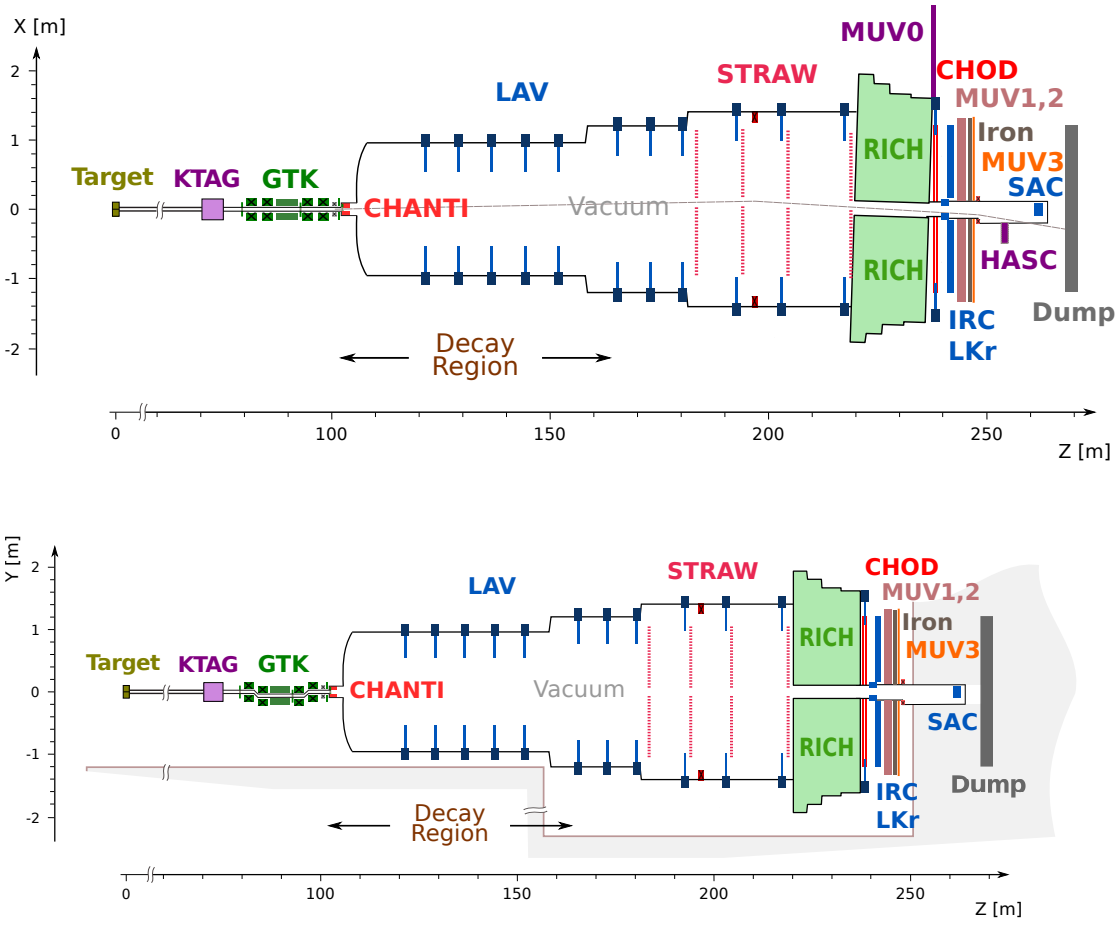

Figure 2.1: A schematic drawing of the NA62 detector in the x (horizontal) and y (vertical) views. The beam travels through the experiment in the $+z$ direction, from [21].

The excellent kinematic resolution allows the suppression of background originating from $K_{2\pi}$ and $K_{\mu 2}$ decays. The main kinematic variable in the experiment is the missing-mass, defined as

$$m^2_{miss} = (P_K - P_\pi)^2,$$

where P_K is the kaon four momentum as measured by the beam spectrometer, and P_π is the four momentum of the charged track, measured by the STRAW spectrometer under the π^+ mass hypothesis. The spectrum of missing-mass for $K^+ \to \pi^+\nu\bar{\nu}$ and the main decay modes is shown in figure 2.2a. Two m^2_{miss} signal regions were defined, indicated

by the labels region I and II in figure 2.2a. The regions were chosen to avoid the main peaks of $K_{\mu 2}$ and $K_{2\pi}$ modes. The knowledge of both the parent and daughter particles' momenta and directions results in a m^2_{miss} resolution of around 1×10^{-3} GeV^2/c^4. The kinematic background suppression is $\mathcal{O}(10^4)$.

The PID systems are used to suppress background originating from $K_{\mu 2}$ decays. NA62 employs two PID systems. One is based around calorimeters including the liquid krypton electromagnetic calorimeter LKr, two hadron calorimeters MUV1 and MUV2, and a fast muon veto MUV3. Pion/muon separation is also provided by a ring-imaging Čerenkov detector (RICH). The rejection power provided by each of the PID techniques reaches the level of 10^8.

Photon vetoes are implemented for the rejection of the second most common K^+ mode, $K^+ \to \pi^+\pi^0$, which presents a potential background to $\pi\nu\bar{\nu}$ if the photons from the π^0 leave the experiment undetected. To avoid this, the NA62 experiment employs a hermetic photon veto system able to detect photons emitted at angles between 0 and 50 mrad. Photons produced at angles above 8.5 mrad are seen by the twelve stations of the large angle veto (LAV), whereas medium angle photons are detected by the LKr. The intermediate ring and small angle calorimeters (IRC and SAC) provide photon detection for photons emitted at angles below 1 mrad. The complete veto system provides a π^0 rejection factor of around 10^7.

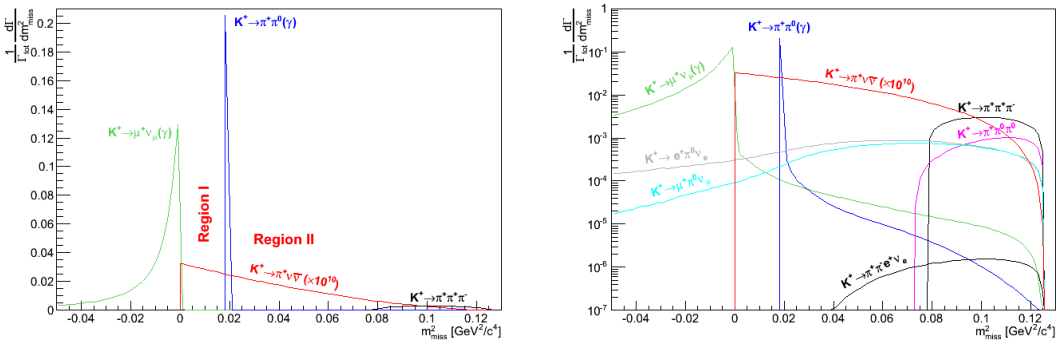

(a) (b)

Figure 2.2: Distribution of the main kinematic variable, $m^2_{miss} = (P_K - P_\pi)^2$, for the NA62 golden channel, $K^+ \to \pi^+\nu\bar{\nu}$ and the main K^+ decay modes; (a) linear scale, (b) log scale, from [21].

NA62 is a high intensity environment with a nominal beam rate of 750 MHz, equating to 5 MHz K^+ decay rate in the fiducial volume. The effective matching of the incoming K^+ to the daughter π^+ requires precise timing. The kaon time comes from the KTAG and GTK detectors, both of which have time resolutions below 100 ps. The charged pion is timestamped with similar precision by the RICH. These detector elements are described in more detail in the rest of this chapter.

2.1 Beam

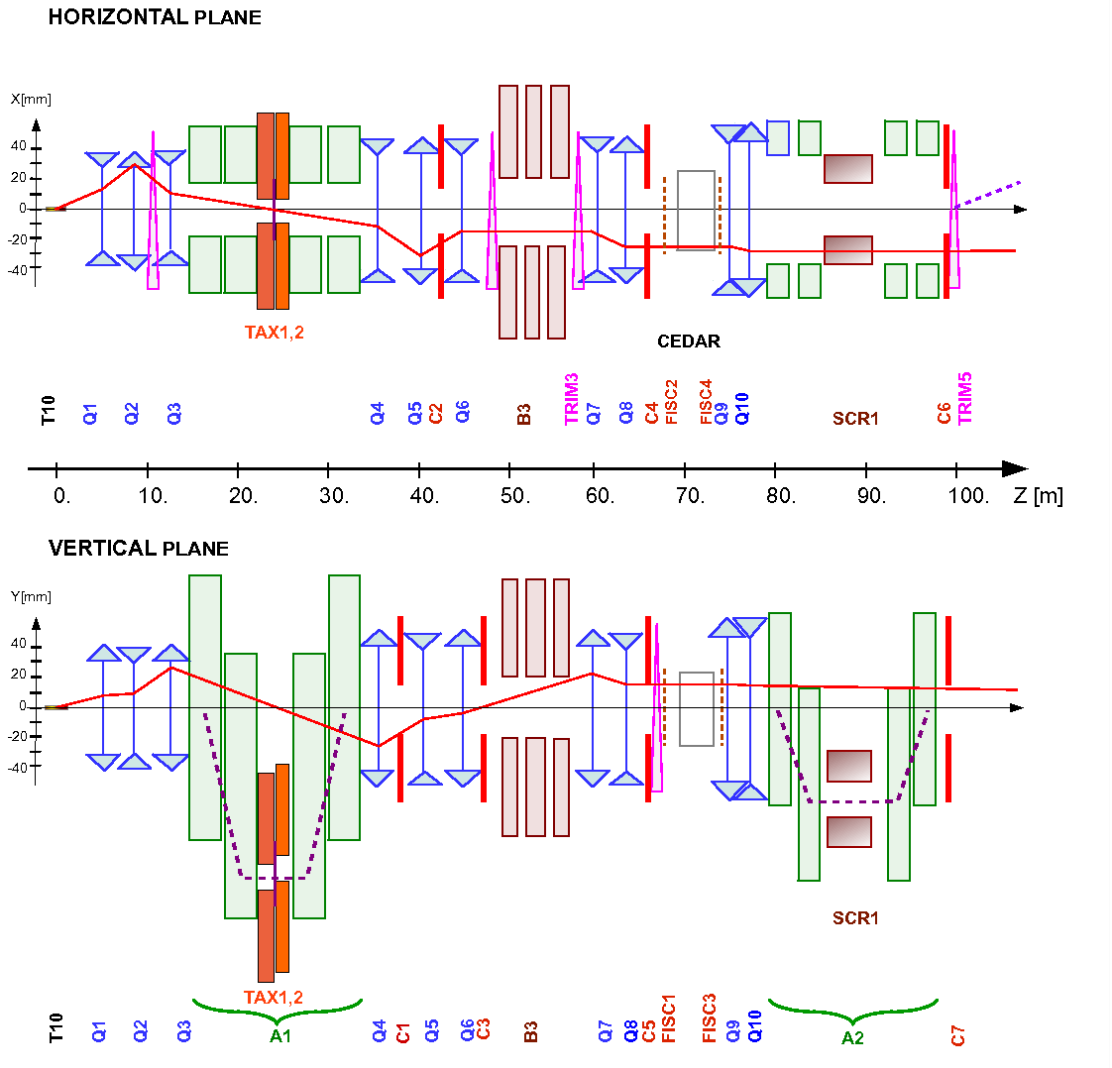

Figure 2.3: A schematic drawing of the secondary hadron beam optics in the x (top) and y (bottom) views, from [21].

The NA62 beam is derived by impinging 400 GeV/c protons extracted from the CERN Super Proton Synchrotron (SPS) onto a cylindrical Beryllium target (T10). A schematic of the hadron beam optics is shown in figure 2.3. The resulting secondary hadron beam is composed of around 6% kaons, 22% protons, and 70% pions. A series of quadrupole magnets (Q1, Q2, Q3 in figure 2.3) together with the achromat magnet, A1, select particles of 75 GeV/c momentum with 1% r.m.s. deviation. The achromat magnet consists of four dipole magnets, where the first two magnets deflect the beam in the vertical direction, and the following two dipoles return it to its original axis. Two beam dump units (TAX1 and TAX2) placed between the two sets of dipoles make the momentum selection. After passing through A1 and the two TAXes, the beam is refocused by the quadrupole triplet Q4, Q5, Q6. Following this, are three 2m long dipole magnets (B3) used to sweep positive and negative muons away from the beam. Just before entering the CEDAR, the beam is rendered parallel by the Q7 and Q8 magnets, and cleaned by the collimators C4 and C5.

The momentum measurement of the beam is performed after its exit from the CEDAR by the Gigatracker, which consists of three silicon pixel stations, as shown in the schematic in figure 2.4. The first GTK station (GTK1) is preceded by the relatively weakly focusing magnets Q9 and Q10. After GTK1, the first two magnets of the second achromat (A2) serve to deflect the beam by 60 mm in the negative y direction. The beam then traverses the second GTK station (GTK2). The second part of the A2 magnet returns the beam to its original axis. Just before the final GTK station (GTK3), a dipole magnet (TRIM5) deflects the beam by +1.2 mrad in the x direction in order to steer the beam into the LKr aperture following the kick from the STRAW spectrometer magnet (MNP33). The layout of these components is shown in figure 2.5.

2.2 KTAG

The first element of the NA62 detector along the beam line is the KTAG [24], designed to timestamp K^+ which make up 6% of beam particles. The KTAG is based around a Čerenkov differential counter with achromatic ring focus (CEDAR) [22], which is a

vessel with volume of 1 m^3 filled with nitrogen gas. As beam particles travel along the CEDAR, they emit Čerenkov light, which is reflected and focused towards the upstream plane of the detector by an optical setup inside the gas volume. A diaphragm, also inside the CEDAR volume, blocks all light that does not originate from kaons. The photons that do make it past the diaphragm exit the CEDAR are directed onto an array of photo multipliers (PMs) divided into eight octants, as shown in figure 2.6. Each octant is instrumented with 48 PMs, resulting in a total of 384 channels. The KTAG has time resolution of less than 100 ps, and K^+/π^+ mis-identification probability of the order of 10^{-4}.

The gas type and pressure inside the CEDAR can be varied depending on the momentum and mass of the particle to be identified. Putting hydrogen instead of nitrogen inside the CEDAR can in principle allow K^+ identification while reducing the total detector thickness from $3.5 \times 10^{-2} X_0$ to $7 \times 10^{-3} X_0$, thereby reducing multiple scattering of the beam. This operation however is expected to degrade the kaon identification performance and time resolution of the detector. The use of H_2 also brings certain operational hazards

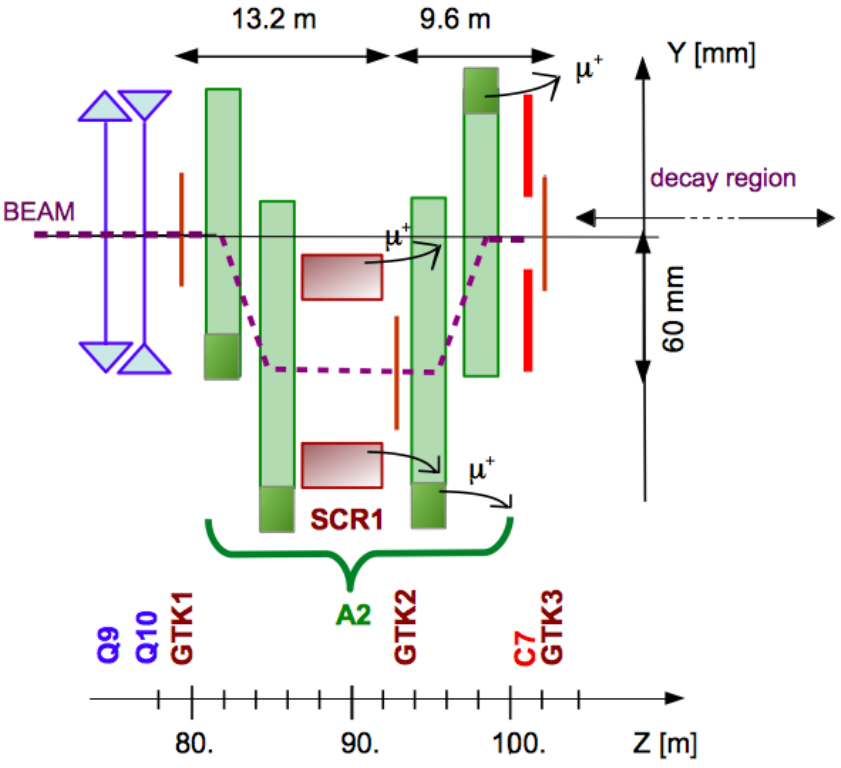

Figure 2.4: A schematic of the beam transport configuration around the Gigatracker spectrometer, from [21].

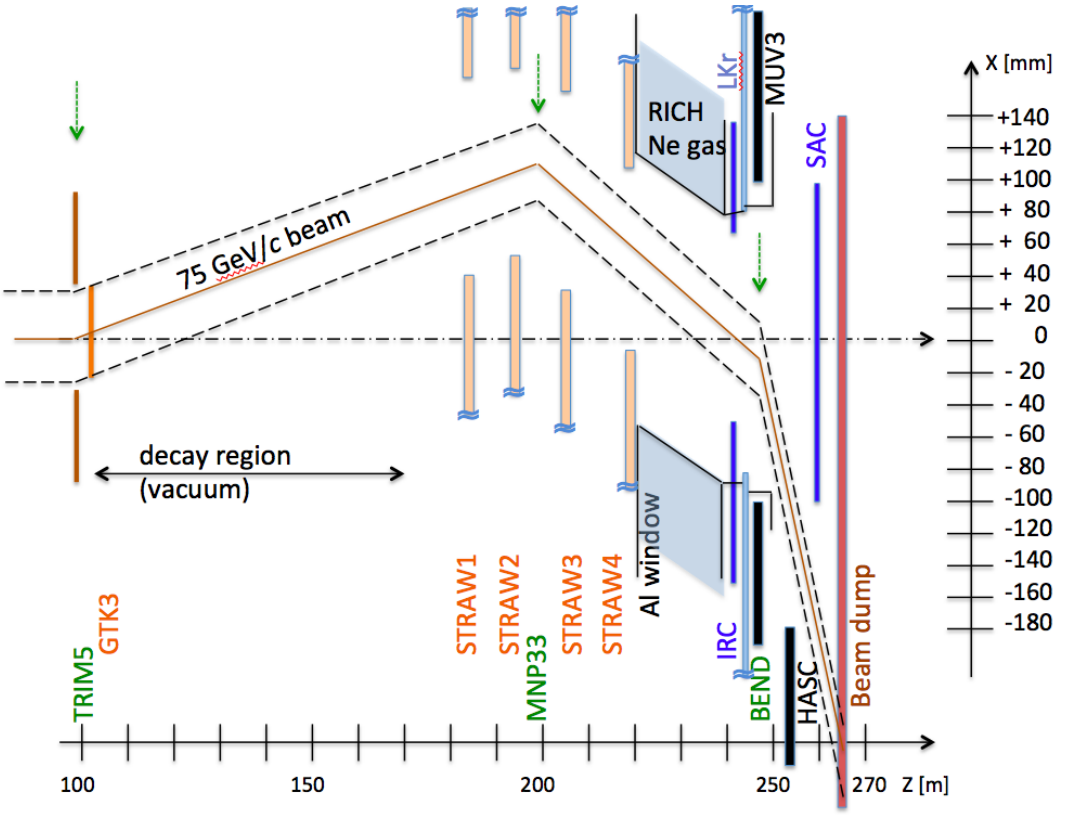

Figure 2.5: Cartoon of the detector layout and beam trajectory after the GTK. The magnet TRIM5 imposes a 1.2 mrad deflection $+x$ direction, which is followed by the MNP33 magnet's 3.6 mrad kick in $-x$ direction. The BEND magnet just before the beam dump imparts a deflection of -13.2 mrad in x, from [21].

due to the explosive nature of the gas. The issue of CEDAR H_2 operation is discussed in more detail in chapter 3.

2.3 Gigatracker

The measurement of the direction and momentum of beam particles is performed by the beam spectrometer, or Gigatracker. The detector is composed of three silicon pixel stations. Each station has 200×90 pixels, each with size of 300×300 μm, resulting in an overall transverse size of 62.8×27 mm^2. Figure 2.7 shows photographs of an assembled GTK station. The first GTK station is placed after the KTAG, and it is followed by the first half of an achromat, which directs the beam in the negative y direction by 60 mm. The deviated beam then traverses the second GTK station, and is returned to its original axis by the second part of A2, figure 2.8. The momentum resolution of the beam

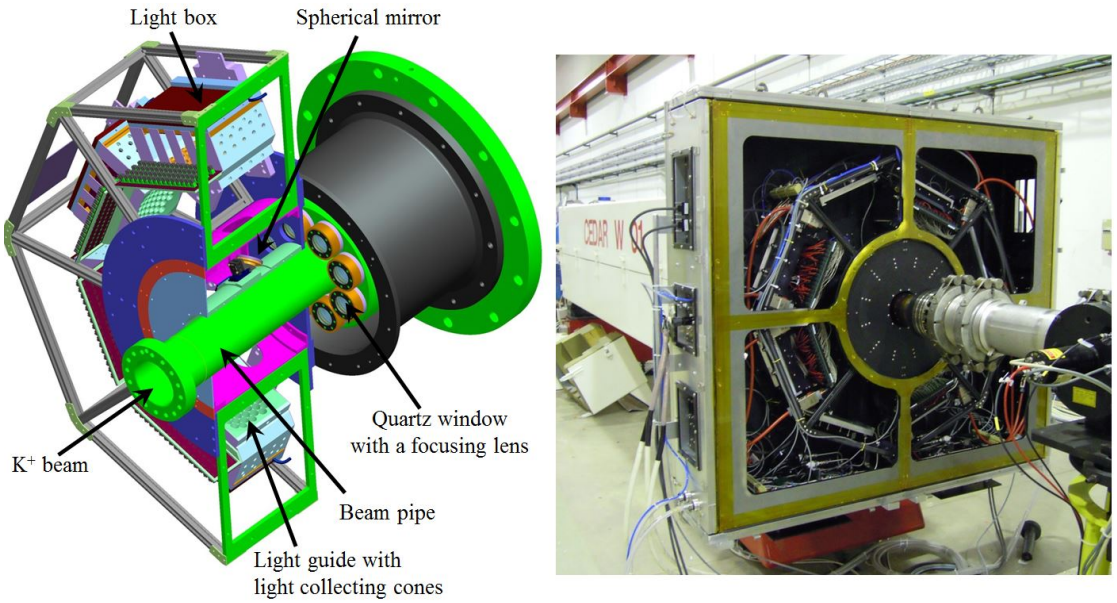

Figure 2.6: A schematic drawing of the KTAG upstream nose is shown on the left, with a photo of the nose and the CEDAR vessel on the right, from [21].

tracker is $0.2\% \cdot P$ GeV/c. with angular resolution of 16 μrad. The time resolution of the detector is around 200 ps.

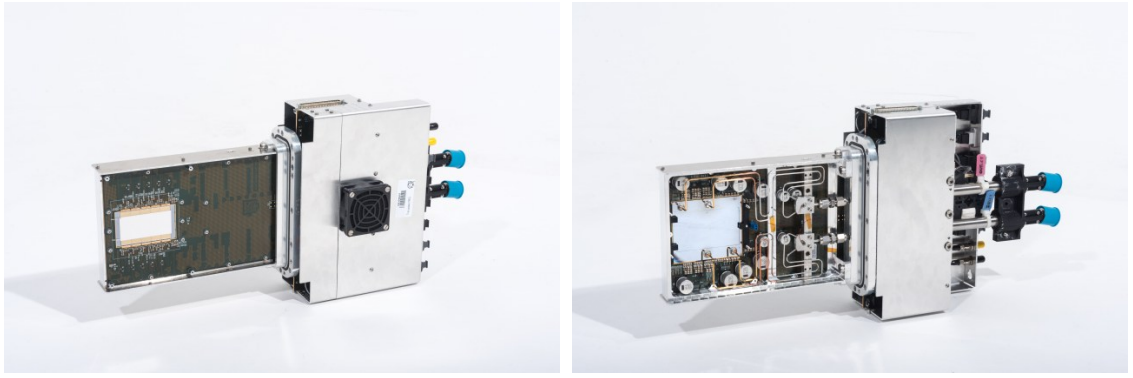

(a) A photo of an assembled GTK station, sensor side.

(b) A photo of an assembled GTK station, cooling side

Figure 2.7: The sensor (a) and cooling (b) sides of a GTK station are pictured, from [21].

2.4 Charged anti-coincidence detector (CHANTI)

The CHANTI detector is placed 28 mm downstream of the last GTK station, and is designed to veto particles originating from inelastic interactions in GTK3. The space

between each successive station roughly doubles to provide hermetic coverage for particles coming from GTK3. Products from such processes can enter the fiducial region and mimic the $K^+ \to \pi^+\nu\nu$ signal. The detector is also sensitive to the muon halo that accompanies the beam. The area of each station is 300×300 mm^2 with a central rectangular gap to allow the passage of the beam pipe, as can be seen in the photographs in figure 2.9. The detector is composed of six stations, each one of which has an x and y view, where forty-eight scintillating triangular bars make up each view. The scintillator bars are read out by fast wavelength shifting (WLS) fibres coupled to silicon photomultipliers (SiPM).

2.5 STRAW spectrometer (STRAW)

The direction and momentum of charged tracks is measured by the magnetic spectrometer (STRAW). The main building block of the STRAW is a straw tube, which is essentially a drift chamber. Each straw is 2160 mm long, with a diameter of 9.82 mm, and is made of 6 μm thick polyethylene terephthalate (PET). The spectrometer is composed of four chambers, with each chamber having four views, offset with respect to one another by 45°, as indicated in figure 2.10. Each view has four planes, each made up of 448 tubes, resulting in 7168 straws in total. The MNP33 magnet is located between the first two and last two stations, as shown in figure 2.5, and it provides a magnetic field of 0.36 T, resulting in a transverse momentum kick of 270 MeV/c. The momentum resolution of the STRAW spectrometer for a charged track is:

$$\frac{\sigma_P}{P} = 0.005\% \cdot P[\text{GeV/c}] \oplus 0.30\%,$$

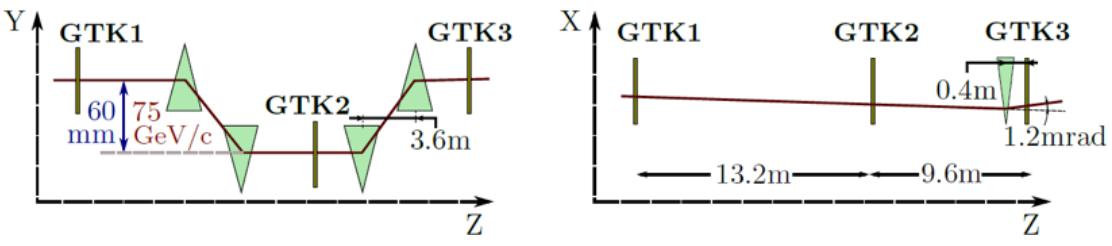

Figure 2.8: Schematic view of the three GTK stations which are interspaced by the two parts of the A2 magnet, left: x view, right: y view, from [21].

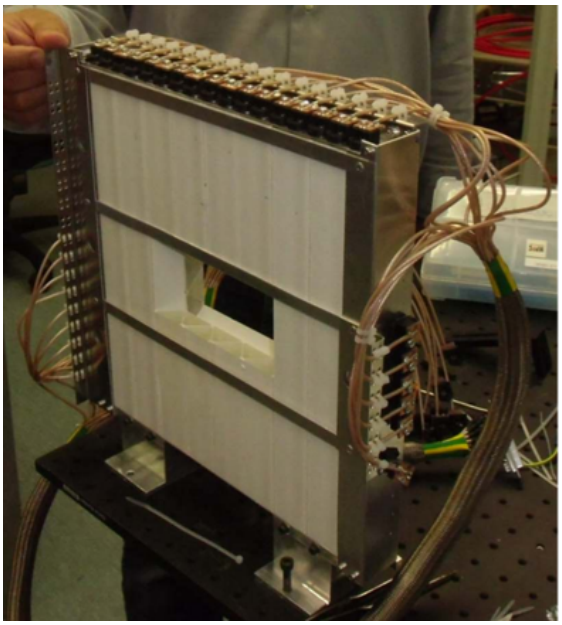

(a) A photo of an assembled CHANTI station with the scintillator bars clearly visible.

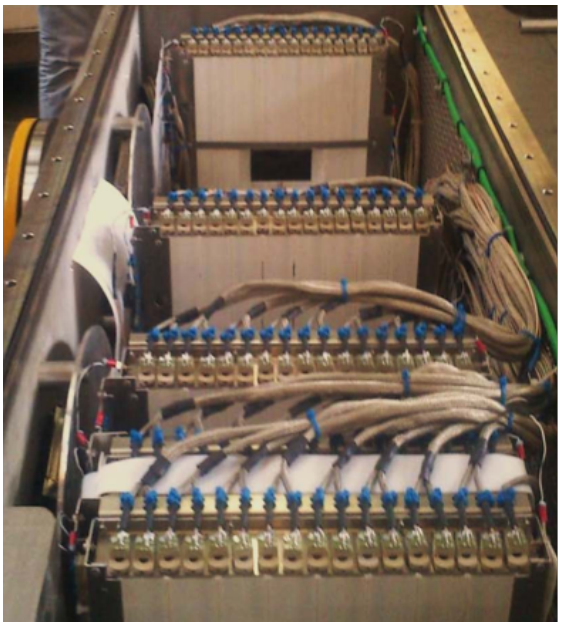

(b) A photograph of the CHANTI vessel which houses the six CHANTI stations and GTK3.

Figure 2.9: Photographs of a CHANTI station (a), and the vessel in which they are housed in (b), from [21].

where the angular resolution is 60 μrad for a 10 GeV/c track, and reduces to 20 μrad for a 50 GeV/c particle.

2.6 Charged particle hodoscopes (CHOD)

NA62 uses a pair of charged hodoscopes, NA48-CHOD and CHOD, to provide downstream time information for charged tracks. This timing information is used in the NA62 trigger, as well as in offline analysis. The NA48-CHOD detector from comes the previous kaon experiment NA48, and employs two planes of scintillator strips, oriented in the x and y directions. The detector is placed downstream of LAV12, and it provides the control trigger of the NA62 experiment.

The CHOD, also known as NewCHOD, has been newly constructed and optimised for NA62. It is composed of a single plane of scintillating tiles, employing a finer tile segmentation near the beam pipe in order to accommodate the higher hit rate. The tile configuration of the CHOD allows for more complex trigger conditions based on the impact position of the track.

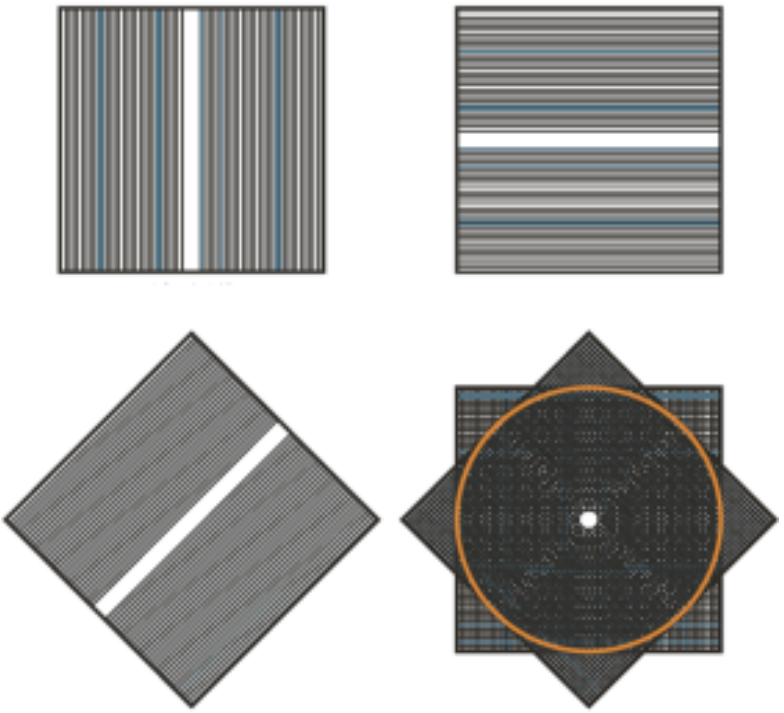

Figure 2.10: A schematic view of the different orientations of a plane of straw tubes, from [21].

2.6.1 NA48-CHOD

The two NA48-CHOD planes are each made of sixty-four 20 mm thick scintillating slabs, as shown in figure 2.11. The slabs have a width of 65 mm close to the beam pipe, and 99 mm elsewhere. Each scintillator is read out at one end by a Plexiglas light guide and a photomultiplier. The hits from the x and y plane provide two independent measurement of the particle crossing time, resulting in a time resolution of around 200 ps. The NA48-CHOD minimum bias trigger condition is based the coincidence of two hits within a 6.25 ns window.

2.6.2 CHOD

An array of one hundred and fifty-two 30 mm tiles make up the CHOD counter active area, with each tile being 108 mm high, with the exception of the 12 tiles near the beam pipe, figure 2.12. Most of the tiles have a width of 134 mm or 268 mm. The scintillation light from each tile is collected and read by WLS fibres coupled to silicon

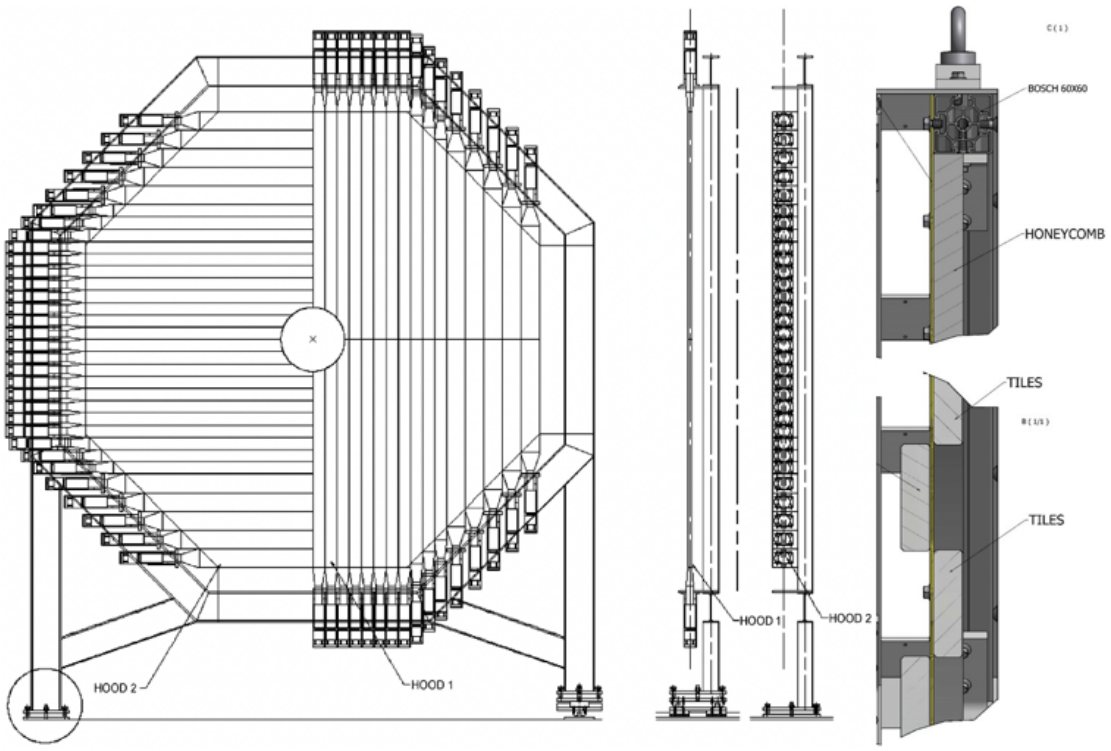

Figure 2.11: A schematic drawing of the NA48-CHOD detector with its horizontal and vertical planes clearly visible, from [21].

photomultipliers. The CHOD provides trigger information (see section 2.11) indicating the crossing of single and multiple particles.

2.7 Photon vetoes

The photon veto system of NA62 is designed to provide hermetic coverage for detection of photons originating from neutral pions, themselves mainly coming from $K^+ \to \pi^+\pi^0$, as well as $K^+ \to \pi^+\pi^0\pi^0$, decays inside the fiducial volume. To achieve this, separate sub-detectors are used to detect photons emitted at large, medium, and small angles. Photons emitted at angles in the range 8.5-50 mrad are detected by the twelve stations of the LAV, photons produced between 1-8.5 mrad are seen by the main electromagnetic calorimeter (LKr), which is filled with liquid krypton. The LKr can also be used to reconstruct π^0s coming from K^+ decays, if both of the photons are in the detector acceptance. Finally, photons at angles smaller than 1 mrad are caught by the IRC and the (SAC), which compose the small angle veto (SAV).

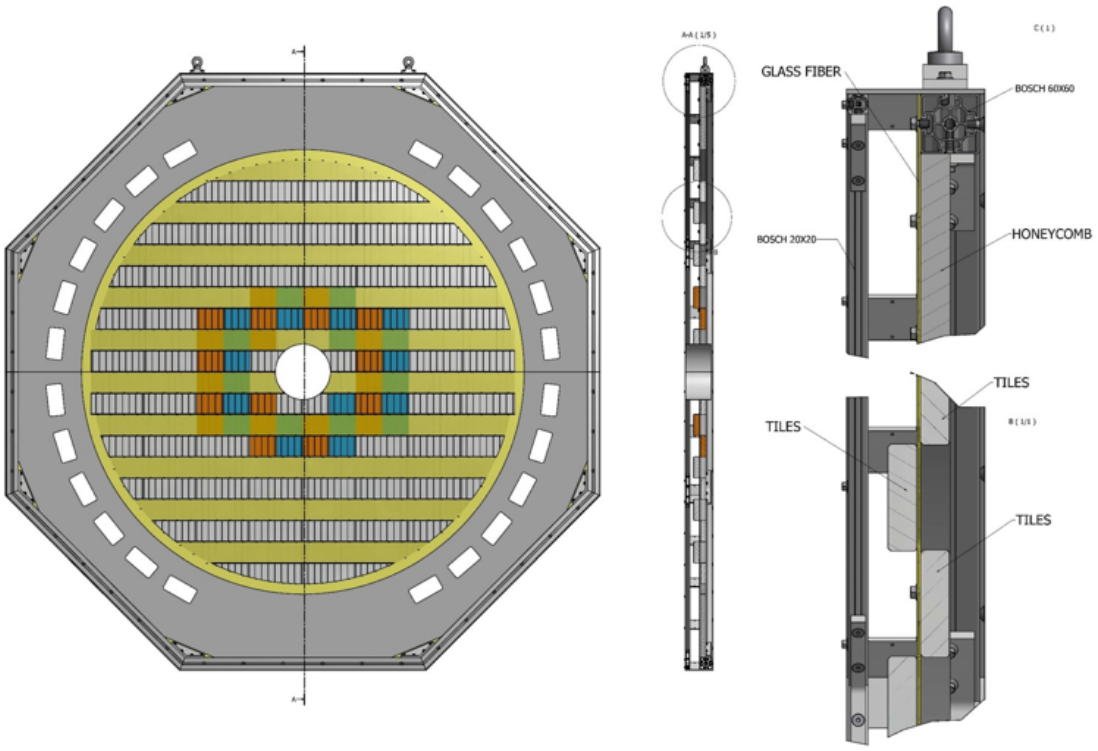

Figure 2.12: A cartoon of the CHOD (also known as NewCHOD), where the different tile segmentations are illustrated, from [21].

2.7.1 Large angle veto (LAV)

The LAV detector comprises of twelve ring shaped detectors place along the z axis of the experiment, with the first station at the beginning of the fiducial volume, and the last one downstream of the CHOD. Lead-glass blocks recycled from the OPAL electromagnetic calorimeter are used as the scintillating medium in each of the LAV modules, figure 2.13. The LAV stations have four or five layers of overlapping blocks, ensuring that a particle traversing the detector will pass through a minimum of three blocks. Each lead glass block is read out by a photo-multiplier coupled to the block via a 40 mm long cylindrical light guide.

2.7.2 LKr

The detection of photons at medium angles is left to the liquid krypton calorimeter (LKr), reused from the NA48 experiment. The calorimeter is filled with 120 litres of liquid krypton kept at a temperature of 120 K. The detector has a depth of 127 cm

(a) Photograph of the assmebled LAV1 station, with the ring shaped layers of scintillation blocks can be distinctly observed.

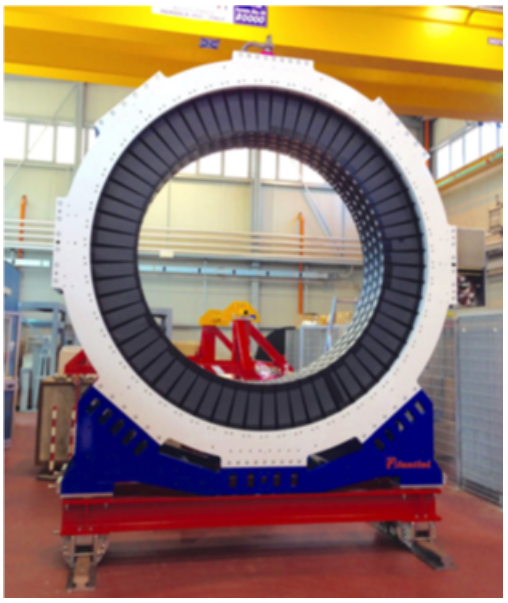

(b) Image showing the twelfth station of the NA62 large angle veto detector.

Figure 2.13: Photographs of the LAV1 (a) and LAV12 (b) stations, from [21].

(27 X_0), and so almost fully contains showers up to 50 GeV. The active area of the detector is divided into 13248 2×2 cm^2 longitudinal cells, formed by Cu-Be ribbon shaped electrodes, illustrated in figure 2.14. The energy resolution of calorimeter is

$$\frac{\sigma_E}{E} = \frac{4.8\%}{\sqrt{E[\text{GeV}]}} \oplus \frac{11\%}{E[\text{GeV}]} \oplus 0.9\%.$$

The energy resolution above makes the LKr one of the most precise calorimeters in the world.

The LKr calorimeter can also be used to reconstruct neutral pions from decays such as $K \to \pi^+\pi^0$, if both of the photons from the π^0 are detected by the calorimeter. This technique is used in the K_{l3} analysis presented in this thesis.

2.7.3 Small angle vetoes

The NA62 SAC detector is shown in figure 2.15. It is constructed of seventy lead plates and seventy plates made of injection moulded plastic scintillator, with each lead and scintillator plate have transverse dimensions of 205×205 mm^2 and thickness of 1.5

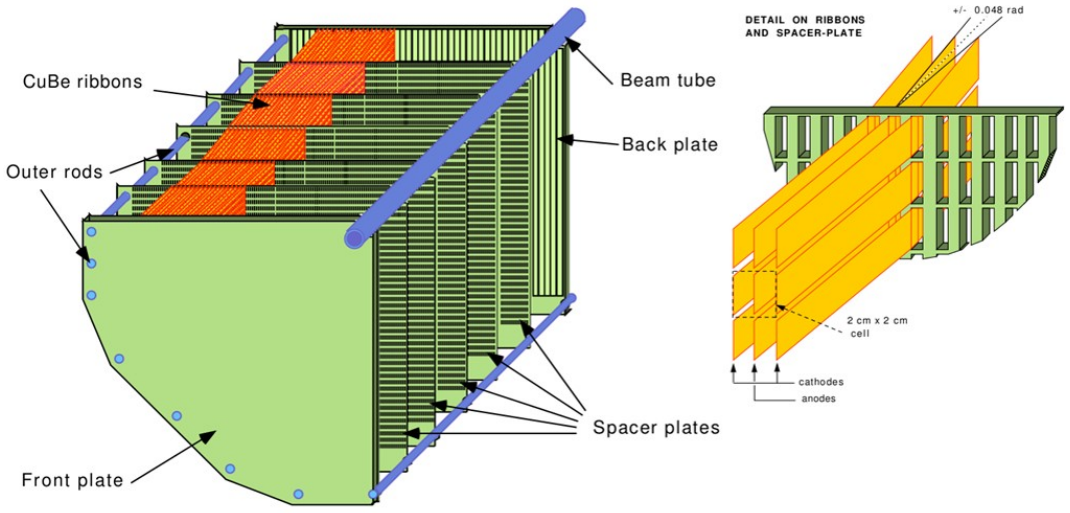

Figure 2.14: A schematic cartoon of the LKr cell structure, from [21].

mm, figure 2.15. The scintillation light is collected and directed out by 240 WLS fibres coupled to four PMTs.

The other small angle veto detector, the IRC, is also composed of lead/scintillator alternating layers, pictured in figure 2.16. The detector is in the shape of a cylinder placed around the beam pipe upstream of the LKr. The IRC is longitudinally segmented, where the upstream and downstream modules are constructed from twenty-five and forty-five ring shaped layers of absorber/scintillator respectively. WLS fibres in tandem with photomultipliers are used to collect and detect the scintillation light.

2.8 Ring imaging Cerenkov counter (RICH)

The NA62 RICH is used to provide π^+/μ^+ separation, achieving a muon suppression factor of 100 for tracks with momenta between 15 and 35 GeV/c. A schematic diagram of the RICH is shown in figure 2.17. The radiator vessel of the RICH is 17.5 m long, and it is filled with neon at atmospheric pressure and room temperature. The downstream end of the vessel houses twenty spherical mirrors used to reflect the Čerenkov photons towards the light collection system located in the upstream part of the detector. These parameters allow the detector to reach its desired π^+ identification efficiency in the relevant momentum range, placing the pion activation threshold at 12.5 GeV/c. Around

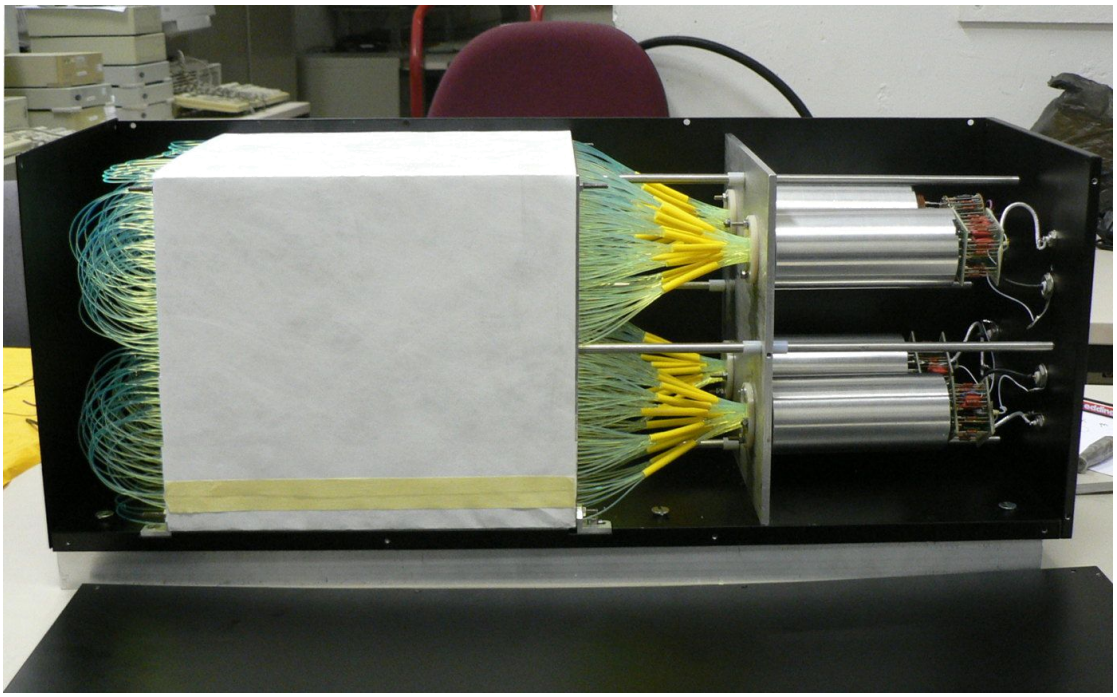

Figure 2.15: A photograph of the NA62 small angle calorimeter (SAC), from [21].

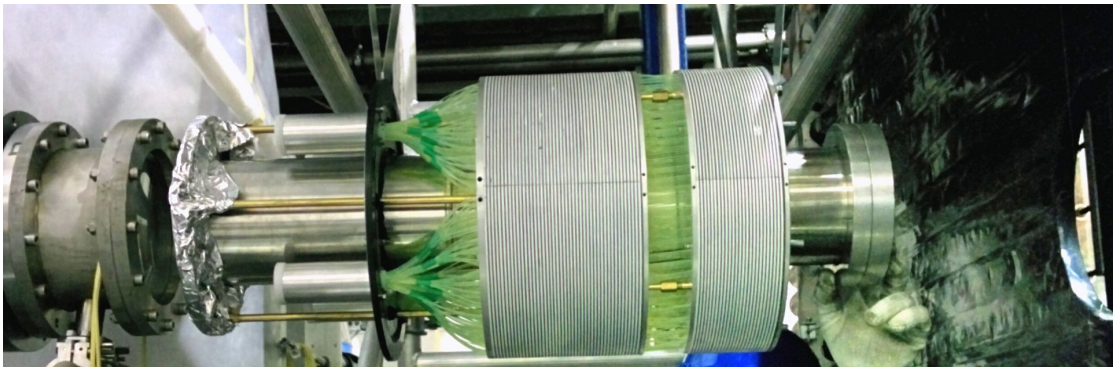

Figure 2.16: A photograph of the NA62 small angle calorimeter (IRC), with upstream and downstream segmentation clearly visible, from [21].

2000 PMs are used to collect the light emitted by the charged particles travelling through the neon gas. The time resolution of the RICH is around 100 ps, making it a suitable choice for providing the reference time of downstream tracks.

2.9 Muon vetoes

The muon veto system is made up of three separate sub-detectors, that together with the LKr, provide calorimetric π^+/μ^+ separation complementary to the RICH. MUV1 and MUV2 are both hadron calorimeters composed of alternating layers of iron and

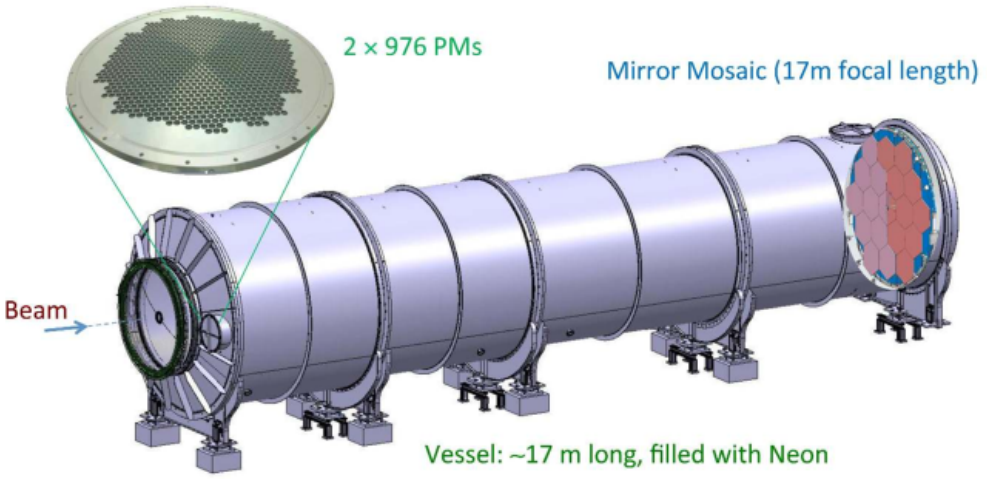

Figure 2.17: A schematic drawing of the NA62 RICH vessel, showing the mirrors and PM array, from [21].

scintillation material. They are followed by the fast muon veto MUV3, which sits behinds an 80 cm iron wall, and participates in the NA62 low level trigger.

2.9.1 MUV1

The MUV1 consists of twenty-four 26.8 mm thick steel plates, interspaced by twenty-three layers of scintillator strips of 9 mm thickness. Each layer is made up of 44 strips, where successive layers are alternately aligned in the horizontal and vertical directions, resulting in twelve horizontally and eleven vertically orientated sheets. The eight vertical and six horizontal strips near the beam pipe are split in half to accommodate the pipe and the high particle rate. The scintillator strips are read out by photo-multipliers via two WLS fibres per each longitudinal side, resulting in a total channel count of 176. The total thickness of the detector amounts to 4.1 interaction lengths.

2.9.2 MUV2

Twenty-four iron and scintillator layers sandwiched together form the MUV2 hadronic calorimeter, adding up to 3.7 interaction lengths. Each scintillation layer is made up of forty-four 4.5 mm thick strips, where each strip spans half the detector. The layer of scintillators are alternately aligned in the horizontal and vertical directions. The two strips around the beam pipe in each scintillator half plane are shaped to fit around the curvature of the beam pipe. Each strip is read out by photo-multipliers via Plexiglas light guides. The total MUV2 channel count is 88.

2.9.3 MUV3

The MUV3 detector provides fast muon veto or alternatively μ identification. The detector is built up from 148 square plastic scintillating tiles, where 140 of the tiles have transverse dimensions of 220×220 mm^2. The 8 tiles surrounding the beam pipe are smaller, in order to accommodate the higher beam rate. The hit rate for each tile, obtained from a simulation, is shown in figure 2.18. Each scintillating unit is placed in a light box to avoid cross-talk, and is read out by two PMTs, adding up to 296 channels in total.

2.10 Additional vetoes

The peripheral muon veto (MUV0) and the hadronic sampling calorimeter (HASC) are two veto detectors specifically designed to detect pions coming from $K^+ \to \pi^+\pi^+\pi^-$ decays which escape the lateral acceptance of the STRAW. Such decay topologies can mimic single track events, and hence may be a background to $K^+ \to \pi^+\nu\nu$.

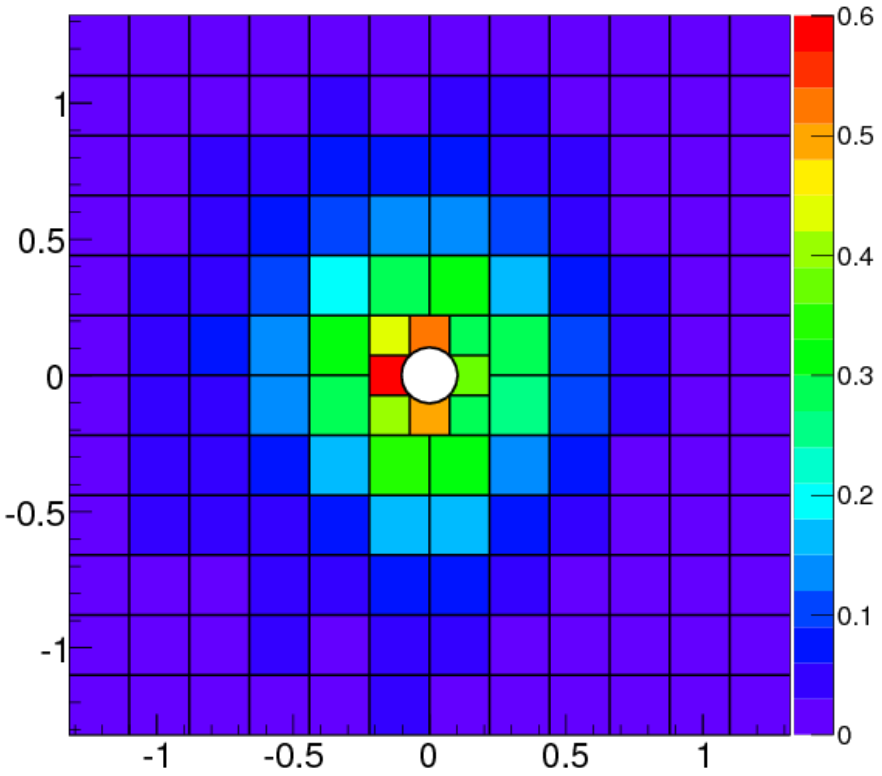

Figure 2.18: The geometry of the MUV3 tiles, and the rate (in MHz) in each at the nominal beam rate. The tile on the left hand side next to the beam pipe sees an increased rate mainly due to muons originating from beam pion decays, from [21].

2.10.1 Peripheral Muon Veto (MUV0)

The MUV0 is mounted on the downstream flange of the RICH, and it is designed to detect negative pions with momentum below 10 GeV/c deflected in the positive x direction by the MNP33. The detector is constructed of 48 plastic scintillator tiles, with a total active area of 1.4×1.4 m^2.

2.10.2 Hadronic Sampling Calorimeter (HASC)

The HASC is used for detection of π^- with momentum above 50 GeV/c travelling through the beam holes of the STRAW chambers. The detector is placed downstream of the BEND dipole magnet sweeping away from the beam from the SAC, figure 2.5. Nine identical modules make up the detector. Each module consists of sixty lead plates interleaved with scintillator plates. The modules are read out in ten segments by WLS fibres and SiPMs.

2.11 Trigger and data acquisition (TDAQ)

The NA62 TDAQ system follows a two tier scheme, with the first level being a hardware based trigger referred to as L0, and a second level based on a software trigger called L1. The particle decay rate inside the detector is around 10 MHz and serves as the input to the L0 trigger, where the maximum output rate was chosen to be 1 MHz. The output of L0 is the input to the L1 software trigger, which further reduces the data flow to a few kHz, allowing for the data to be written on disk/tape. An overview of the NA62 TDAQ architecture is illustrated in figure 2.19.

The readout (RO) system of each sub-detector that participates in the L0 trigger continuously evaluates a set of predefined conditions on the digitized data coming from the detector. The result of these algorithms is encoded into data units called primitives, which are sent to the central L0 trigger processor (L0TP). A set of specific combinations of particular primitives, which are in time, is known as a trigger mask. The L0TP is programmed to look for the occurrence of several different such combinations, dispatching an L0 trigger signal if the conditions of at least one mask have been satisfied. Due to the high rates possible from certain masks, e.g. the minimum bias control trigger, a downscale factor (D_s) can be set for each active mask, meaning that only 1 in D_s occurrences of the required conditions for a mask will generate an L0 trigger.

Upon receiving an L0 trigger, most sub-detectors immediately send their data to the 30 PCs (PC farm) running the L1 software algorithms. The exceptions being the GTK, LKr, MUV1, and MUV2 which store their data in a local buffer, and only send data to the PC farm upon the receipt of a successful L1 trigger. Reading out these detectors only after an L1 trigger greatly reduces the required data bandwidth. The transport of data from the sub-detectors to the PC farm is achieved via the use of a switched Gigabit Ethernet network.

As with the L0 trigger, several different L1 trigger algorithms run concurrently, allowing for a range of trigger streams. If there is a successful verdict from a particular set of L1 conditions, then the data from the remaining detectors is read out. Following this, the data events are built and temporarily stored on disk in one of the three merger PCs.

The raw data is eventually moved onto tape, freeing up the space on the merger disks. The possibility of a second level software trigger (L2) exists, however such a tier has not been implemented so far.

2.12 Detector control system (DCS)

This section describes an essential part of the NA62 detector infrastructure, its detector control system (DCS) [25]. The DCS allows the remote configuration and operation of each NA62 sub-detector and its corresponding sub-components, e.g. individual low voltage or high voltage channels, the power supplies themselves, read-out electronics. The DCS also performs a monitoring function, where the state of each detector is continually monitored and any deviation from nominal operational conditions is flagged up. For example, each channel will have an alarm configured based on its ON/OFF state, where an alarm will be raised if the channel is found to be "OFF", when it should be "ON".

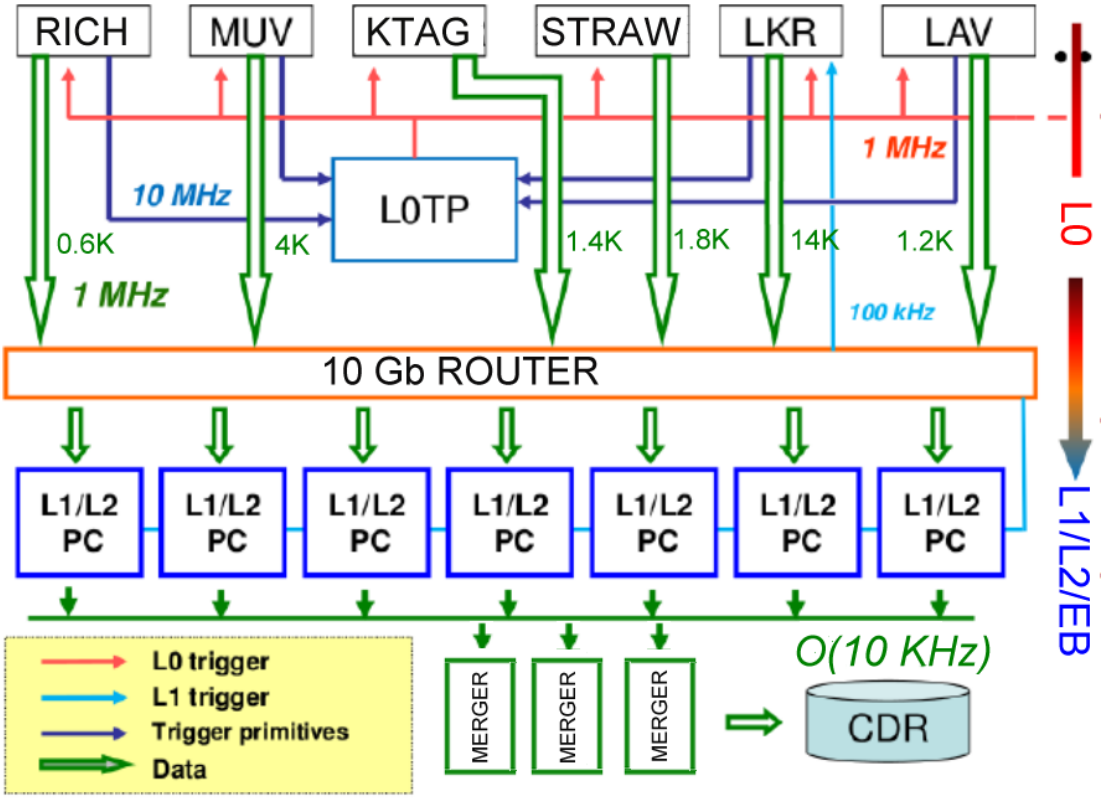

Figure 2.19: Archeticure of the NA62 trigger and data acquisition system, from [21].

The DCS of NA62, and indeed other CERN experiments, is based on the commercially available software WinCC OA (previously known as PVSS) [26]. The JCOP framework [27], developed at CERN, is used on top of WinCC OA to build up the DCS. Within the framework, modules enabling the control (and communication with) some of the most commonly used hardware at CERN, e.g. CAEN power supplies, are already available. These modules along with other tools, e.g. a finite state machine (FSM) implementation, greatly speed up the development and integration of the detector control systems across CERN.

The ability to remotely control detector systems serves directly to raise the uptime of the experiment, and its data-taking efficiency, by reducing the time for power-cycle or reset operations to be carried out. This is why it is essential that any piece of hardware involved in data-taking is properly integrated into the DCS. Section 2.12.1 describes the integration of a new piece of hardware, a power distribution unit (PDU), which was deployed throughout NA62 in 2018.

Another way in which the DCS helps to increase data-taking efficiency is by alerting NA62 shifters if a monitored detector parameter goes out of its predefined optimal range. To reduce the response time of shifters, and therefore the time it takes for issues to be resolved, each alarm in the NA62 DCS needs to be properly configured, and active. The development of a custom module, which displays NA62 DCS alarms which are configured but not active, is detailed in section 2.12.2. The work described in the sections 2.12.1 and 2.12.2 was carried out by the author of this thesis.

2.12.1 PDU control

A number of network switches are installed in the NA62 experimental caverns, TCC8 and ECN3. These switches form part of the NA62 network used for data collection and detector control. During the data collection runs in 2016 and 2017, it was found that occasionally these switches would get "stuck", and no longer transmit or receive data. In such cases, the switch in question had to be manually power-cycled requiring human intervention in the experimental area. Entering the experimental caverns during an active data-taking period is a disruptive and time consuming procedure, necessitating

the interruption of the beam hence data-taking, and authorisation from the CERN Control Centre (CCC).

To enable the power cycle of the switches remotely, and without human presence in the NA62 caverns, ten remote controlled power distribution units (PDU) were installed in the experimental area in June 2018. Each PDU has eight individually controlled outlets allowing the control of up to eight separate devices per PDU. To ensure operational consistency across the experiment, and enable the archiving of the status of the PDUs and any commands sent to them, the power strips were integrated into the NA62 DCS.

A new device class was written, abstracting the possible states of the PDU and its channels, and also any commands which could be sent to the device. Along with the device abstraction, a user interface control panel was developed, figure 2.20, facilitating the control of the PDU by the user. The access to the different PDU panels is achieved by the newly written, "PDUs of NA62" panel, figure 2.21. The DCS communicates directly with the PDU via the simple network management protocol (SNMP).

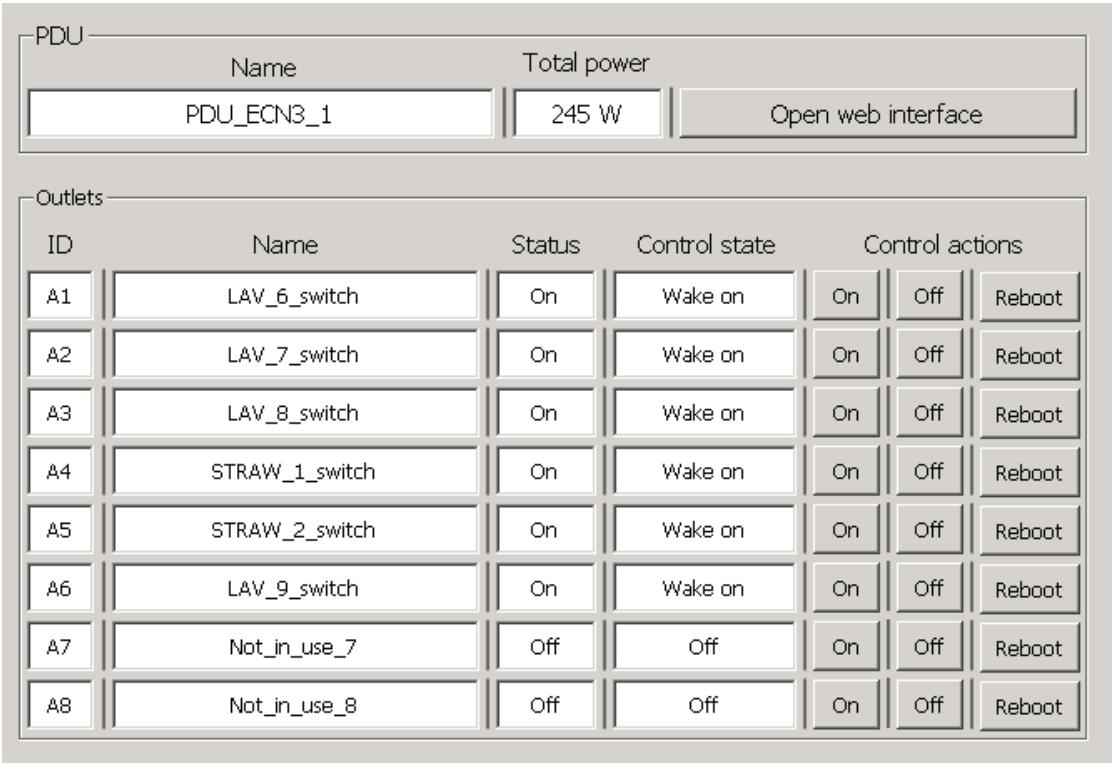

Figure 2.20: A screenshot of the UI panel used to the control individual PDUs installed throughout the experiment.

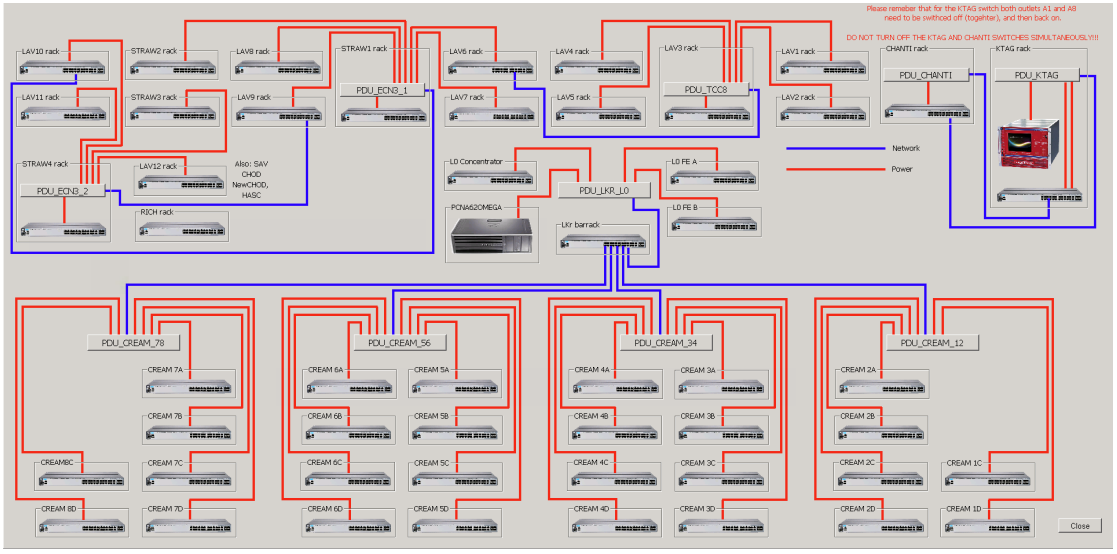

Figure 2.21: The NA62 PDU panel used to access the different individual PDU UI panels. The panel also includes a schematic drawing of how the PDUs are interconnected.

The 49 PDU connected switches, shown in figure 2.21, needed to be rebooted a total of 367 times since the integration of the PDUs in June 2018. A power-cycle of a switch using a PDU is approximately 30 minutes quicker compared to a local intervention, meaning that without the proper integration of the PDUs in the DCS, the experiment would have lost approximately 184 hours of data-taking.

2.12.2 Masked alarms tool

It is sometimes convenient to temporarily mask an alarm for particular detector conditions, e.g. a HIGH/LOW temperature alarm due to a faulty temperature probe. It is essential however, for the alarm to be re-enabled once the issue causing it to be masked is resolved, otherwise potentially dangerous detector conditions may occur without detection.

To ease the discovery of masked alarms within the NA62 DCS, a panel was developed to display the list of such alarms, allowing the user to filter the list per sub-detector or with a specific keyword, figure 2.22. The starting point for the development of the panel was a panel already available in the JCOP framework with similar functionalities, figure 2.23. While this panel performed the basic functionality of displaying masked alarms, it

has several key downsides which made it not suitable for use out of the box, these will now be summarised.

The default panel is difficult to access, and only available to DCS experts, a regular NA62 shifter cannot access it. The panel can only show masked alarms from the WinCC OA project in which it is summoned, this presents an issue since the control system for each subdetector is hosted in a different WinCC OA project. These projects are spread out across several different physical machines. To get a list of masked alarms for the whole NA62 detector, one would need to log into multiple different machines and open a different panel for each sub-detector. Another shortcoming was the fact that the JCOP panel did not allow for filtering the list of displayed inactive alarms.

The new masked alarm panel was designed to be a distributed component where a piece of code which queries the project's internal database for masked alarms sits on each individual DCS project, with the results of the query, i.e. the list of masked alarms, stored in a variable within the project. The central DCS project which brings all the other sub-detector projects in a central user interface, hosts the newly developed panel and queries each project's data point for the already retrieved list of inactive alarms. This architecture means that the database queries are able to run in a parallelised way, which greatly reduces the search time. The interrogation of each project's database is performed via the means of a SQL query.

The convenience and flexibility of the new masked alarm tool will help NA62 detector experts ensure all appropriate detector parameter alarms are properly configured and armed. This will contribute to increasing the uptime of the experiment, which is essential in helping NA62 reach its goals.

2.13 Summary

The NA62 detector and its supporting infrastructure, described in this chapter, enable the precision measurement of the $K^+ \to \pi^+ \nu\bar{\nu}$ branching fraction. The versatility and flexibility of the experiment also allows for a wide range of K^+ related physics analyses to be performed, such as the K_{l3} branching fraction measurement discussed in this thesis.

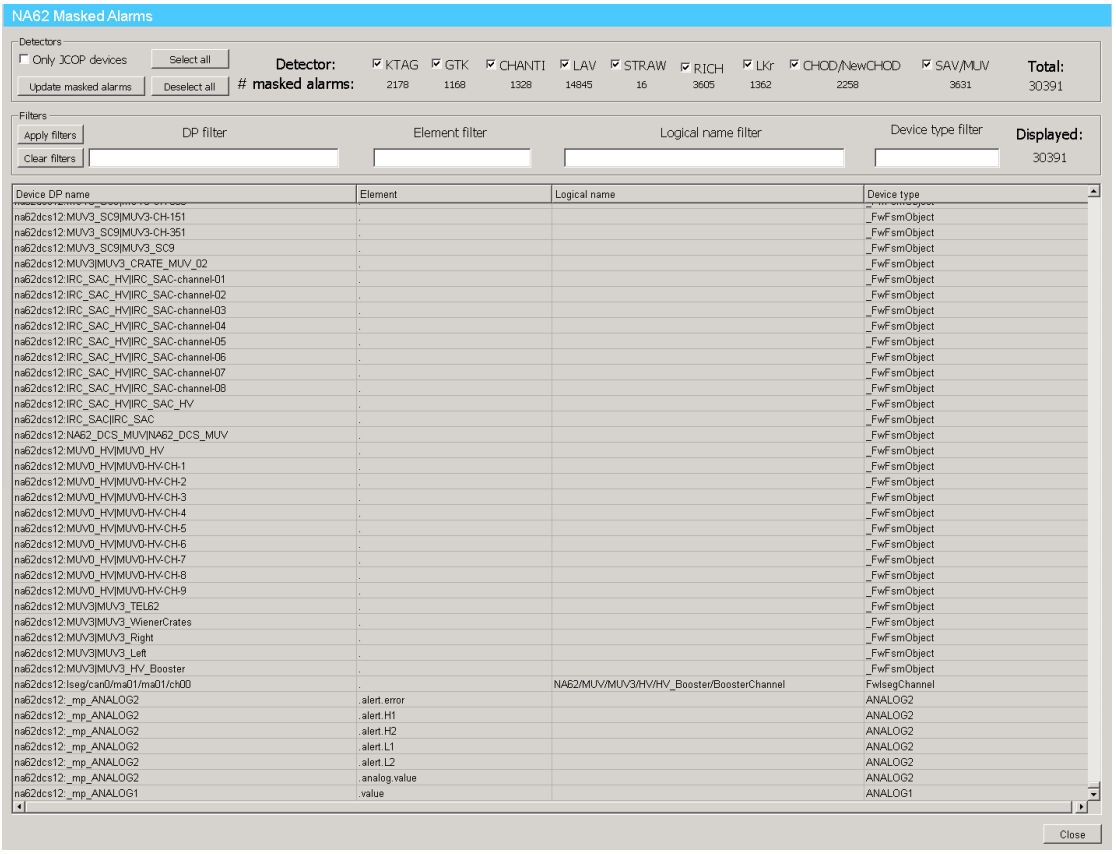

Figure 2.22: A screenshot of newly developed NA62 masked alarms panel.

The CEDAR vessel, which is a part of the kaon tagging system of the experiment, allows for the option to be operated with hydrogen, potentially reducing the rate of background in detectors further downstream. The use of hydrogen is likely however to have an impact on the performance of the KTAG itself. There are also particular operational challenges around the use of H_2, due to the explosive properties of the gas. The modifications required for the safe H_2 operation of the CEDAR, as well as the impact on the performance of downstream detectors are discussed in the following chapter.

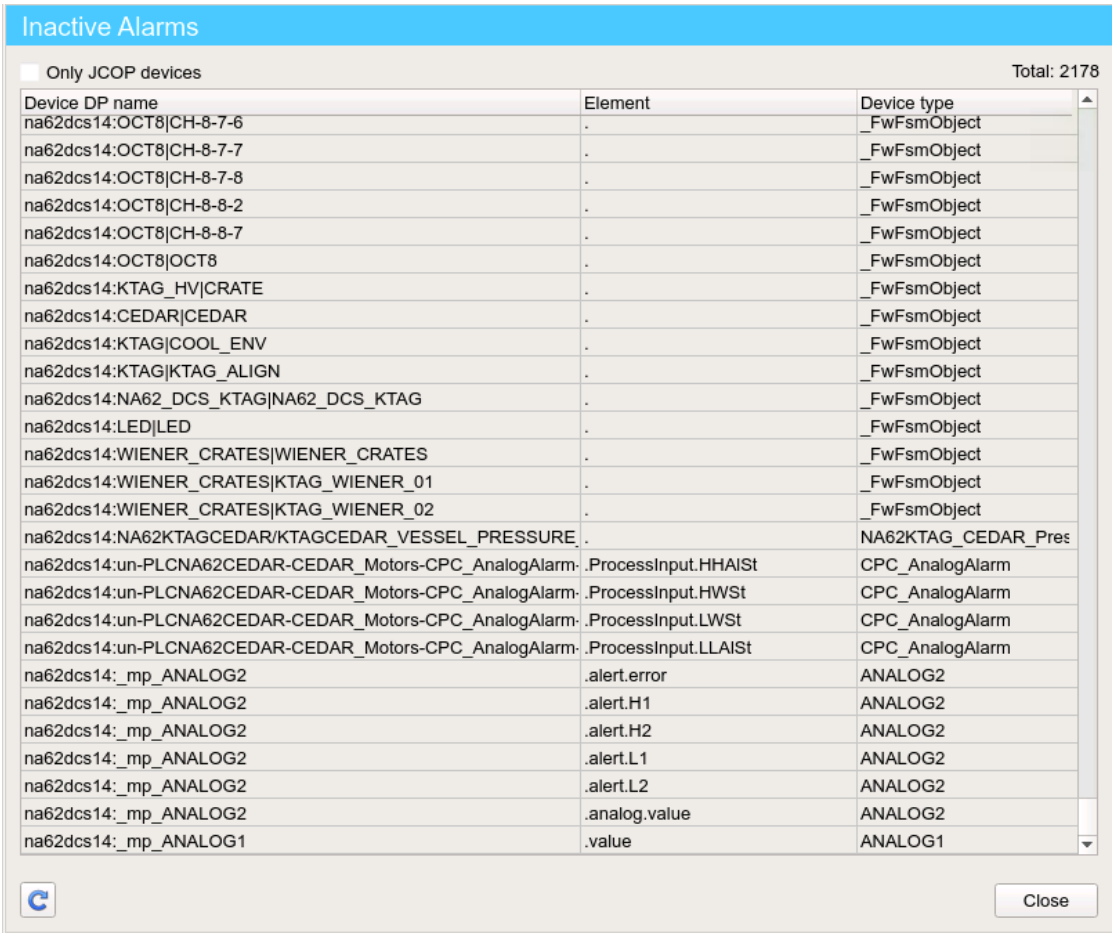

Device DP name	Element	Device type
na62dcs14:OCT8|CH-8-7-6	.	_FwFsmObject
na62dcs14:OCT8|CH-8-7-7	.	_FwFsmObject
na62dcs14:OCT8|CH-8-7-8	.	_FwFsmObject
na62dcs14:OCT8|CH-8-8-2	.	_FwFsmObject
na62dcs14:OCT8|CH-8-8-7	.	_FwFsmObject
na62dcs14:OCT8|OCT8	.	_FwFsmObject
na62dcs14:KTAG_HV|CRATE	.	_FwFsmObject
na62dcs14:CEDAR|CEDAR	.	_FwFsmObject
na62dcs14:KTAG|COOL_ENV	.	_FwFsmObject
na62dcs14:KTAG|KTAG_ALIGN	.	_FwFsmObject
na62dcs14:NA62_DCS_KTAG|NA62_DCS_KTAG	.	_FwFsmObject
na62dcs14:LED|LED	.	_FwFsmObject
na62dcs14:WIENER_CRATES|WIENER_CRATES	.	_FwFsmObject
na62dcs14:WIENER_CRATES|KTAG_WIENER_01	.	_FwFsmObject
na62dcs14:WIENER_CRATES|KTAG_WIENER_02	.	_FwFsmObject
na62dcs14:NA62KTAGCEDAR/KTAGCEDAR_VESSEL_PRESSURE_	.	NA62KTAG_CEDAR_Pres
na62dcs14:un-PLCNA62CEDAR-CEDAR_Motors-CPC_AnalogAlarm·	.ProcessInput.HHAlSt	CPC_AnalogAlarm
na62dcs14:un-PLCNA62CEDAR-CEDAR_Motors-CPC_AnalogAlarm·	.ProcessInput.HWSt	CPC_AnalogAlarm
na62dcs14:un-PLCNA62CEDAR-CEDAR_Motors-CPC_AnalogAlarm·	.ProcessInput.LWSt	CPC_AnalogAlarm
na62dcs14:un-PLCNA62CEDAR-CEDAR_Motors-CPC_AnalogAlarm·	.ProcessInput.LLAlSt	CPC_AnalogAlarm
na62dcs14:_mp_ANALOG2	.alert.error	ANALOG2
na62dcs14:_mp_ANALOG2	.alert.H1	ANALOG2
na62dcs14:_mp_ANALOG2	.alert.H2	ANALOG2
na62dcs14:_mp_ANALOG2	.alert.L1	ANALOG2
na62dcs14:_mp_ANALOG2	.alert.L2	ANALOG2
na62dcs14:_mp_ANALOG2	.analog.value	ANALOG2
na62dcs14:_mp_ANALOG1	.value	ANALOG1

Figure 2.23: The default masked alarm panel from the JCOP framework which was used as a starting point for the NA62 custom version.

Chapter 3

Operation of CEDAR with hydrogen

The ultimate goal of NA62 is to collect around 100 $K^+ \to \pi^+\nu\bar{\nu}$ events. To do so, it needs to put on tape around 10^{13} K^+ decays, assuming a $\pi^+\nu\bar{\nu}$ branching ratio of around 10^{-10}, and a signal acceptance of approximately 10%. These considerations drive the choice of a high intensity, 75 GeV/c secondary hadron beam, comprising around 6% kaons, 24% protons, and 70% pions. The disadvantage of using a high energy beam is that it becomes difficult to separate out the non-useful beam particles, i.e. the protons and the pions.

If a beam pion were to interact with the residual gas in the fiducial volume, it could enter into the detector acceptance, and mimic the signature of a $K^+ \to \pi^+\nu\bar{\nu}$ decay. A vacuum at the level of 10^{-8} mbar would be required to keep the rate of this process down to less than one occurrence per year. The condition on the vacuum can be relaxed by an order of magnitude if kaons entering the experiment are tagged, and this is achieved by using the KTAG detector.

The KTAG detector consists of a CEDAR, designed and built in the early 1980s by CERN, coupled with new photon detectors and FE electronics. The 750 MHz beam

rate, means that a time resolution at the level of 100 ps is required. Positively identifying kaons also aids in suppressing background arising from upstream-downstream track mismatching. The principles of the CEDAR operation are described in section 3.1.

The CEDAR used for the KTAG is designed to be filled with N_2, with the internal optics optimised to cancel the light dispersion caused by the nitrogen gas. The original plan for the NA62 CEDAR was to swap the radiator gas from nitrogen to hydrogen. Doing so, reduces the amount of the material in the beam line, and therefore the scattering of the beam. Using H_2 inside the CEDAR means that the dispersion correction of the internal optics is no longer optimal. The reduced efficacy of the optical correction could potentially cause up to 30% less light yield [21], and degrade the KTAG performance. The magnitude of this effect, which was not fully understood at the time of the H_2 operation proposal, means that it is not clear that the H_2 CEDAR configuration is the optimal one for the NA62 experiment.

In order to clarify the situation, two distinct aspects of the H_2 CEDAR operation need to be studied.

- The reduction of the beam scattering from using H_2 compared to N_2, and its effects on downstream detectors.
- The drop in KTAG performance, i.e. K^+/π^+ separation power and time resolution, caused by the gas swap.

These points are discussed in more detail in section 3.2. The investigation of the second point in particular requires that the CEDAR is operated with H_2. Operational challenges in using H_2, arise from the flammable nature of the gas. Section 3.3 outlines some of the work done to prepare the CEDAR for safe H_2 operation. Section 3.4 discusses the studies performed to evaluate the impact of CEDAR H_2 on detectors downstream of the KTAG.

3.1 Detector principles

Particles travelling through a medium faster than the phase velocity of light in that medium, emit radiation in cones at an angle θ, this is the Čerenkov effect. The angle of emission θ, depends only on the velocity of the particle and the refractive index of the medium it is crossing, via equation 3.1:

$$cos\theta = \frac{1}{n\beta}, \tag{3.1}$$

where n is the refractive index of the material, and β is the particle velocity. β is given by:

$$\beta = \left[1 + \left(\frac{m}{p}\right)^2\right]^{-1/2}, \tag{3.2}$$

with m being the particle mass, and p being its momentum. Therefore for a particle beam with a fixed momentum crossing a medium with a fixed refractive index, the angle θ only depends on the mass of the particles. The CEDAR exploits this fact to perform its particle identification.

The detector focuses the Čerenkov light emitted by particles into a ring, where the ring radius is dependent on θ, and the focal length of the system f (which is fixed). For two particles, with masses m_1 and m_2, the difference in radii between the two rings produced, Δr, is:

$$\Delta r = f\Delta\theta = \frac{f}{\theta}\frac{m_2^2 - m_1^2}{2p^2}, \tag{3.3}$$

A diaphragm with a fixed radius (r_D), and a variable width (w_D) annular aperture, pictured in figure 3.1, ensures only light coming from rings with radii r_D reaches the photo sensitive parts of the detector. Particles of different masses can only be separated if $\Delta r > w_D$. Since the radius of the rings from which light will be detected is fixed, θ in equation 3.1 is fixed. Therefore to select the mass of the particle to be identified,

one needs to adjust the refractive index; this is done by varying the pressure of the gas inside the CEDAR.

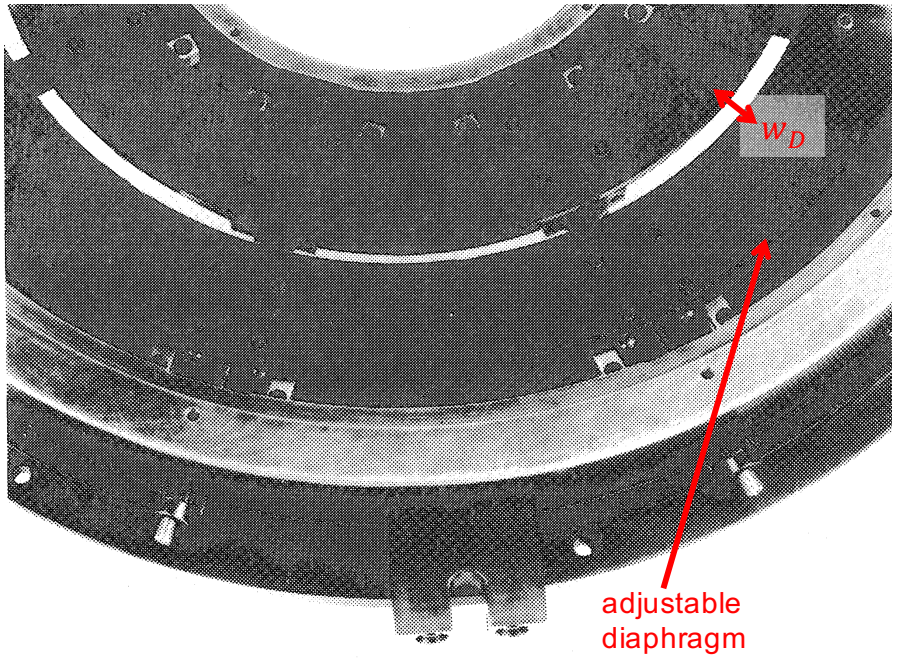

Figure 3.1: A photo of the CEDAR diaphragm, with the width of its adjustable aperture annotated as w_D, from [22].

The Čerenkov light is focussed onto the diaphragm plane by a series of optical components which include a Mangin mirror, a chromatic corrector, and a condenser. The optical set-up is illustrated in figure 3.2.

There are several effects which can broaden the radius of the ring, and hence reduce the separation power of the CEDAR. The most severe of these is the dispersion of Čerenkov light caused by its traversal of the radiator gas. To mitigate this effect, chromatic correctors, which compensate for the dispersion profile $n(\lambda)$ of the gas in the CEDAR, are used.

Beam divergence is another factor which affects the sharpness of the ring image focussed onto the diaphragm. If the beam particles do not have parallel trajectories, the cones of Čerenkov light will not be concentric. The effect of this on the light ring is illustrated in figure 3.3c.

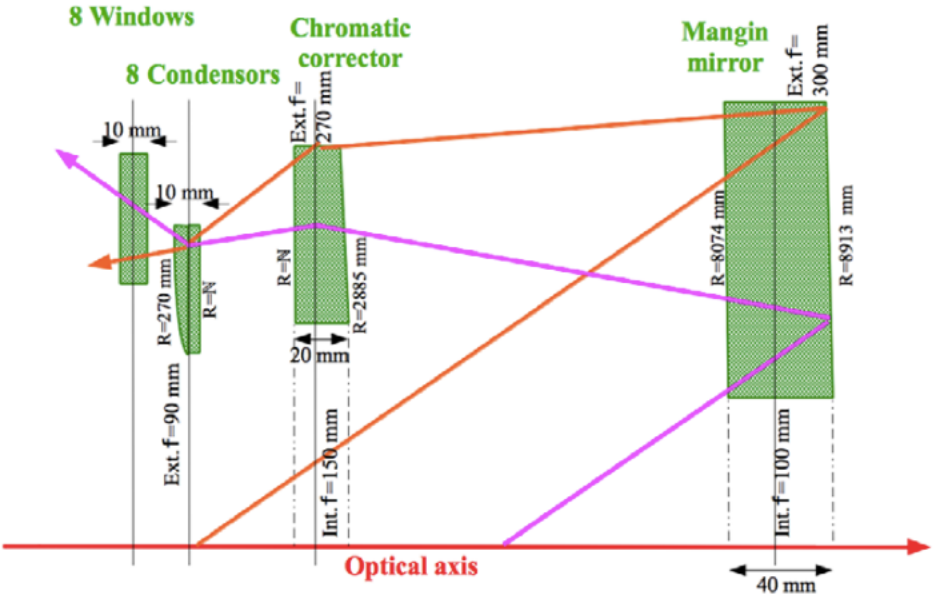

Figure 3.2: A schematic drawing of the CEDAR optics used to focus the Čerenkov cones into rings, from [22].

A broadening effect also arises from the multiple scattering of the beam as it travels through the detector. If the beam particles change direction as they go through the CEDAR, the photons emitted will not be in concentric circles, figure 3.3d.

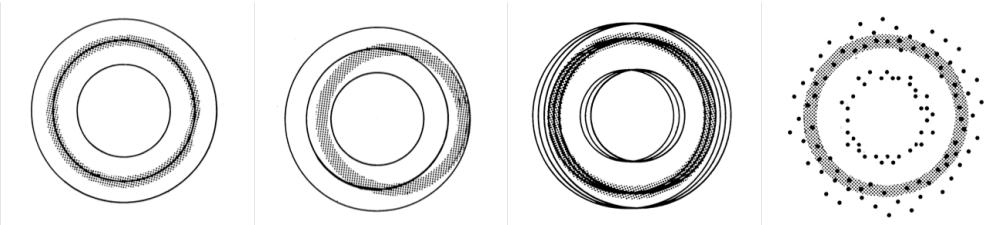

(a) A good alignment of the CEDAR. (b) The CEDAR misaligned. (c) Off-centre rings due to beam divergence. (d) Broadening due to multiple scattering.

Figure 3.3: The different distortions of the shape of the Čerenkov ring due to various broadening effects. Shaded area represents the diaphragm opening, from [22].

3.2 Nitrogen vs hydrogen as radiator gas

As the beam travels through the length of the CEDAR it undergoes multiple scattering. The effect of this scattering is to increase the number of background hits seen in the downstream detectors. Possible consequences of the increased background hit rates are an increased rate of random veto and degraded track reconstruction. The phenomenon

of random veto happens when a signal is present in a veto detector, causing the event to be wrongly rejected. A higher rate of random veto decreases the signal efficiency, leading to an overall lower yield of signal events. The $\pi\nu\bar{\nu}$ analysis is particularly affected by this due to its unique signal signature of a single π^+ and nothing else.

The deviation of a particle's trajectory due to multiple scattering depends on the amount material the particle passes through. Therefore reducing the material budget of the CEDAR, should decrease the amount angular divergence introduced to the beam, leading to lower background rates in the detectors downstream of the CEDAR. Using hydrogen instead of nitrogen as the CEDAR radiator gas would lower the material budget of the KTAG. The material budgets for the two gases at their operating pressures is listed in table 3.1.

	Nitrogen	Hydrogen
Pressure [bar]	1.3	3
Aluminium window thickness [μm]	2 × 100	150+200
Aluminium window thickness [$10^{-3}X_0$]	2.2	3.9
Gas thickness [$10^{-3}X_0$]	35	3.2
Total thickness [$10^{-3}X_0$]	37.2	7.1

Table 3.1: Summary of the operational pressures and material budgets of the CEDAR filled N_2 and H_2. The aluminium windows referred to here, separate the CEDAR vessel from the evacuated beam pipe.

As discussed in section 3.1, the current CEDAR optics compensate for the aberration due to the light travelling through the nitrogen. If the CEDAR is filled with hydrogen, this correction will no longer be optimal, and the Čerenkov light will no longer be sharply focussed at diaphragm radius, r_D. Figure 3.4 [24] illustrates this effect, where the radius of the Čerenkov light ring arriving at the diaphragm plane is plotted as a function of the light wavelength λ, for nitrogen (figure 3.4a) and hydrogen (figure 3.4b).

Without a reconfiguration of the optical system, the light yield is expected to be around 30% less [21]. The decreased number of hits associated with fewer photons hitting the photomultipliers will result in a worse time resolution, potentially impacting $K^+ - \pi^+$ matching. Some light can be recovered by increasing the width of diaphragm aperture,

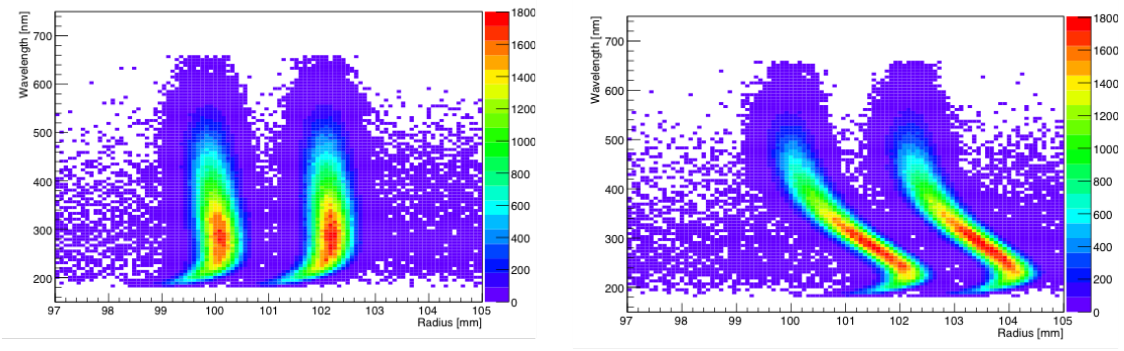

(a) Radii of rings from kaons (left) and pions (right) versus λ for the CEDAR filled with nitrogen.

(b) Radii of rings from kaons (left) and pions (right) versus λ for the CEDAR filled with hydrogen.

Figure 3.4: Radius of the Čerenkov light ring at the diaphragm as a function of its wavelength, for N_2 (left) and H_2 (right), from [24].

therefore letting more light through. This however will mean that light originating from beam pions as well as kaons will reach the KTAG PMs, resulting in a worse K/π separation. Using the H_2 as the CEDAR radiator gas clearly has both upsides and downsides, and the balance between those will decide whether there is an overall benefit to the experiment.

3.3 Hydrogen operation safety

Putting hydrogen inside the CEDAR has certain safety implications, relating to the fact that hydrogen is a flammable gas. For a fire or an explosion to occur, two conditions need to be met simultaneously: the concentration of hydrogen in air (by volume) must be in the flammable range, and an ignition source must be present. Hydrogen can ignite in a wide range of concentrations, and it only needs 0.019 mJ of ignition energy. The minimum concentration needed for H_2 to burn in air is 4%, this is known as the lower explosive limit (LEL), if the concentration of hydrogen climbs above 75%, the mixture becomes too rich to burn: the upper explosive limit (UEL).

The safety arrangements around operating the CEDAR with H_2 are aimed at preventing either of the above conditions occurring separately, or at the same time. A key part of these arrangements are several hardware interlocks designed to power down or prevent from powering up, electrical equipment located in and around the CEDAR, therefore

removing potential sources of ignition. This electrical equipment includes the detector high and low voltage power supplies, alignment and diaphragm motors, and switches inside the CEDAR gas volume. A photo of the KTAG experimental area is shown in figure 3.5. The interlocks are triggered when potentially dangerous conditions arise, table 3.2 summarises four of the interlocks implemented and their triggers.

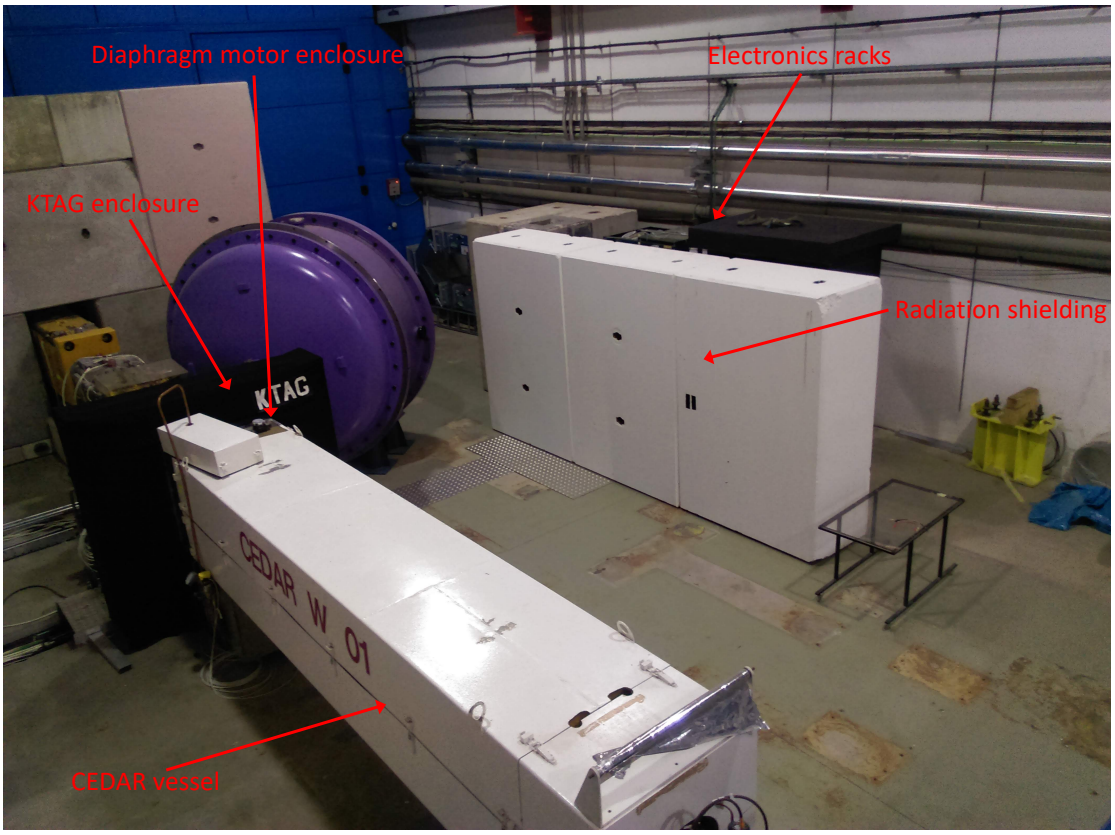

Figure 3.5: A photo of the KTAG detector and its systems.

Interlock name	Condition	Receiving system	Description
CEDAR H_2 leak	Gas leak during a filling, or a pressure drop during an operation	KTAG HV, LV	Stop H_2 filling and interlock KTAG HV, LV
Low N_2 flow in diaphragm motor enclosure	Diaphragm motor enclosure N_2 flow <10 l/hr	CEDAR diaphragm motor	De-energize CEDAR diaphragm motor
Low N_2 flow in KTAG enclosure	N_2 flow in KTAG enclosure <300 l/hr for 24 hrs	KTAG HV, LV	Interlock KTAG HV, LV
CEDAR end switches power on forbidden	H_2 is inside of CEDAR	CEDAR diaphragm end switches	Inhibit energization of diaphragm end switches

Table 3.2: Summary of the interlocks required for CEDAR operation with H_2

The CEDAR gas control system (GCS) continuously evaluates the interlock conditions described in the table 3.2. Each interlock is represented in hardware by a programmable

logic controller (PLC) output, which is used to drive a relay. In the normal operational state (when the interlock conditions are false), the relevant output, and therefore the relay, are energised, causing the relay pins acting as the dry contact to be closed. If the interlock trigger is evaluated as true, the output is de-energised causing the dry contacts to open, and delivering the interlock signal. This scheme also ensures that the interlock is in a safe state in the case of a hardware failure. An example implementation of a dry contact is illustrated in figure 3.6.

3.3.1 High and low voltage power supplies

A metal enclosure at the upstream end of the CEDAR, shown in figure 3.5, houses the photo multipliers, and the read-out electronics of the KTAG. The power supplies providing the high and low voltage to the equipment are located in racks several metres away from the detector, and are also indicated in figure 3.5. The KTAG electronics enclosure is permanently flushed with nitrogen in order to prevent the ingress of a potential hydrogen-air mixture. In case of a prolonged failure of the nitrogen flushing,

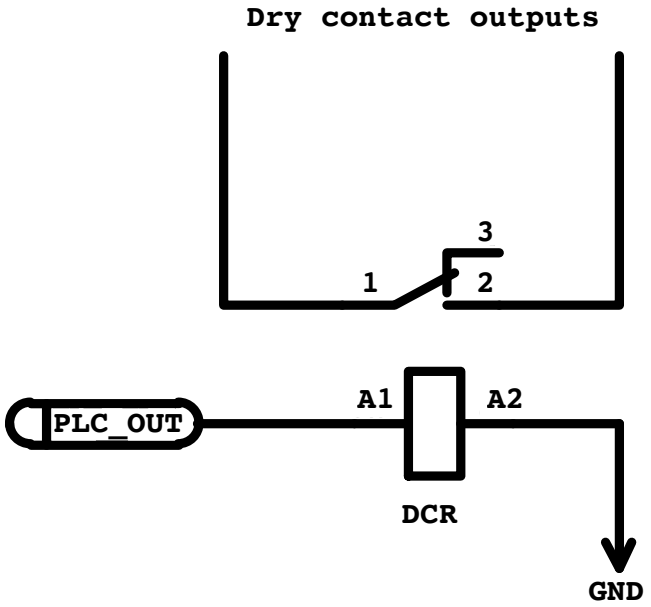

Figure 3.6: Schematic of a dry contact circuit. In normal operational mode, the dry contact relay (DCR) is energised, causing pins 1 and 2 to be connected.

the electronics inside the enclosure must be switched off. To do so, two dry contacts were integrated with the high and low voltage power supplies.

The high voltage power supply used to power the PMs is a CAEN SY4527 [28] which has built-in interlock support. The interlock signal (dry contact) is delivered via the means of a cable fitted with a LEMO 00 connector.

The low voltage supply model for the KTAG is a TTi PL155-P [29], which provides a "remote-off" feature, allowing the power output to be interrupted. The powering off of the low voltage supply is triggered by connecting a pair of contacts, rather than their disconnection, which is the scheme used by the interlocks. To integrate the interlock signal with the TTi supplies, an additional relay was installed to "reverse" the dry contact states, i.e. the contact provided to the low voltage power supply is closed when the interlock is on, and open when it is not. The metal frame built to house the relay and its power supply is shown by figure 3.7.

3.3.2 CEDAR diaphragm motor

The motor which controls the CEDAR diaphragm is located on top of the CEDAR, and can be seen in figure 3.5. To mitigate the risk of the motor coming into contact with a flammable gas mixture, the enclosure is permanently flushed with nitrogen. In order to prevent the operation of the motor in case of failure of the N_2 flushing system, the CEDAR motor interlock in table 3.2 was implemented. The power to the motor is delivered through the interlock dry contact, meaning the power to the motor is cut if the interlock is triggered.

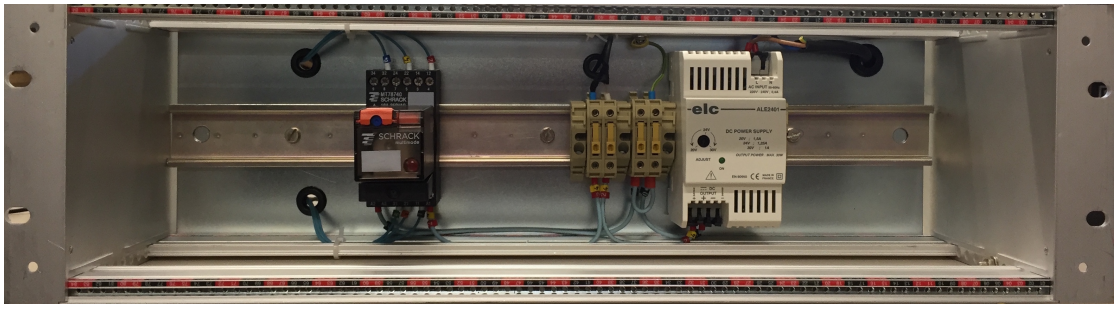

Figure 3.7: Frame housing the relay delivering the interlock signal to the TTi PL155-P low voltage power supplies.

3.3.3 CEDAR diaphragm end-switches

Inside the CEDAR there are two switches, which are designed to stop the diaphragm being damaged by being moved too far in either the opened or closed direction. In order to prevent the switches being energised if the detector is being used with hydrogen, a relay, RL7 in figure 3.8, driven by a dry contact, is used to cut the power to the two end switches simultaneously. To help ensure the safe operation of equipment in explosive atmospheres, the European Union has put in place two directives describing the type of equipment permitted to operate in explosive environments. These directives are commonly known as ATEX [30]. To further mitigate the risk of the end-switches acting as an ignition source, an ATEX rated Pepperl-Fuchs Z779 Zener barrier [31], pictured in 3.8b, was installed, limiting the amount of current allowed to flow to the switches.

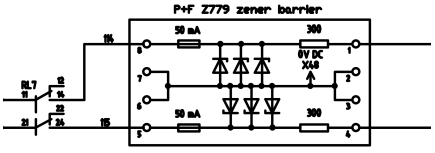

(a) A schematic of the zener diagram circuit.

(b) Photo of the zener barrier in-situ.

Figure 3.8: The P+F Zener barrier and relay number 7 are complementary pieces of safety hardware aiming to prevent the presence of an ignition source inside the CEDAR. A schematic of the barrier wiring is shown on the left, whereas a photo of the relay and barrier in-situ is displayed on the right.

3.3.4 Detector control system

In order to provide status information and warning to NA62 shifters, the state of the diaphragm motor and end switches interlocks was integrated into the KTAG DCS, including a countdown timer for the N_2 flushing of the KTAG enclosure interlock. The state of the interlocks is displayed on the "KTAG environment" panel, shown in figure 3.9. If either of interlocks is triggered, a DCS alarm is raised and an "ERROR" state is propagated along the KTAG FSM.

3.4 Evacuated CEDAR run

The multiple scattering undergone by the particles travelling through the CEDAR is expected to increase the hit rates experienced by downstream detectors. In order to attempt to assess the magnitude of these effects, the CEDAR was evacuated at the end of the 2016 run, and data was taken with the detector volume empty. Purging the nitrogen from the vessel removes the bulk of the material of the CEDAR, making the material budget of the detector similar to that which would be present if it were filled with H_2.

The size of the contribution, due the nitrogen inside the CEDAR, towards downstream detector rate is estimated by comparing the hit rates with the CEDAR filled with N_2, and with it empty. In order to minimise the influence of beam related effects, e.g. intensity or alignment, the data runs used for the study were chosen to have similar intensity and to be close to each other in time. These are listed in table 3.3.

Run	Date	$\overline{\text{Argonion}}[10^9]$	CEDAR status
6291	16/09/2016	0.73	full
6610	20/10/2016	0.78	full
6694	31/10/2016	0.89	full
6761	03/11/2016	0.80	empty
6791	06/11/2016	0.89	empty
6792	06/11/2016	0.86	empty

Table 3.3: A list of the runs used for the empty CEDAR study and their average Argonion counts.

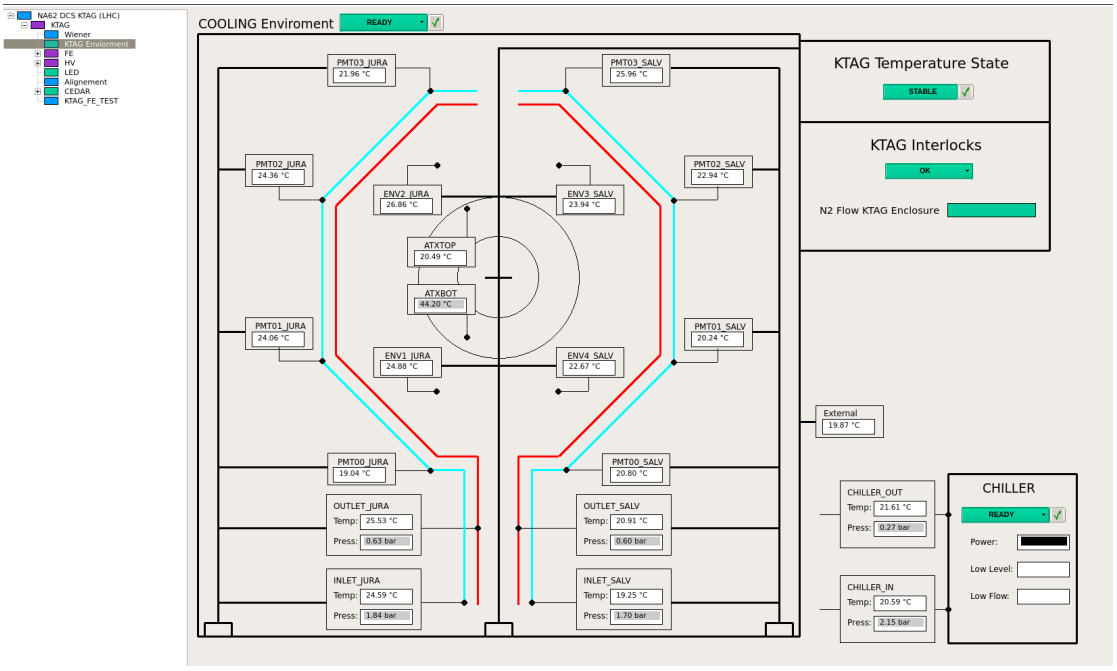

(a) Both enclosure and motor flushing interlocks in OK state.

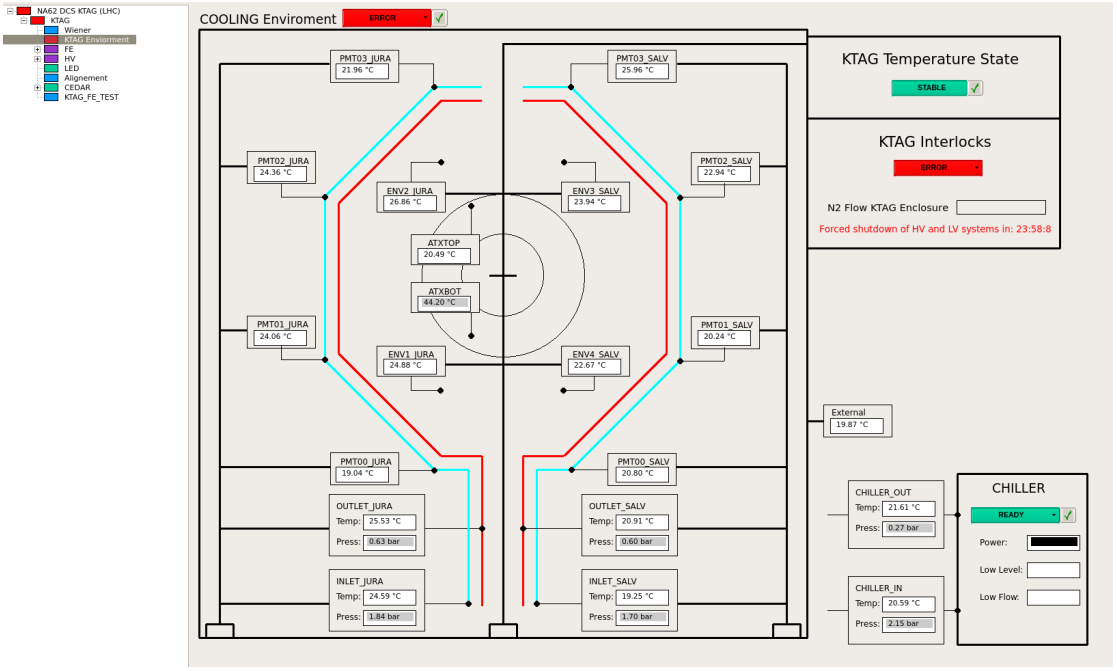

(b) Enclosure N_2 flushing interlock in ERROR state.

Figure 3.9: A screenshot of the environment panel in the KTAG DCS when the interlocks are in operational state (left), and when the N_2 enclosure flushing interlock has been triggered and the countdown has been initiated (right).

An ionization chamber (Argonion) [32] placed at the end of the NA62 experiment is used to estimate the rate of particles entering the experiment. The counts of the Argonion integrated over the entire length of a burst are used to normalise the downstream detector rates. Figure 3.11 shows the Argonion counts over the duration of the six runs used for

the empty CEDAR analysis. An example of the effect of the normalisation is shown in 3.12.

3.4.1 CHANTI rates

The CHANTI is made up of six stations of plastic scintillator placed after the third GTK module. Its purpose is to veto events with activity coming from inelastic interactions of the beam with GTK3. The distances between the CHANTI stations and GTK3 are listed in table 3.4.

CHANTI station	A	B	C	D	E	F
Distance to GTK3 [mm]	27	83	200	430	890	1810

Table 3.4: The spacing of each CHANTI station from GTK3.

The CHANTI hit rates during the six runs analysed are plotted in figure 3.10, with the average rates for each run listed in table 3.5. The variation in rates between the stations is attributed to the varying acceptance for δ-rays originating from quasielastic scattering in GTK3.

The CHANTI station rates averaged over the three full CEDAR runs and the three empty CEDAR runs are listed in table 3.6. The rates in each of the stations decrease by around 7% with the CEDAR evacuated compared with the CEDAR filled with N_2. The average difference in the rates with the CEDAR full/empty is similar to the variation seen within the full/empty run sets.

CHANTI station	$\overline{f_{6291}}$ [MHz]	$\overline{f_{6610}}$ [MHz]	$\overline{f_{6694}}$ [MHz]	$\overline{f_{6761}}$ [MHz]	$\overline{f_{6791}}$ [MHz]	$\overline{f_{6792}}$ [MHz]
A	12.43	13.00	12.64	10.84	11.84	11.91
B	13.53	14.14	13.76	12.03	13.01	13.08
C	13.54	14.11	13.73	12.26	13.15	13.16
D	12.71	13.28	12.96	11.61	12.46	12.46
E	10.82	11.32	11.07	9.53	10.19	10.18
F	11.01	11.54	11.29	10.20	10.82	10.87

Table 3.5: Average rates in each CHANTI station per run.

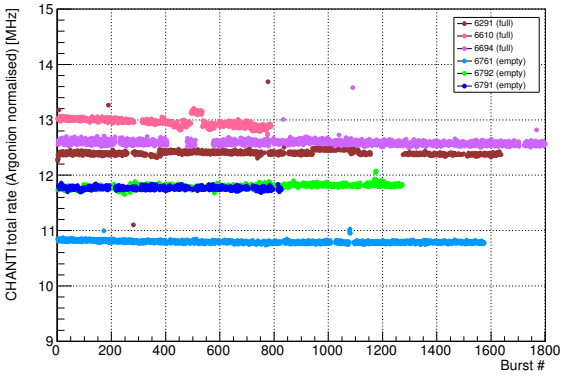

(a) CHANTI station A normalised rates.

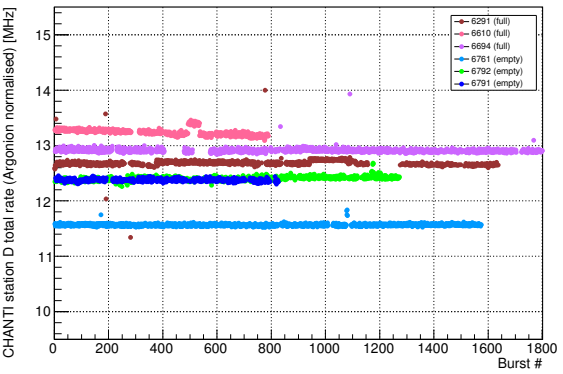

(d) CHANTI station D normalised rates.

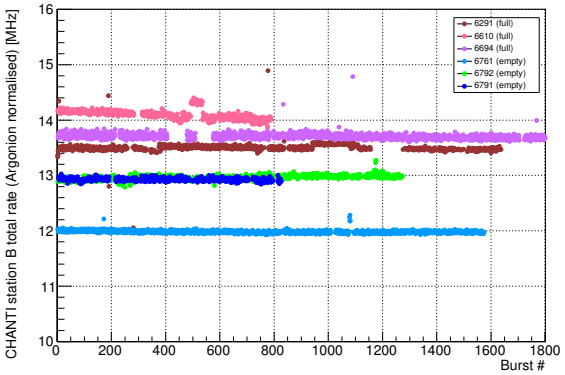

(b) CHANTI station B normalised rates.

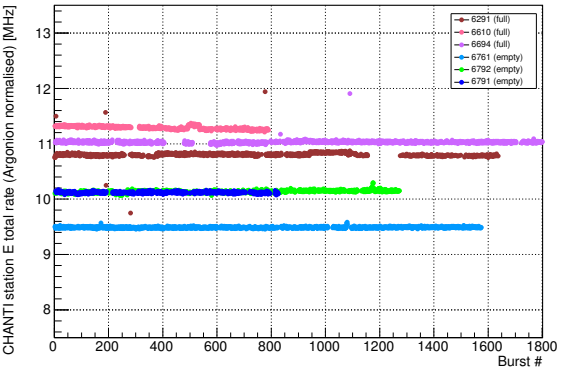

(e) CHANTI station E normalised rates.

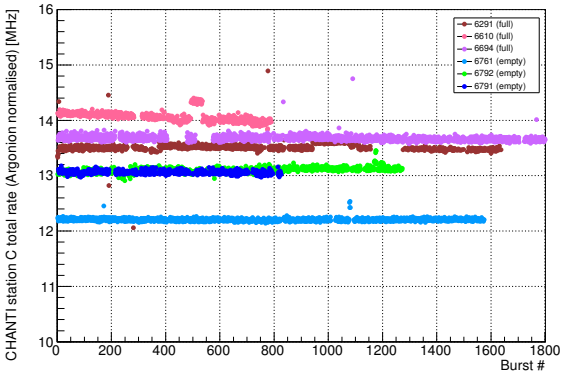

(c) CHANTI station C normalised rates.

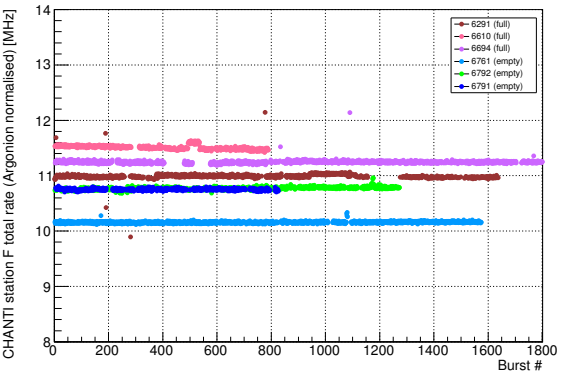

(f) CHANTI station F normalised rates.

Figure 3.10: Argonion normalised hit rates per burst at the six CHANTI stations, for the three full and three empty runs.

3.4.2 LAV rates

The rates for the full and emptied CEDAR runs in each of the twelve LAV stations are shown in figure 3.13, with the average run rates enumerated in table 3.7. For most of the large angle veto stations, runs with the CEDAR filled show an increase of around 4% in

CHANTI station	$\overline{f_{full}}$ [MHz]	$\overline{f_{empty}}$ [MHz]	$\overline{f_{full}}/\overline{f_{empty}}$
A	12.69 ± 0.29	11.53 ± 0.60	1.10 ± 0.06
B	13.81 ± 0.31	12.71 ± 0.59	1.09 ± 0.06
C	13.79 ± 0.29	12.86 ± 0.52	1.07 ± 0.05
D	12.98 ± 0.29	12.18 ± 0.49	1.07 ± 0.05
E	11.07 ± 0.25	9.97 ± 0.38	1.11 ± 0.05
F	11.28 ± 0.27	10.63 ± 0.37	1.06 ± 0.05

Table 3.6: Averaged hit rates between the three full and three empty runs, and their ratio, for each of the six CHANTI stations. The error assigned to $\overline{f_{full}}$ and $\overline{f_{empty}}$ is the standard deviation of the respective run set mean rate

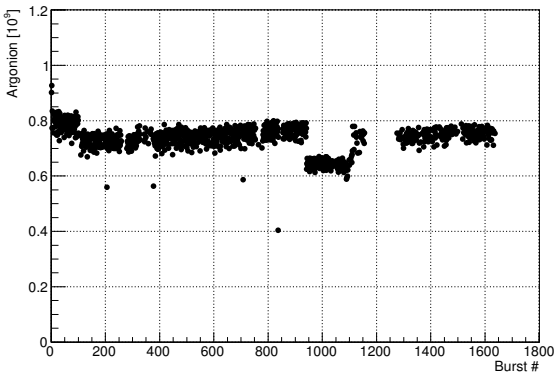

(a) Argonion counts during run 6291.

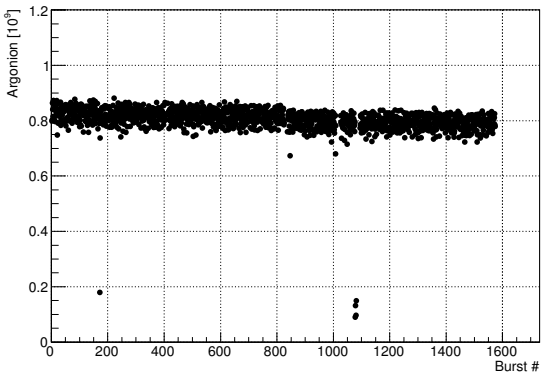

(d) Argonion counts during run 6761.

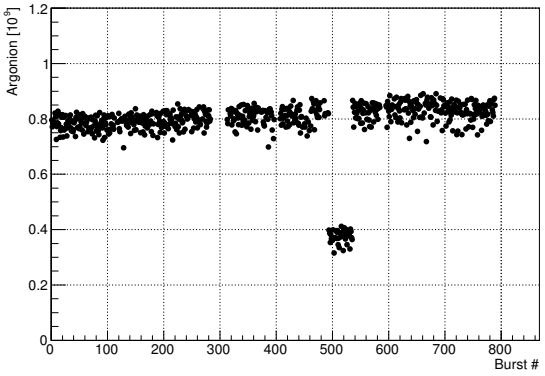

(b) Argonion counts during run 6610.

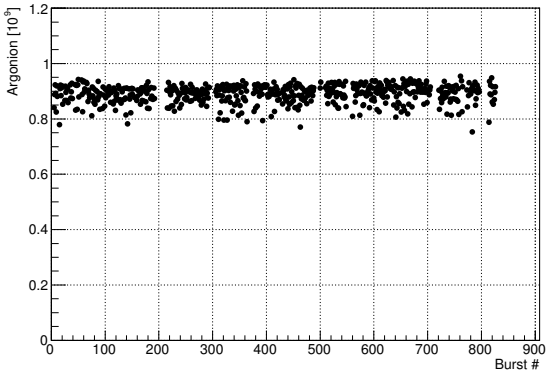

(e) Argonion counts during run 6791.

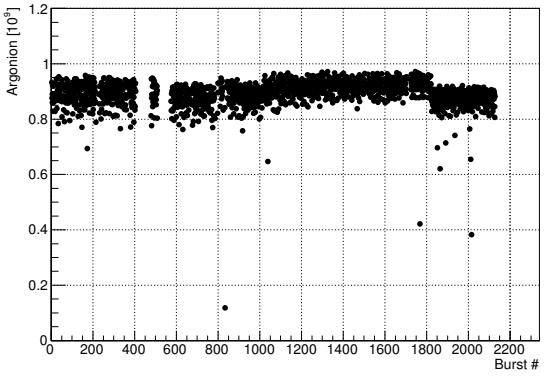

(c) Argonion counts during run 6694.

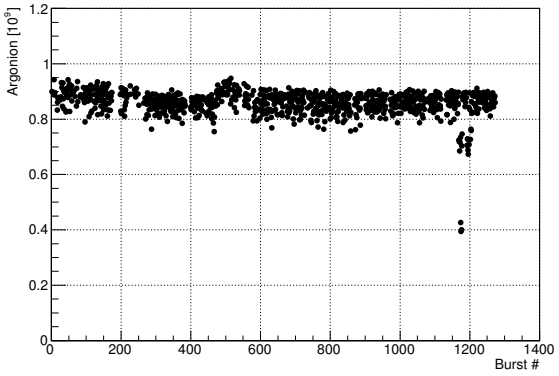

(f) Argonion counts during run 6792.

Figure 3.11: Argonion counts of the six runs used for studying the effect of the N_2 inside the CEDAR.

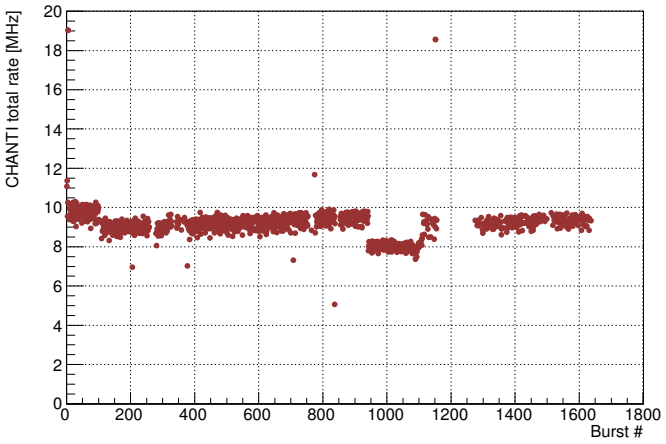

(a) The hit rate of CHANTI station A for run 6291 without normalisation.

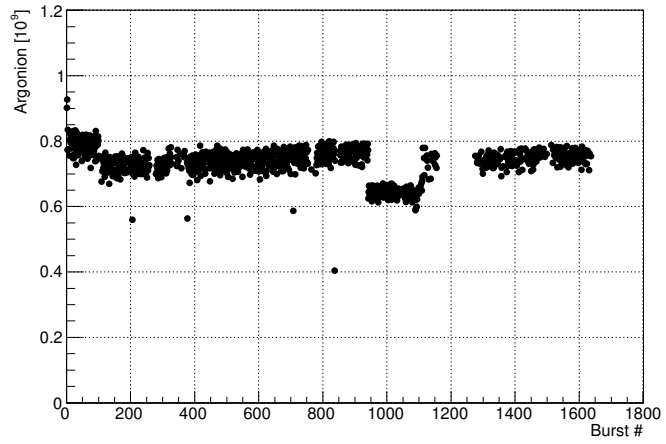

(b) Argonion counts during run 6291.

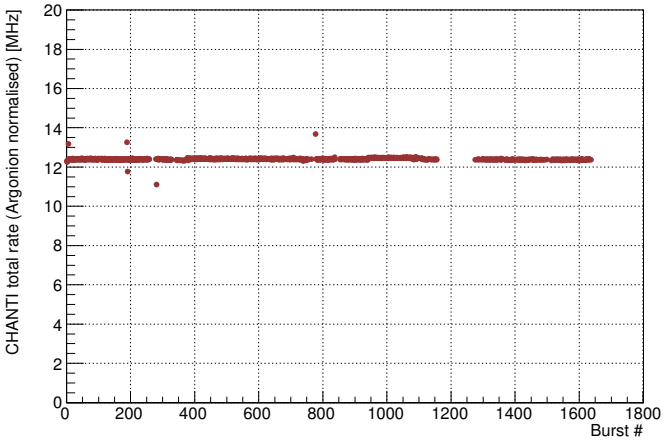

(c) CHANTI station A rate normalised by the Argonion rate.

Figure 3.12: Rate of CHANTI station A during run 6291, before and after Argonion normalisation.

the LAV hit rate with respect to the data taken with Čerenkov volume evacuated. This increase is again comparable to the variation of rates seen between runs belonging to the same CEDAR status run set. In LAV12, the hit rates with the CEDAR evacuated are consistently lower than those when the CEDAR was full, where the decrease in rate is around 10% and the variation within run sets is at the two percent level.

The rates in the LAVs have been shown to be sensitive to the steering and tuning of the beam. These effects do not correlate strongly with the counts given by the Argonion chamber, and can account for the hit rates differences seen between runs where the CEDAR was in the same state. LAVs further upstream have a higher sensitivity to beam related effects.

LAV station	$\overline{f_{6291}}$ [MHz]	$\overline{f_{6610}}$ [MHz]	$\overline{f_{6694}}$ [MHz]	$\overline{f_{6761}}$ [MHz]	$\overline{f_{6791}}$ [MHz]	$\overline{f_{6792}}$ [MHz]
1	13.08	14.09	13.61	12.72	13.31	13.16
2	8.76	9.58	9.18	8.58	9.05	8.87
3	6.61	7.18	6.92	6.49	6.78	6.69
4	6.03	6.52	6.26	5.88	6.13	6.04
5	5.71	6.14	5.93	5.60	5.85	5.72
6	4.97	5.49	5.31	4.96	5.34	5.19
7	4.88	5.33	5.14	4.83	5.04	4.93
8	4.64	5.04	4.89	4.62	4.80	4.72
9	2.93	3.24	3.13	2.94	3.06	2.99
10	2.91	3.17	3.07	2.90	3.02	2.94
11	3.81	4.06	3.91	3.76	3.91	3.81
12	7.77	8.02	7.77	7.04	7.16	7.08

Table 3.7: Averaged LAV station hit rates for each of the six runs used in this study.

LAV station	$\overline{f_{full}}$ [MHz]	$\overline{f_{empty}}$ [MHz]	$\overline{f_{full}}/\overline{f_{empty}}$
1	13.59 ± 0.50	13.06 ± 0.31	1.04 ± 0.05
2	9.17 ± 0.41	8.83 ± 0.24	1.04 ± 0.05
3	6.90 ± 0.28	6.65 ± 0.15	1.04 ± 0.05
4	6.27 ± 0.24	6.02 ± 0.13	1.04 ± 0.05
5	5.93 ± 0.21	5.72 ± 0.12	1.04 ± 0.04
6	5.25 ± 0.27	5.16 ± 0.19	1.02 ± 0.06
7	5.12 ± 0.23	4.93 ± 0.10	1.04 ± 0.05
8	4.86 ± 0.21	4.71 ± 0.09	1.03 ± 0.05
9	3.10 ± 0.16	3.00 ± 0.06	1.03 ± 0.06
10	3.05 ± 0.13	2.95 ± 0.06	1.03 ± 0.05
11	3.94 ± 0.12	3.83 ± 0.07	1.03 ± 0.04
12	7.85 ± 0.15	7.09 ± 0.06	1.11 ± 0.02

Table 3.8: Averaged hit rates between the three full and three empty runs, and their ratio, for each of the twelve LAV sub-detectors. The error assigned to $\overline{f_{full}}$ and $\overline{f_{empty}}$ is the standard deviation of the respective run set mean rate.

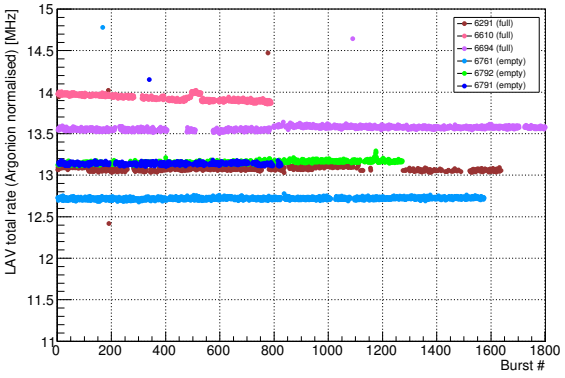

(a) LAV station 1 normalised rates.

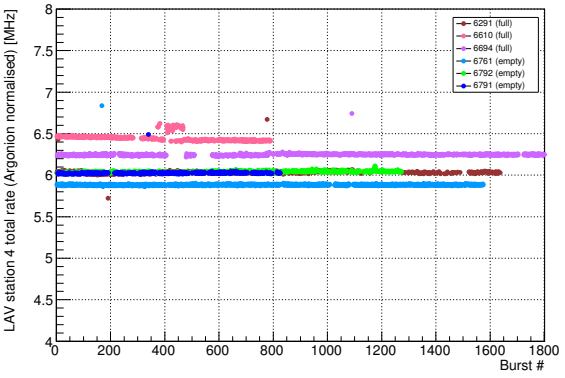

(d) LAV station 4 normalised rates.

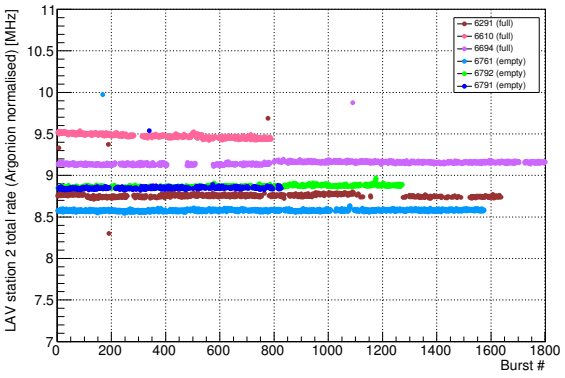

(b) LAV station 2 normalised rates.

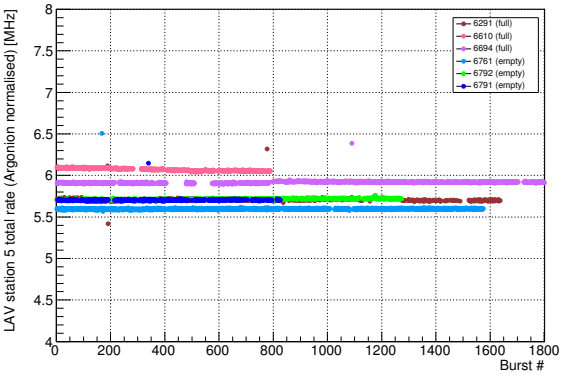

(e) LAV station 5 normalised rates.

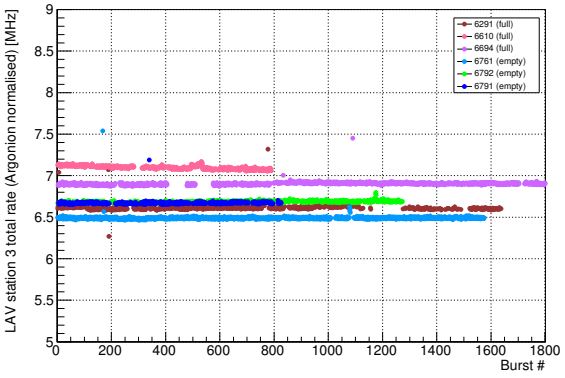

(c) LAV station 3 normalised rates.

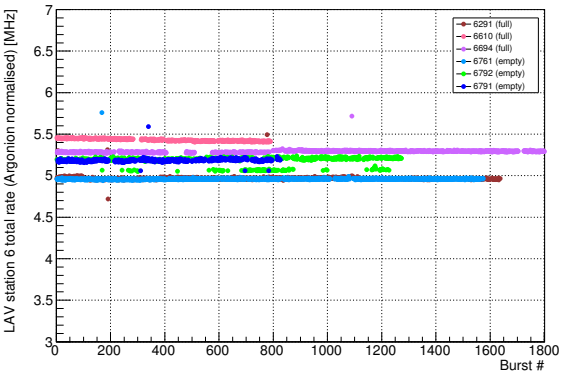

(f) LAV station 6 normalised rates.

Figure 3.13: Hit rates (per burst) at the first six LAV stations normalised to Argonion counts, for the six runs used to study the effect of the N_2 inside the CEDAR.

3.4.3 IRC and SAC rates

The pattern of hit rates observed in the IRC and SAC is similar to that of LAV12, where the increase in the number of hits observed when the CEDAR filled with N_2 versus when it is empty, is consistently above the run variation within the same dataset. The average

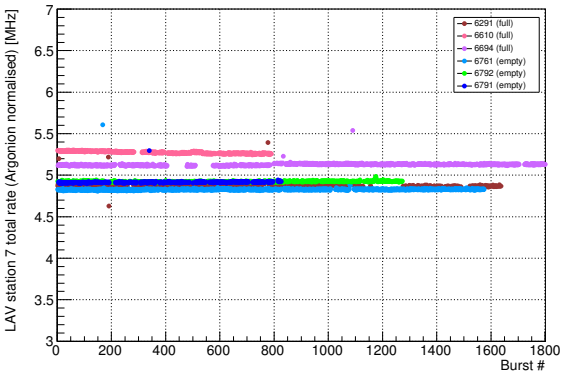

(g) LAV station 7 normalised rates.

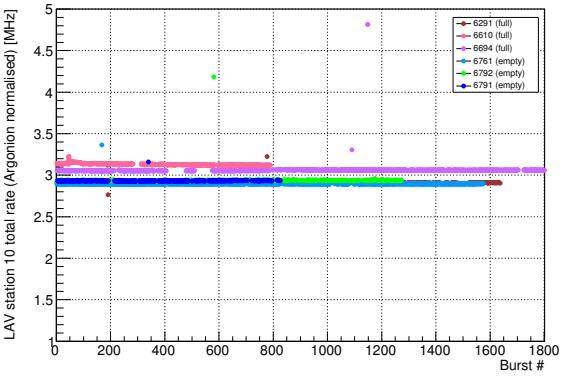

(j) LAV station 10 normalised rates.

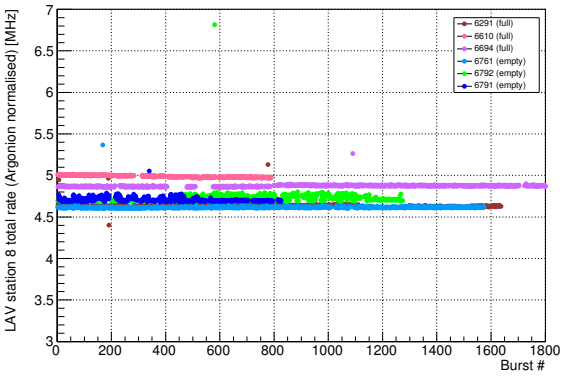

(h) LAV station 8 normalised rates.

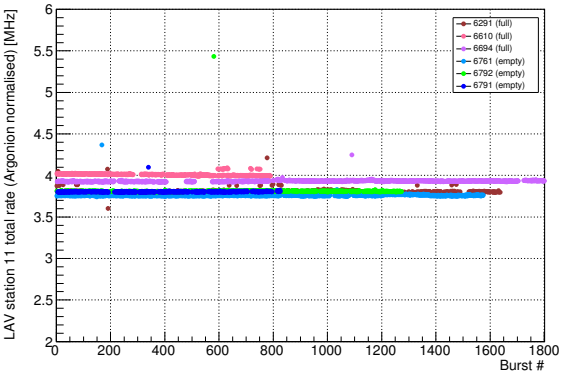

(k) LAV station 11 normalised rates.

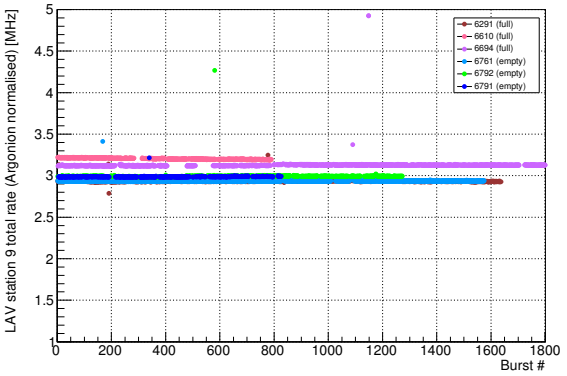

(i) LAV station 9 normalised rates.

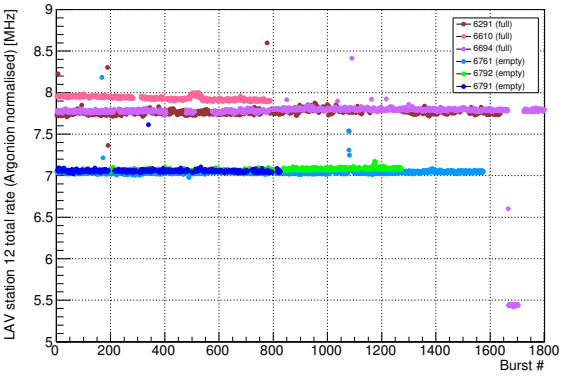

(l) LAV station 12 normalised rates.

Figure 3.13: Hit rates (per burst) at the last six LAV stations normalised to Argonion counts, for the three full CEDAR and three empty CEDAR runs.

hit rates in the small angle calorimeters are summarised in tables 3.9 and 3.10, with the hit rates for each burst of the six runs studied are plotted in figure 3.14. The difference in the full/empty hit rates observed for the SAC is around 4%, which is in-line with the observations from most of the other sub-detectors studied. The IRC shows the highest difference in average rates between the full/empty datasets, which is around 18%. This

difference can be explained by considering the fact that the IRC is placed around the beam pipe, and is particularly sensitive to the beam.

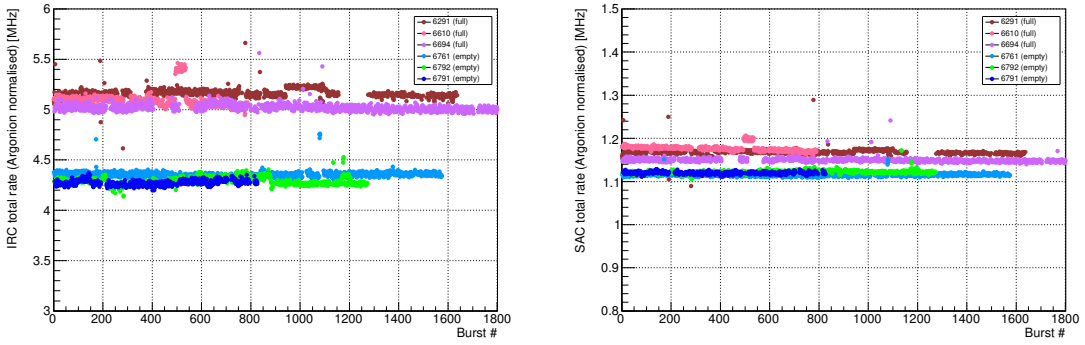

(a) IRC normalised rates.

(b) SAC normalised rates.

Figure 3.14: Hit ates at the IRC and SAC detectors Argonion normalised plotted as a function of the burst number, for the runs taken with the CEDAR full and empty.

SAV detector	$\overline{f_{6291}}$ [MHz]	$\overline{f_{6610}}$ [MHz]	$\overline{f_{6694}}$ [MHz]	$\overline{f_{6761}}$ [MHz]	$\overline{f_{6791}}$ [MHz]	$\overline{f_{6792}}$ [MHz]
IRC	5.16	5.10	5.02	4.35	4.27	4.29
SAC	1.17	1.18	1.15	1.12	1.12	1.12

Table 3.9: Averaged run hit rates of the IRC and SAC, for the two small angle photon veto detectors.

SAV detector	$\overline{f_{full}}$ [MHz]	$\overline{f_{empty}}$ [MHz]	$\overline{f_{full}}/\overline{f_{empty}}$
IRC	5.10 ± 0.07	4.31 ± 0.04	1.18 ± 0.02
SAC	1.16 ± 0.01	1.12 ± 0.00	1.04 ± 0.01

Table 3.10: Averaged hit rates between the three full and three empty runs, and their ratio, for two small angle veto detectors. The error assigned to $\overline{f_{full}}$ and $\overline{f_{empty}}$ is the standard deviation of the respective run set mean rate.

3.5 Summary

Running the CEDAR with H_2 reduces the hit rate in downstream detectors. The drop in rate observed in the detectors studied, except from LAV12, IRC, and SAC, is similar in magnitude to the variation in rates seen during the normal data taking. The rate reduction in LAV12, IRC, and SAC is more significant when compared to the run-to-run variation. This suggests that using the CEDAR with H_2 would bring tangible improvements to the $\pi\nu\bar{\nu}$, if complemented by improved stability of beam conditions. To quantify the benefit of the reduced scattering, one would have to perform a full $\pi\nu\bar{\nu}$ analysis, with the KTAG filled with H_2. As discussed earlier, the benefit of the reduced

scattering may well be cancelled out by the reduction in the KTAG performance, if the CEDAR optics are not modified for H_2 operation. To take $\pi\nu\bar{\nu}$ data with the CEDAR filled with hydrogen as is, i.e. without H_2 optimised optics, would require taking dedicated H_2 data to assess the performance of the $\pi\nu\bar{\nu}$ analysis, and potentially re-optimise it.

With the end of the first NA62 data-taking period in November 2018, and the desire to start taking $\pi\nu\bar{\nu}$ data in earnest in 2021, the NA62 collaboration has taken the decision not to use the current CEDAR with H_2. Instead, the strategy adopted by NA62 is to take $\pi\nu\bar{\nu}$ data with the current CEDAR configuration, and in parallel adapt a different CEDAR for H_2 operation. This work has already begun, and the new CEDAR is expected to be ready for the 2022 data-taking period. In this way, NA62 will benefit from a CEDAR with a lower material budget and no performance degradation, while maximising the amount of data collected.

Chapter 4

K_{l3} branching fraction measurement strategy

Performing a precision measurement of branching fractions, which is the aim of the analysis presented in this thesis, generally requires two ingredients: a large number of signal events resulting in a low statistical error, and a good control of systematic effects that also contribute to the overall uncertainty. A common method of reducing systematic effects when studying the branching fraction of a particular channel is to use a "normalisation" channel. The normalisation channel generally has a similar decay signature to the mode of interest, allowing the bulk of the event selection for both channels to be the same. In this way, when one takes the ratio between the branching fraction of the two decays, many systematic effects will cancel, at least to first order. Not performing any particle identification in the fit selection, e.g. using the calorimeters or the RICH, allows for control samples enriched in particular decay modes to be selected. These control samples can be used to study the agreement data and simulation, and to implement any required corrections.

This is the strategy adopted for the K_{l3} branching fraction measurement. A common selection is used to isolate events that have a single downstream positively charged track matched to a K^+ and a π^0. This is the signature of the two K_{l3} channels of interest, $K_{\mu 3}$ and K_{e3}, as well as the $K_{2\pi}$ decay, which will serve as the normalisation channel. Two

versions of the analysis have been studied: one where the downstream track is matched a kaon as reconstructed by the Gigatracker, the other does not include the GTK and makes use of a "nominal" kaon.

The resulting data sample will be a mixture of different decays, where the contribution of each source, or sample strength, will be proportional to the branching fraction and acceptance of the decay mode. Therefore if the contribution strength and acceptance of each decay channel is known, one can extract the branching fraction.

The acceptance of each decay mode can be obtained from a simulation, with the formula:

$$\epsilon_j = \frac{n_j^{accepted}}{n_j^{generated}}, \tag{4.1}$$

where ϵ_j is the acceptance for decay mode j, $n_j^{generated}$ is the number of decay events generated, and $n_j^{accepted}$ is the number of events passing the selection. simulation can also be used to predict the distributions of different variables which will change between the various decay channels. The sum of these distributions, in the (unknown) correct proportions, should be the same as that obtained from data using the same selection. The decay channel fractions present in the data sample can be determined by performing a fit of the variable distributions obtained from simulation to the same data distributions, where the floated parameters are the sample strengths.

The problem of fitting distributions from multiple Monte Carlo samples to data is addressed by Barlow and Beeston in [33]. The article specifically addresses the issues of using simulation samples that are limited in size and using distributions that may contain bins with low event counts. Both of these issues are pertinent to this analysis, hence the Barlow-Beeston method was used to perform the sample fraction fit. The strategy of using a common selection to obtain a mixed sample, which is then used for the channel branching fractions fit also has the advantage of boosting the number of signal events for each channel, as no specific selection is made to isolate individual pure samples.

Section 4.1 describes the selection used to obtain the data and simulation samples on which the fraction fit is performed, including upstream-downstream track matching with

and without the GTK, π^0 tagging, and trigger conditions. The principles of the Barlow-Beeston method, and its application to this analysis are discussed in section 4.2.

4.1 Event selection

The experimental signatures of the three processes of interest, $K^+ \to \pi^0\mu^+\nu_\mu$, $K^+ \to \pi^0 e^+\nu_e$, and $K^+ \to \pi^+\pi^0$, all have a single charged track and a π^0 in their final state, with the dominant decay of the neutral pion being $\pi^0 \to \gamma\gamma$. The neutrino from the K_{l3} decays leaves the experiment undetected. Therefore, exactly the same selection criteria for the three decays can be used, with the decay discrimination performed by the sample fraction fit.

4.1.1 Trigger

The trigger used for event selection is a minimum-bias trigger, designated as the "control" trigger of the experiment. Its sole condition is the presence of at least 2 hits in the NA48-CHOD. The generation of control triggers is downscaled by a factor 400 in order to prevent an unsustainably high rate. At a downscale of 400, the control trigger already takes up 30% of the available data read-out bandwidth.

4.1.2 Filter

After the data has been centrally processed, it is split into several different filter streams designed to provide reduced datasets for the various NA62 analyses. This analysis makes use of the control stream, part of the filter designed for the $\pi\nu\bar{\nu}$ measurement. The stream contains all control triggered events that pass a minimum bias selection criteria. For an event to be accepted through the filter, it must contain at least one hit in the horizontal and vertical planes of the same quadrant of the NA48-CHOD. Additionally, successfully filtered events must contain at least one reconstructed STRAW track which satisfies the following conditions:

- Track reconstructed in all four STRAW chambers

- STRAW candidate is in the acceptance of NA48-CHOD, LKr, and MUV3
- STRAW track is loosely matched to a NA48-CHOD hit pair, using a discriminant of the same form as equation 4.2
- Spectrometer candidate must be in time with at least one hit in each GTK station. The track time is taken to be the time of NA48-CHOD or the time of the KTAG candidate, with at least four sectors, closest to the the NA48-CHOD time within a 5 ns window, if one exists.

4.1.3 Downstream track selection

The downstream track selection isolates events with exactly one "good" downstream track. A "good" downstream track is a STRAW track reconstructed in all four STRAW chambers, which has associations with all of the relevant downstream detectors. Events with more than ten reconstructed STRAW tracks are rejected.

The spectrometer reconstruction algorithm clusters STRAW hits in groups of views, chambers, chambers pairs, and finally multi-chamber tracks. The final track parameters, e.g. slopes and momentum, are extracted via the means of an iterative least squares fit (LSF), which removes hits too far from the predicted track trajectory. For a STRAW track to be considered of "quality", it must have a fit $\chi^2 < 20$, and the difference between the estimated track momentum before and after the fit must less than 20 GeV/c. Additionally, the K_{l3} selection only accepts tracks reconstructed in all four chambers, and with a positive charge.

A preliminary condition for associating STRAW tracks to other downstream detectors, is that the extrapolated track position at the relevant detector plane falls within the active area of the detector, e.g. the track is in the detector geometrical acceptance. The acceptance conditions for the NA48-CHOD, CHOD, LKr and MUV3 are described in table 4.1.

If a track is found not to satisfy the conditions in table 4.1, it is rejected. Once a track has been determined to be of "quality" and in the geometrical acceptance, an attempt is

Detector	$(x, y)_{centre}$ [mm]	z [mm]	R_{low} [mm]	R_{high} [mm]
STRAW chamber 1	(101.2, 0)	183 508	75	1000
STRAW chamber 2	(114.4, 0)	194 066	75	1000
STRAW chamber 3	(92.4, 0)	204 459	75	1000
STRAW chamber 4	(52.8, 0)	218 885	75	1000
CHOD	(0,0)	238 131	140	1070
NA48-CHOD V plane	(0,0)	239 009	130	1100
NA48-CHOD H plane	(0,0)	239 389	130	1100
LKr	(0,0)	241 093	150	1130
MUV3	(0,0)	246 800	130	2400

Table 4.1: Geometrical acceptance conditions for the relevant downstream detectors. For the STRAW, NA48-CHOD, and CHOD, the track (x, y) position must fall within the area outlined by two circles with radii R_{low} and R_{high}. The LKr acceptance is defined by an inner circle with a radius of R_{low} and an outer octagon with an apothem of R_{high}. The acceptance area of MUV3 is constructed by an inner circle with radius of R_{low} and a square with a side of R_{high}.

made to match it with candidates in the NA48-CHOD, CHOD, and LKr. The track is first matched with the NA48-CHOD, which has a time resolution of 0.2 ns. If a STRAW track is successfully matched with a NA48-CHOD candidate, the time of the candidate is used alongside the time obtained from the spectrometer (STRAW time resolution of around 5 ns), to make the rest of the detector matches.

The matching algorithm starts by looking for STRAW-NA48-CHOD candidate associations. A STRAW track and a NA48-CHOD candidate are considered associated if the extrapolated track position at the NA48-CHOD z plane, directly intersects the horizontal and vertical slabs belonging to the hodoscope candidate, or is within 20 mm of their edges [34]. For each association, a discriminant is built using the distance between the track and the NA48-CHOD candidate and their time difference:

$$D_{NA48\text{-}CHOD} = \left(\frac{|X_{STRAW} - X_{NA48\text{-}CHOD}|}{2\sigma_X}\right)^2 + \left(\frac{|T_{STRAW} - T_{NA48\text{-}CHOD}|}{3\sigma_T}\right)^2, \quad (4.2)$$

where $X_{NA48\text{-}CHOD}$ is the (x, y) position of the NA48-CHOD candidate, as taken from the central coordinates of the corresponding slabs, X_{STRAW} is the extrapolated position of the track, $T_{NA48\text{-}CHOD}$ is the candidate time, and T_{STRAW} is the time of the track as measured by the spectrometer. $\sigma_X = 13$ mm, $\sigma_T = 5.6$ ns.

Matching the charged hodoscope candidates to STRAW tracks in both time and space reduces the chances of matching a STRAW track to an accidental NA48-CHOD candidate occurring at the same point in time or space. Figure 4.1 shows the variables used to construct the discriminant NA48-CHOD (left), and the form of the discriminant itself (right). The pair with the lowest discriminant is taken, and it is considered matched if:

- $D_{NA48-CHOD} < 10$
- $|T_{STRAW} - T_{NA48\text{-}CHOD}| < 20$ ns

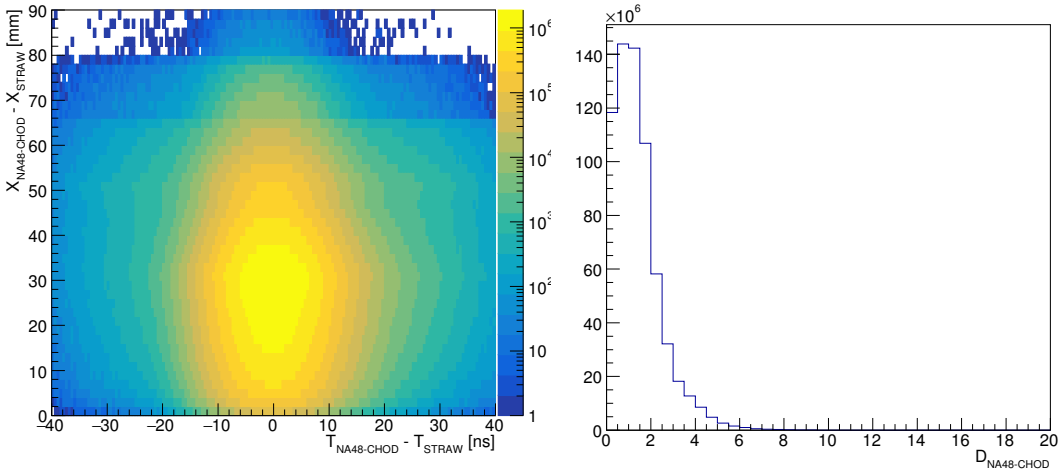

(a) $X_{STRAW} - X_{NA48\text{-}CHOD}$ vs. $T_{STRAW} - T_{NA48\text{-}CHOD}$

(b) $D_{NA48-CHOD}$

Figure 4.1: A plot of the spatial and temporal variables used to build $D_{NA48-CHOD}$ are shown on the left, with the distribution of the resulting discriminant on the right.

If a track is successfully matched with NA48-CHOD, the CHOD matching procedure is performed. The position of the charged track at the CHOD plane is calculated, and if distance between the track and a CHOD candidate is less than the search radius, r_{search}^{CHOD}, a STRAW-CHOD associated pair exists. r_{search} is dependent on the momentum of the track according to:

$$r_{search}^{CHOD} = \begin{cases} 0.07 + \frac{47.3}{P_{track}}\text{mm}, & \text{if } P_{track} > 1 \text{ GeV/c.} \\ 47.37\text{mm}, & \text{otherwise} \end{cases} \tag{4.3}$$

The momentum dependence of the search radius is an artefact of the detector association tool [35]. The association algorithm was originally developed for the MUV3 detector, which has a significant amount of material in front of it, necessitating the momentum dependence in order to account for multiple scattering.

For each CHOD-STRAW track association, a discriminant is built using the relation:

$$D_{CHOD} = \left(\frac{|X_{CHOD} - X_{STRAW}|}{3\sigma_X}\right)^2 + \left(\frac{|T_{CHOD} - T_{STRAW}|}{2\sigma_T}\right)^2, \tag{4.4}$$

where X_{CHOD} is the (x, y) position of the CHOD candidate, as taken from the central coordinates of the corresponding tile, X_{STRAW} is the extrapolated position of the track, T_{CHOD} is the candidate time, and T_{STRAW} is the time of the track as measured by the spectrometer. $\sigma_X = 16$ mm and $\sigma_T = 7$ ns. The shape of the discriminant and the two variables which are used to build it are shown in figure 4.2.

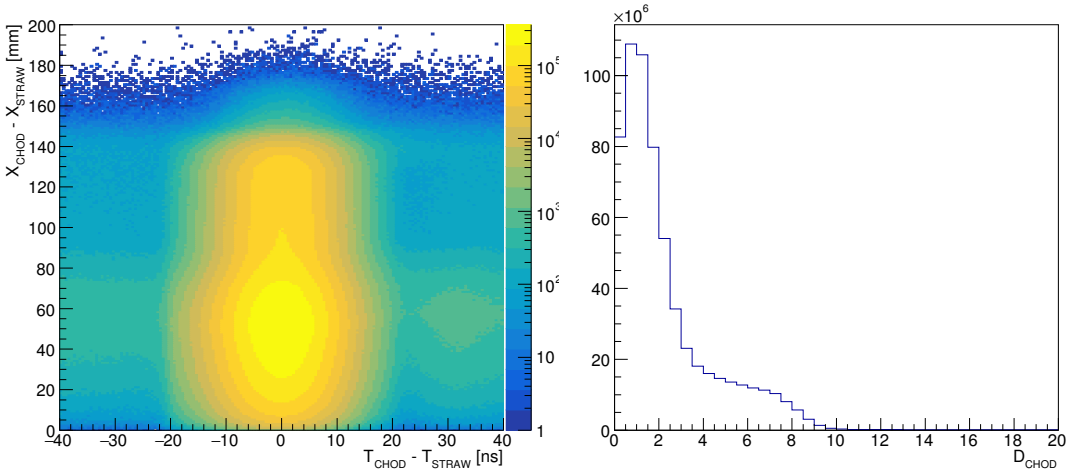

(a) $X_{CHOD} - X_{STRAW}$ vs. $T_{CHOD} - T_{STRAW}$ (b) D_{CHOD}

Figure 4.2: A plot of the distance between associated STRAW-CHOD candidates versus their time difference is shown on the left, with the resulting discriminant distribution displayed on the right.

The pair with the lowest discriminant is considered matched, if the following conditions are met:

- $D_{CHOD} < 10$
- $|T_{CHOD} - T_{NA48\text{-}CHOD}| < 5$ ns.

The tighter $|T_{CHOD} - T_{NA48\text{-}CHOD}|$ cut with respect to $|T_{STRAW} - T_{NA48\text{-}CHOD}|$ represents the better time resolution of the CHOD, which is $\mathcal{O}(1\text{ns})$.

Once a track has been matched with an NA48-CHOD and CHOD candidate, the LKr matching algorithm is run [36]. For each LKr cluster, a discriminant is built according to:

$$D_{LKr} = \left(\frac{|X_{LKr} - X_{STRAW}|}{\sigma_X}\right)^2 + \left(\frac{|T_{LKr} - T_{STRAW}|}{\sigma_T}\right)^2, \tag{4.5}$$

where X_{LKr} is the (x, y) position of the LKr cluster, X_{STRAW} is the extrapolated position of the track at the LKr plane, T_{LKr} is the cluster time, and T_{STRAW} is the time of the track as measured by the spectrometer. $\sigma_X = 20$ mm and $\sigma_T = 5$ ns. The track cluster pair with the lowest discriminant is taken, and the LKr cluster is considered associated to the track if the criteria below are met:

- $|X_{LKr} - X_{STRAW}| < 60$ mm
- $|T_{LKr} - T_{STRAW}| < 15$ ns.

An auxiliary cluster reconstruction is run at the analysis level, if no associated cluster is found [36]. The algorithm attempts to form a cluster using LKr hits around the track impact position, which meet the following conditions with respect to the track:

- $|X_{hit} - X_{STRAW}| < 60$ mm
- $|T_{hit} - T_{STRAW}| < 25$ ns.

The most energetic LKr hit passing the above criteria is designated as the seed hit, and must have an energy deposit of at least 40 MeV.

A track associated LKr cluster is considered matched if the following criteria are satisfied:

- $|X_{STRAW} - X_{LKr}| < 100$ mm
- $|T_{LKr} - T_{NA48\text{-}CHOD}| < 6$ ns

- $|T_{LKr} - T_{CHOD}| < 6$ ns
- $|T_{LKr} - T_{STRAW}| < 20$ ns.

The times of the successfully matched candidates of the NA48-CHOD, CHOD, and LKr are combined with the STRAW track time to form the "downstream time", according to equation 4.6, marking the end of the downstream track selection.

$$T_{downstream} = \frac{\sum_{i=1}^{4} w_i T_i}{\sum_{i=1}^{4} w_i}, \tag{4.6}$$

here $i = 1, 2, 3, 4$ are the indices for the NA48-CHOD, CHOD, STRAW, and LKr respectively. T_i is the time of each matched detector reconstructed candidate, and the values of $w_{1,2,3,4}$ are 2, 1.5, 1, and 0.1 ns^{-1}. The weight, w_i, given to each detector time reflects the time resolution of the detector in question.

4.1.4 Downstream-upstream track matching

4.1.4.1 KTAG matching

The downstream track time is used to match the STRAW track to an incoming kaon that has been identified by the KTAG. The matching algorithm only considers KTAG candidates that have hits in at least 5 out of the 8 sectors. The procedure selects the KTAG candidate, with time T_{KTAG}, closest to $T_{downstream}$ within a 2 ns window. If there is no KTAG candidate with 5 sectors, within that time window, the event is rejected. If the downstream track is successfully matched with a KTAG candidate, the time of the KTAG candidate is used for any further associations. This is due to the fact that the KTAG has a lower time resolution, $\mathcal{O}$(70ps), compared to the detectors entering in the computation of the downstream track time.

4.1.4.2 GTK matching

The GTK matching procedures make use the two variables: ΔT and CDA. ΔT is defined as $\Delta T = T_{KTAG} - T_{GTK}$, where T_{GTK} is the time of each GTK matching

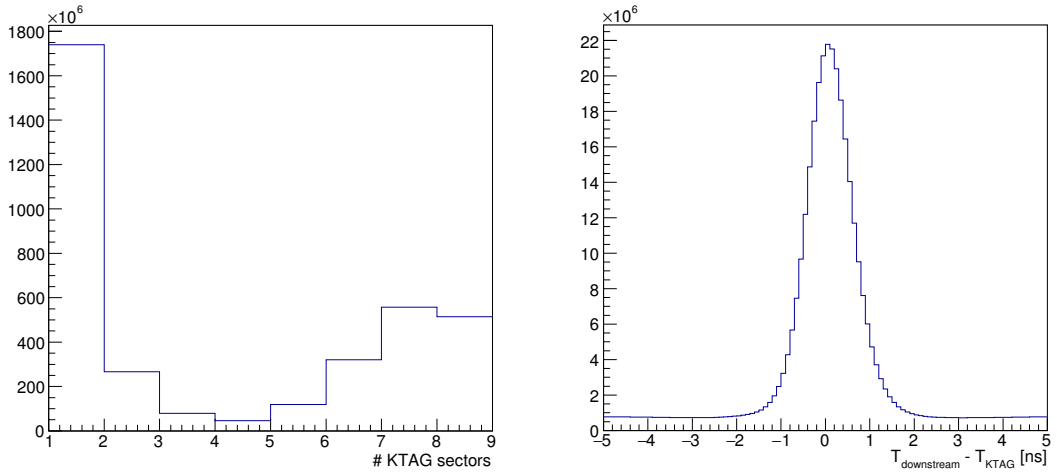

(a) Number of sectors per KTAG candidate.

(b) $T_{downstream} - T_{KTAG}^{candidates}$

Figure 4.3: A plot of the KTAG candidate sector distribution is shown on the left, with the difference in time with respect to $T_{downstream}$ plotted on the right.

candidate and T_{KTAG} is the time of selected KTAG candidate. The second variable, CDA, is the closest distance of approach between the selected STRAW track and the GTK candidates being considered. The CDA is calculated using the positions and directions of the STRAW and GTK tracks. The matching algorithm combines these two variables into a discriminant, $D(CDA, \Delta T)$ [37]:

$$D(CDA, \Delta T) = [1 - p(CDA)] \cdot [1 - p(\Delta T)], \tag{4.7}$$

where $p(CDA)$ and $p(\Delta T)$ are the probabilities of CDA and ΔT belonging to signal like events, i.e. the particle reconstructed in the STRAW originates from the kaon reconstructed in the GTK. $p(CDA)$ and $p(\Delta T)$ are calculated according to the following two relations:

$$p(CDA) = \int_0^{CDA} f(CDA')d(CDA'), \tag{4.8}$$

$$p(\Delta T) = \int_{-\Delta T}^{+\Delta T} f(\Delta T')d(\Delta T'). \tag{4.9}$$

$f(CDA')$ and $f(\Delta T')$ are the signal probability density functions for the CDA and ΔT respectively, which are obtained from the analysis of $K^+ \to \pi^+\pi^+\pi^-$ decays. The form of the two PDFs is illustrated in figure 4.4.

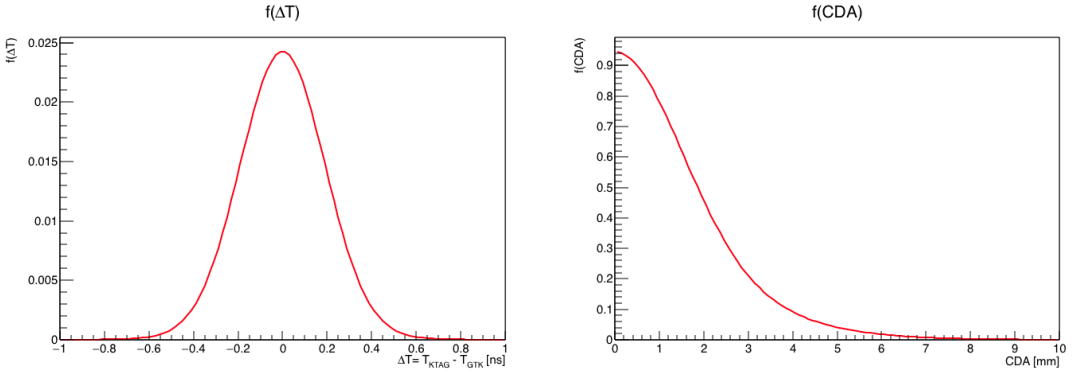

(a) $f(\Delta T)$. (b) $f(CDA)$.

Figure 4.4: A plot of the signal probability density functions for ΔT(left) and CDA (right), used for K^+ downstream track matching.

$D(CDA, \Delta T)$ is only built for downstream-GTK track pairs which meet the condition: $|\Delta T| < 0.3$ ns. The downstream-upstream track pair with the highest discriminant is taken, and is considered matched if it meets the following conditions:

- $D(CDA, \Delta T)$ ¿ 0.01
- $CDA < 5$ mm.

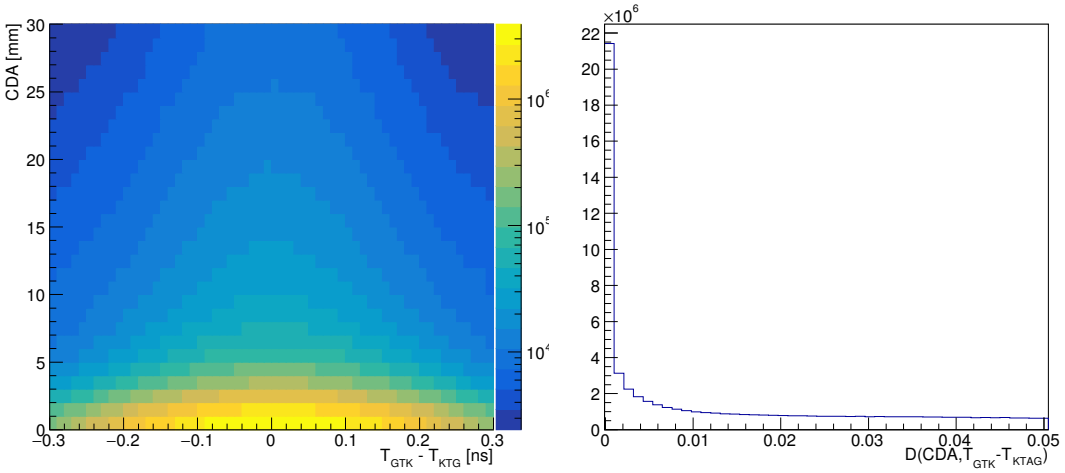

(a) CDA vs. ΔT (b) $D(CDA, \Delta T)$

Figure 4.5: Plots of the CDA against ΔT (left) and $D(CDA, \Delta T)$ (right), for the kaon-downstream track pairs with the highest $D(CDA, \Delta T)$.

The decay vertex of matched upstream-downstream tracks is calculated by taking the mid-point on the line of closest approach between the two track trajectories. The distributions of the (x, y) and z positions of the decay vertices are shown in figure 4.6. In order to select decays occurring in the fiducial volume, only decays with z vertex in the range of 110 m and 180 m are accepted.

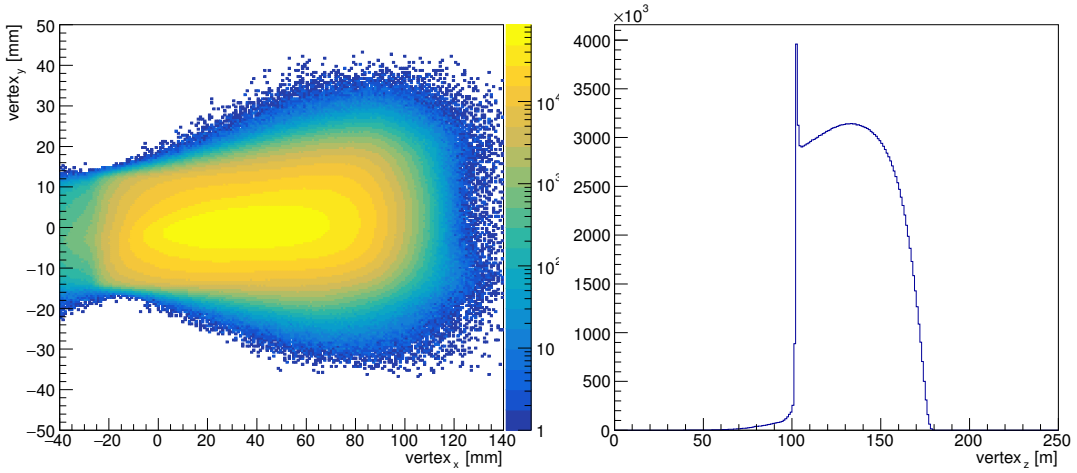

(a) Charged decay vertex (x, y) (b) Charged decay vertex z

Figure 4.6: A plot of the transversal (left) and longitudinal (right) positions of the charged decay vertex.

4.1.4.3 Nominal kaon matching

Rather than using kaon candidates reconstructed by the Gigatracker, the selected downstream track is matched to a kaon reconstructed from measured parameters of the beam in the data [38]. Such kaons are referred to as "nominal" kaons throughout this work. The beam parameters used to construct a nominal kaon, are measured on a run by run basis, and include the beam central momentum, the dx/dz and dy/dz slopes, and the (x, y) positions at $z = 102.4$ m. The decay vertex and CDA between the kaon and the charged track are calculated using the same method as in section 4.1.4.2. Due to the fact that the CDA resolution is higher without the use of the GTK, the CDA cut is relaxed to 8 mm. The cuts of the z coordinate of the decay vertex remain as: $110 < z_{vertex} < 180$ m.

4.1.4.4 Magnetic field correction

As charged particles travel through the fiducial volume, their direction is altered by Earth's magnetic field and residual magnetisation of the vacuum vessel. A field map of the magnetisation inside the FV was created by NA62 collaboration, and is used to correct the track directions. Once the charged vertex has been computed, the particle slopes are corrected for the effect of the magnetic field, and the vertex is recalculated with the new particle directions.

In order to reduce background events stemming from inelastic interactions of beam particles in the last GTK station, events which have CHANTI activity within 3 ns of T_{KTAG} are rejected.

4.1.5 π^0 tagging

The reconstruction of neutral pions relies on information from the charged vertex of the K^+ (either GTK or nominal) matched to the charged track, and the reconstructed LKr clusters originating from the process $\pi^0 \to \gamma\gamma$. The first step of the algorithm is to identify "quality" photon candidates. For an LKr cluster to qualify as such, it must be at least 20 mm away from a dead cell, so that none of the γ energy is lost due to the non-functional channel. The cluster must also be at least 30 mm away from another LKr cluster in order to avoid energy sharing between clusters. The cluster must not be associated to a STRAW track, and its shape must be electromagnetic like. The cluster energy, E_γ, must be above 2 GeV, imposing this cut removes the part of the E_γ spectrum where there are significant differences in the non-linear response of the LKr between data and simulation.

The direction of the each photon candidate is calculated using the (x, y) positions of the LKr cluster, the z position of the LKr front plane (z_{LKr}) and the (x, y, z) of the charged decay vertex. Combining the direction of the γ with the measured energy from the LKr cluster, one can construct the γ four momentum.

If there are at least two photon candidates, a π^0 candidate is reconstructed with each possible photon pair, with the π^0 four momentum calculated as

$$P_{\pi^0} = P_{\gamma 1} + P_{\gamma 2}, \tag{4.10}$$

where $\gamma_{1,2}$ are the four momenta of the two photons. The photon with the lower energy out of the two is designated as γ_1.

For a neutral pion candidate to be classified as of "quality", it must meet several different conditions. The two photons forming the π^0 must be at least 300 mm away from each other as to avoid energy sharing between the clusters. Their time difference, $|T_{\gamma 1} - T_{\gamma 2}|$, must be less than 4 ns, suppressing photon pairs originating from different sources. The time of the neutral pion, $T_{\pi^0} = \frac{T_{\gamma 1}+T_{\gamma 2}}{2}$, must be within 4 ns of T_{KTAG}, helping to ensure the track and the π^0 emanate from the same decay. The neutral z vertex of the reconstructed π^0 must be in the range 110-180 m. The π^0 vertex is calculated using the formula:

$$z_{\pi^0}^{vertex} = z_{LKr} - \frac{\sqrt{E_{\gamma 1} E_{\gamma 2} d_{12}}}{m_{\pi^0}^{PDG}}, \tag{4.11}$$

where $m_{\pi^0}^{PDG} = 134.98$ MeV/c^2, the Particle Data Group (PDG) value for the π^0 mass, and d_{12} is the distance between the two LKr clusters.

Finally, the reconstructed mass of the π^0, $m_{\pi^0}^{reco}$, must be within 10 MeV/c^2 of the PDG value, $m_{\pi^0}^{PDG}$. Events which have fewer or more than one tagged π^0 are rejected.

4.2 Sample fraction fit

4.2.1 Barlow-Beeston method

Binning one or more of the distributions discussed in section 4.2.2 into a histogram with n bins results in a set of numbers $\{d_1, d_2, d_3, ..., d_n\}$, where d_i represents the number of data events which enter into bin i. For each bin, there is also a predicted number of

events f_i, which is given by summing the distributions of the simulation samples. For m simulation samples, the predicted number of events in individual bins is given by:

$$f_i = N_D \sum_{j=1}^{m} \frac{P_j}{N_j} a_{ji}, \tag{4.12}$$

where a_{ji} is the number of simulation events from source j in bin i, P_j and N_j are the strength and total number of events of simulation sample j. N_D represents the total number of events in the data sample. N_D and N_j are given by equations 4.13 and 4.14 respectively.

$$N_D = \sum_{i=1}^{n} d_i \tag{4.13}$$

$$N_j = \sum_{i=1}^{n} a_{ji} \tag{4.14}$$

It is convenient to combine the normalisation factor relating the total size of each simulation sample (N_j) with respect to the data sample size (N_D) with the simulation sample strengths (P_j) into a single number p_j:

$$p_j = \frac{N_D P_j}{N_j}. \tag{4.15}$$

Equation 4.12 then becomes:

$$f_i = \sum_{j=1}^{m} p_j a_{ji}. \tag{4.16}$$

Assuming the number of data events in each bin follows a Poisson distribution, the probability of finding a particular d_i given a particular f_i is given by:

$$P(d_i) = e^{-f_i} \frac{f_i^{d_i}}{d_i!}. \tag{4.17}$$

To estimate the values p_j, one maximises the likelihood L, which is the product of $P(d_i)$ for each of the n histogram bins:

$$L = \prod_{i=1}^{n} P(d_i) = \prod_{i=1}^{n} e^{-f_i} \frac{f_i^{d_i}}{d_i!}. \tag{4.18}$$

For convenience, one can equivalently maximise the log of the likelihood using the relation

$$a^b = e^{b \ln a}, \tag{4.19}$$

to rewrite 4.18 as

$$\ln L = \sum_{i=1}^{n} d_i \ln f_i - f_i. \tag{4.20}$$

This is the technique often referred to as a "binned maximum likelihood". The approach correctly accounts for statistical fluctuation in the number of data events, but it does not consider the fact that the number of Monte Carlo bin entries can also be subject to Poisson statistics. Accommodating this fact, one writes a new expression for the predicted number of events in bin i,

$$f_i = \sum_{j=1}^{m} p_j A_{ji}, \tag{4.21}$$

where A_{ji} is the actual expected (unknown) number of events, with

$$P(a_{ji}) = e^{-A_{ji}} \frac{A_{ji}^{a_{ji}}}{a_{ji}!}. \tag{4.22}$$

One can now write the new log likelihood to be maximised, which incorporates the Poisson nature of the data and Monte Carlo events:

$$\ln L = \sum_{i=1}^{n} d_i \ln f_i - f_i + \sum_{i=1}^{n}\sum_{j=1}^{m} a_{ji} \ln A_{ji} - A_{ji}. \tag{4.23}$$

By maximising 4.23, one obtains estimates for parameters, p_j and A_{ji}, with p_j being the parameter of interest. The construction of the log likelihood and the maximisation strategy have been conveniently implemented in the class TFractionFitter [39], part of the ROOT analysis framework developed at CERN [40].

4.2.2 Choice of fit variables

For the fitting technique above to be effective, the distribution of variables used to construct the likelihood must differentiate the different samples sufficiently, so that a unique set of parameter values give the optimum solution. For example, if the fitting variable chosen had the same shape for all of the samples, any of combination of sample strengths would result in a good description of the data.

Given the selection outlined in section 4.1, the dominant modes which will enter the fit sample are $K_{2\pi}$, $K_{\mu 3}$, K_{e3}, and $K_{3\pi^0}$, with a significantly lower contribution from $K_{3\pi}$. Two variables which are expected to provide enough separation between the samples are the two-body and three-body missing-masses, denoted as $m^2_{miss}(l)$ and $m^2_{miss}(l+\pi^0)$ respectively. The two-body missing-mass here is:

$$m^2_{miss}(l) = (P_K - P_l)^2, \tag{4.24}$$

where P_l is the four momentum of the charged track constructed with either the π^+, μ^+, or e^+ mass and momentum information from the STRAW. The four momentum of the kaon, P_K, can either come from the matched GTK candidate or the nominal kaon described in section 4.1.4.3. The three-body missing-mass uses the information from the tagged π^0, and it is defined as:

$$m^2_{miss}(l+\pi^0) = (P_K - P_l - P_{\pi^0})^2, \tag{4.25}$$

$K_{2\pi}$ is a two-body decay, which means that it peaks in both the two-body and three-body missing-mass distributions, if the π^+ mass is used to construct the two quantities. The two-body missing-mass peaks at $m^2_{\pi^0} = 0.01822$ GeV^2/c^4, and the three-body instance peaks at ≈ 0 GeV^2/c^4 (neutrino mass squared).

The two semileptonic decays, $K_{\mu 3}$ and K_{e3}, both have similar flat shapes in $m^2_{miss}(l)$, due to the missing π^0 and neutrino. However they peak at ≈ 0 MeV/c^2 in their respective "correct" mass hypothesis threebody missing-mass distributions, i.e. $m^2_{miss}(\mu + \pi^0)$ for $K_{\mu 3}$ and $m^2_{miss}(e + \pi^0)$ for K_{e3}.

Similarly to $K_{\mu 3}$ and K_{e3}, $K_{3\pi^0}$ also has continuous spectrum in the two-body missing-mass distribution, due to the fact that it is also a three-body decay. In the three-body missing-mass, under a π^+ hypothesis, it peaks at m_{π^0}, since the missing particle is a second neutral pion, rather than a nearly massless neutrino.

$K_{3\pi}$ decays do not peak in any of the six possible missing-mass configurations, since only one of three pions is used in the two-body versions, and the three-body missing-mass distributions include a mis-reconstructed π^0 or a π^0 from a different decay. It also possible for $K_{\mu 2}$ decays to enter the fit sample, if the muon track is erroneously matched to a π^0. Such decays would peak at zero in the two-body missing-mass distribution, $m^2_{miss}(\mu+)$, but not in any of three-body missing-masses spectra.

The combination of $m^2_{miss}(\pi)$ with one of the three-body missing-mass instances, or two of the three-body missing-masses plotted against one another should provide enough discriminating power to obtain reliable estimates of the sample strengths. Using different combinations of the mass hypothesis for the fit will serve as a useful cross-check, and could be used to obtain an estimate of the systematic uncertainty.

4.2.3 Use of GTK

Calculating the two and three-body missing-masses using the GTK results in a better missing-mass resolution due to the knowledge of the kinematic properties of the incoming kaon. This is turn means that the missing-mass peaks described in the previous section will be narrower, leading to better separation amongst the peaks of the different decay

modes, and potentially better fit performance. The missing-mass distributions obtained with the GTK are sensitive to pileup effects, where the downstream track could be matched to the wrong kaon, or the GTK track could be mis-reconstructed. Therefore, for a good data/simulation agreement to be achieved, pileup effects present in data must be reproduced in simulation.

Including the GTK in the analysis also means the effect of differences between the beam tuning in data, and simulation, are greatly diminished, since that information is present in the reconstructed GTK candidates. If a nominal kaon is used for the upstream-downstream track matching, the missing-mass distributions become sensitive to the direction and momentum of the beam. The beam in data, i.e. the mean and spread of its momentum, dx/dz and dy/dz slopes, does have some considerable differences when compared to simulation. To account for this, a correction scheme needs to be applied to Monte Carlo events. The correction consists of weighting the Monte Carlo events based on the true kaon momentum.

The agreement between data and simulation for the two and three-body missing-masses, with and without the GTK, is discussed in the following chapter. Chapter 5 also reviews the different techniques developed to improve data/simulation agreement including the kaon weighting scheme, and the smearing of upstream and downstream simulation tracks.

Chapter 5

Data and simulation samples

The analysis strategy outlined in the previous chapter relies on simulation for two main functions: a description of the shape of the fit variables, and the calculation of the acceptance for each decay mode included in the fit. If the simulation is to be used for these purposes, good agreement between data and simulation must be demonstrated, particularly in the variables to be fitted, i.e. the two-body and three-body missing-masses squared, calculated with and without the Gigatracker.

Previous comparisons between data and simulation have shown that there are disagreements in the NA62 simulation related to the resolution of the kinematic variable $m^2_{miss}(l)$ ($\sigma^{GTK}_{m^2_{miss}(l)}$), calculated using the GTK. The missing-mass resolution observed in simulation is better than that in data. This results in a difference in the width of the $m^2_{miss}(\pi^+)$ peak of $K_{2\pi}$ decays, particularly in the central part of the peak. There are also known issues regarding the simulation of pileup. Pileup decays also affect the $m^2_{miss}(l)$ and $m^2_{miss}(l+\pi^0)$ distributions, where a charged track could be matched to the "wrong" kaon. Pileup effects can also cause either the track or the kaon to be mis-reconstructed. Such types of events broaden the missing-mass distribution but dominate in the tails of the distributions.

A mechanism to inject pileup hits into Monte Carlo events has been developed by the NA62 collaboration, and this significantly improves the data/simulation agreement in the tails of the missing-mass distributions. There are however residual discrepancies

in the agreement at the level of around 30%. In order to improve the data/simulation agreement of the missing-mass resolution (with GTK), techniques to smear STRAW and GTK tracks were developed. Applying the smearing to simulation events brings the agreement with data to ¡5% in the central part of the $m^2_{miss}(\pi)$ spectrum. The fraction sample fit works well when the fit distributions in simulation are representative of the ones in data. Applying corrections such as the kinematic smearing serve to improve the data/simulation agreement to this effect.

Matching downstream tracks to a "nominal" kaon, with constant properties for each event removes the bulk of the influence of the pileup effects. However the $m^2_{miss}(l)$ and $m^2_{miss}(l+\pi^0)$ distributions become sensitive to differences between the beam properties in data and simulation, which are significant. To mitigate this effect, Monte Carlo events are weighted according to the true kaon momentum and the data/simulation ratio of beam parameters as measured by the GTK.

An overview of the data and simulation samples used for data/simulation agreement studies, and subsequent K_{l3} branching fraction measurement, is given in sections 5.1 and 5.2 respectively. Section 5.3 discusses the data/MC agreement when using the Gigatracker, including the smearing techniques for STRAW and GTK track (section 5.3.1) and pileup (section 5.2.1). The "nominal" kaon strategy and the requisite weighting and corrections are discussed in 5.4.

5.1 Data samples

The analysis presented in this thesis is based on a data sample collected between September and November 2016, designated as 2016A. This is the first data sample available where all three stations of the Gigatracker were fully commissioned [41]. The sample is composed of 122 runs, with each run consisting of a few hundred to a thousand SPS spills or bursts, for a total of around 84 000 bursts. The beam intensity during the collection of 2016A was approximately 40% of the nominal one. Figure 5.1 shows the instantaneous intensity for the data sample, where the mean is around 280 MHz. The total number of control triggers analysed is around 8.3×10^8.

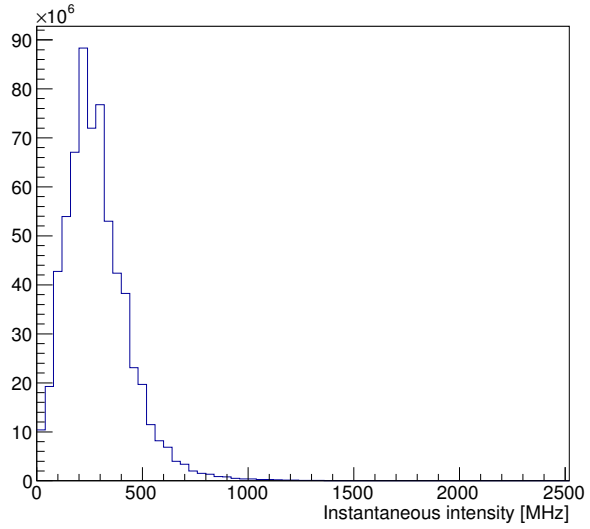

Figure 5.1: The instantaneous beam intensity (λ) for 2016A.

5.2 Simulation samples

The simulation of the secondary hadron beam is carried out by the ray tracing package TURTLE [42]. The software simulates the transport of a K^+ through the beam optics described in section 2.1 up to the entrance of the CEDAR, which is at $z \approx 70$ m. The rest of the simulation is handled by GEANT4 [43], which deals with the decay of particles and their physical interactions with the NA62 detector. Dedicated decay generator libraries are used to reproduce the decay properties of the different kaon decay modes [44].

The output of the decay generators, i.e. the daughter particles of the K^+, is taken by GEANT4, which then handles the simulation of the particles' passage through the experiment and their interactions with the detector material using Monte Carlo (MC) methods. Detector geometries, materials and magnetic fields are all represented in GEANT4.

The output of the above processes then goes through a digitisation step which attempts to simulate the properties of the read out electronics of the detectors, e.g. time resolution of photo-multipliers. The output of this phase is then fed into exactly the same NA62Reconstruction software [45] as that used to process the data.

In the NA62 Monte Carlo generation setup described thus far, only one kaon decay is simulated per event meaning that pile-up effects which may be present in data are not intrinsically reproduced. In order to introduce pile-up processes in the simulation, detector hits are injected into the simulation events at the analysis level. The mechanism of injection is described in section 5.2.1.

5.2.1 Pileup simulation

The pileup generation process starts by determining the expected number of pileup particles for each simulation event. For 2016A, the mean beam intensity is around 280 MHz. Using this value, the expected number of pile-up events within a 150 ns time window is calculated. This number is then used as a rate parameter in a Poissonian distribution from which the number of particles to be injected into the event is extracted. The identity of each generated beam particle is assigned according to the beam composition at the third GTK station, i.e. 6.0% koans, 70.2% pions, and the rest protons. The time of the beam pileup particle is uniformly assigned to be between $\pm$75 ns.

For each generated pileup particle, hits (also obtained from simulation) are added to the detector events of the KTAG, GTK, STRAW, CHOD, MUV3, and LKr. For the two upstream detectors (KTAG and GTK), the properties of the generated pileup particles can be used directly. For the downstream detectors, this is not the case as the decay of the pileup particles also needs to be accounted for.

The number of hits added to the CEDAR events depends on the pileup particle type being simulated. For a pileup K^+, the number of hits introduced is taken from a Poission distribution, with a mean rate of 18 (the average number of KTAG hits per kaon). For a pileup pion, the average hit rate is 0.6. No hits are injected in the KTAG for pileup protons, as the detector is completely blind to them. Each hit is assigned to one of the eight sectors at random. The time of each hit is taken from the time of the generated pileup particle with the application of smearing according to the time resolution of the KTAG PMs.

For the GTK, a hit library is used, where each entry contains a varying number of channel IDs to be assigned to the pileup hits. For every pileup particle, an entry from the library is picked at random. The time assigned to this is that of the generated pileup particle with additional smearing corresponding to the individual pixel time resolution. The GTK pileup simulation also includes the introduction of a 4% hit inefficiency.

To include the effects of pileup downstream of the GTK, two extra processes need to be simulated:

- whether the pileup particle decays inside the experiment's fiducial volume
- the decay mode of the pileup particle.

The probability for a K^+ to decay within the NA62 fiducial volume ($102 < z < 180$ m) is 12.9%. The K^+ decay probability goes up to 25%, if the decay region is extended to include the end part of the experiment ($102 < z < 265$ m). The fraction of pions which decay in the range, $102 < z < 265$ m, is around 3%. Hits from the decay products of pileup kaons and pions are injected into the simulation event according to these two probabilities.

Pileup kaons can decay to one of the main six K^+ decay modes, which add up to 99.995% of the total K^+ decay rate. The frequency of each decay process is determined according to the decay branching fractions, summarised in table 1.2. Each decay mode has a library of simulated hits deposited in the STRAW, CHOD, LKr, and MUV3 detectors by the daughter particles of the corresponding decay. The hits from these libraries are injected into the corresponding detector events, with the time of the hits coming from the time of the parent pileup particle and the individual time of the simulated hit.

For pileup π^+s, a library containing hits from simulated $\pi^+ \to \mu^+\nu_\mu$ decays (branching fraction $\approx 99.99\%$) is used to add inject pileup information into detector events. There are no downstream pileup hits added from generated pileup protons.

The secondary hadron beam of NA62 is accompanied by a beam "halo", mainly composed of muons originating from charged pions decaying along the beamline. The rate

of the halo has been estimated to be 136 MHz at nominal beam intensity. This number is scaled according to the actual beam intensity for 2016A, and is used to calculate the number of halo particles to insert into the simulation event. The same Poissonian statistics process as the generation of the number of beam pileup particles is used. A library of simulated halo muon hits is used to inject the extra activity into the downstream detectors.

5.3 Agreement with GTK kaons

5.3.1 Kinematic resolution

The decay $K^+ \to \pi^+\pi^0$ is useful to study $\sigma_{m^2_{miss}}$ as it is a two-body decay, therefore $m^2_{miss}(l)$ peaks at $m^2_{\pi^0} = 0.01822$ GeV^2/c^4. The decay is also particularly pertinent as it is the dominant contribution to the data sample selected for the fraction fit. To select a nearly pure control sample of $K_{2\pi}$ events for the purposes of studying the data/simulation agreement, the fit sample selection described in 4.1 was extended, by adding π^+ identification, photon veto, and kinematic cuts. The additional cuts applied are summarised below:

- $0.000 < m^2_{miss}(\pi^+) < 0.036$ [GeV^2/c^4]
- $-0.001 < m^2_{miss}(\pi^+ + \pi^0) < 0.001$ [GeV^2/c^4]
- $E^{LKr}_{track}/P^{STRAW}_{track} < 0.8$
- No MUV3 candidate within 5 ns of T_{KTAG}
- No extra LKr clusters within 4 ns of T_{KTAG}
- No LAV candidate within 4 ns of T_{KTAG}
- No IRC or SAC candidates within 7 ns of T_{KTAG}.

The first two criteria exploit the two-body kinematics of the $K_{2\pi}$ decay, i.e. the peak at 0.01822 GeV^2/c^4 for the two-body missing-mass distribution, and 0 GeV^2/c^4 for three-body variant. The $E^{LKr}_{track}/P^{STRAW}_{track}$ cut is designed to reject events where the charged

track is an electron, e.g. K_{e3}. Electrons deposit all of their energy into the LKr, giving $E^{LKr}_{track}/P^{STRAW}_{track} \approx 1$. The MUV3 veto rejects events with muons in them, e.g. $K_{\mu 3}$ and $K_{\mu 2}$. The last three conditions reject events with additional photons to the two used to reconstruct the neutral pion. Such events normally contain radiative and $K_{3\pi^0}$ decays.

In order to improve the overall data/simulation agreement, and allow closer comparison, the pileup simulation described in section 5.2.1 was used. The effect of pileup injection on the $m^2_{miss}(\pi^+)$ and CDA distributions for $K_{2\pi}$ selected events is illustrated by figures 5.2 and 5.3 respectively, where the improvement is clearly visible. The disagreement in the centre of the missing-mass and CDA distributions is mitigated by a set of smearing techniques outlined in this section.

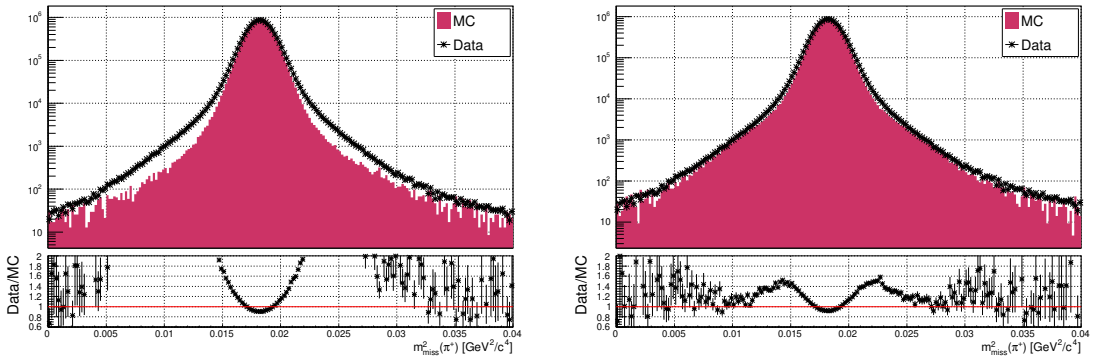

(a) $m^2_{miss}(\pi^+)$ before pileup injection

(b) $m^2_{miss}(\pi^+)$ after pileup injection

Figure 5.2: Data/simulation comparison of the $m^2_{miss}(\pi^+)$ distribution for $K_{2\pi}$ selected events before (left) and after (right) pileup injection.

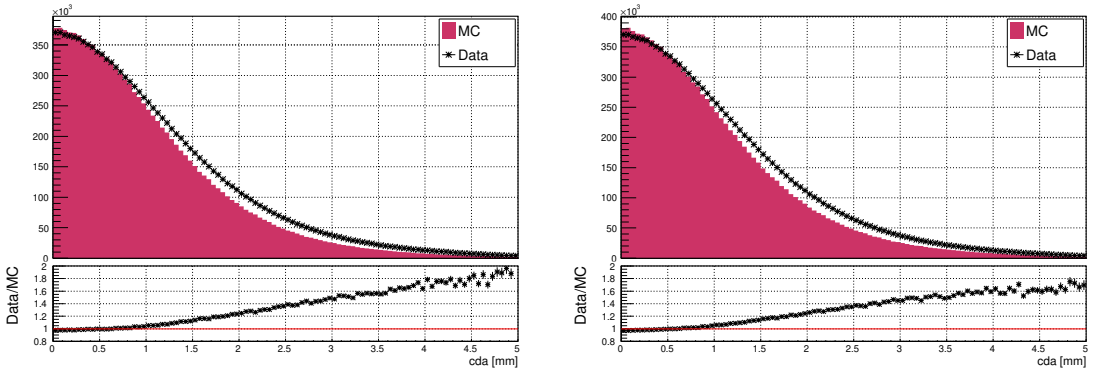

(a) CDA before pileup injection

(b) CDA after pileup injection

Figure 5.3: Data/simulation comparison of the CDA distribution for $K_{2\pi}$ selected events before (left) and after (right) pileup injection.

The "central" parts of the $m^2_{miss}(\pi^+)$ and CDA distributions are dominated by the intrinsic resolutions of the GTK and STRAW detectors. The $m^2_{miss}(\pi^+)$ resolution is dependent on both of the resolution of the tracks momentum and direction, whereas the CDA is only influenced by resolution of the track direction. The individual contributions of the different measured quantities to the missing-mass squared resolution is shown in figure 5.4.

The resolution of $m^2_{miss}(\pi^+)$ appears to be better in simulation when compared to data, leading to a narrower missing-mass peak in simulation, resulting in the parabola observed in the data/simulation ratio between 0.016 GeV$^2/c^4 < m^2_{miss}(\pi^+) <$ 0.02 GeV^2/c^4 in figure 5.2. A similar effect is seen in the data/simulation ratio of the CDA distribution between the kaon and its charged daughter particle, figure 5.3.

Four different kinematic resolutions enter into the overall resolution of $m^2_{miss}(\pi^+)$. These are the kaon angle and momentum resolutions (GTK), as well as the daughter charged track direction and momentum resolutions (STRAW), the four quantities are denoted as σ_{θ_K}, σ_{P_K}, σ_{θ_π}, σ_{P_π} respectively. In order to study which one or more of these quantities is causing the disagreement observed in figures 5.2 and 5.5, one can calculate and plot the contribution of each of the four kinematic resolution to $\sigma_{m^2_{miss}}$ as a function of P_π. To do so, one starts from the expression for $m^2_{miss}(\pi^+)$, given in equation 5.1 below,

$$m^2_{miss} \approx m^2_K \left(1 - \frac{|P_\pi|}{|P_K|}\right) + m^2_\pi \left(1 - \frac{|P_K|}{|P_\pi|}\right) - |P_K|\,|P_\pi|\,\theta^2_{K\pi}, \tag{5.1}$$

where m_K and m_π are the masses of K^+ and π^+ respectively, P_K and P_π are their momenta, and $\theta_{K\pi}$ is the angle between them. Equation 5.1 is partially differentiated with respect to each of variable of interest, i.e. P_K, P_π, $\theta_{K\pi}$, and multiplied by the resolution of each variable, which may be a function of P_π. The parametrisations of each resolution function are given in equations 5.2, 5.3, 5.4, and 5.5. The four resulting $\sigma_{m^2_{miss}}$ contributions curves, and their sum in quadrature are plotted in figure 5.4.

$$\sigma_{\theta_K} = 15\ \mu rad \tag{5.2}$$

$$\frac{\sigma_{P_K}}{P_K} = 0.2\% \tag{5.3}$$

$$\sigma_{\theta_\pi} = 14\ \mu rad \oplus \frac{600\ \mu rad}{P_\pi[\mathrm{GeV/c}]} \tag{5.4}$$

$$\frac{\sigma_{P_\pi}}{P_\pi} = 0.3\% \oplus 0.005\% \cdot P_\pi \tag{5.5}$$

The ratio between the $m^2_{miss}(\pi^+)$ and CDA resolutions in data and simulation is plotted as a function of the π^+ momentum in figure 5.5. These plots show that the resolution in data is around 10% to 15% higher compared to data, and that disagreement does not change significantly as a function of track momentum. The flat distributions of figure 5.5 do not definitively indicate whether the STRAW or the GTK is causing the discrepancies seen between data and simulation for the $\sigma_{m^2_{miss}}$ and σ_{CDA} distributions.

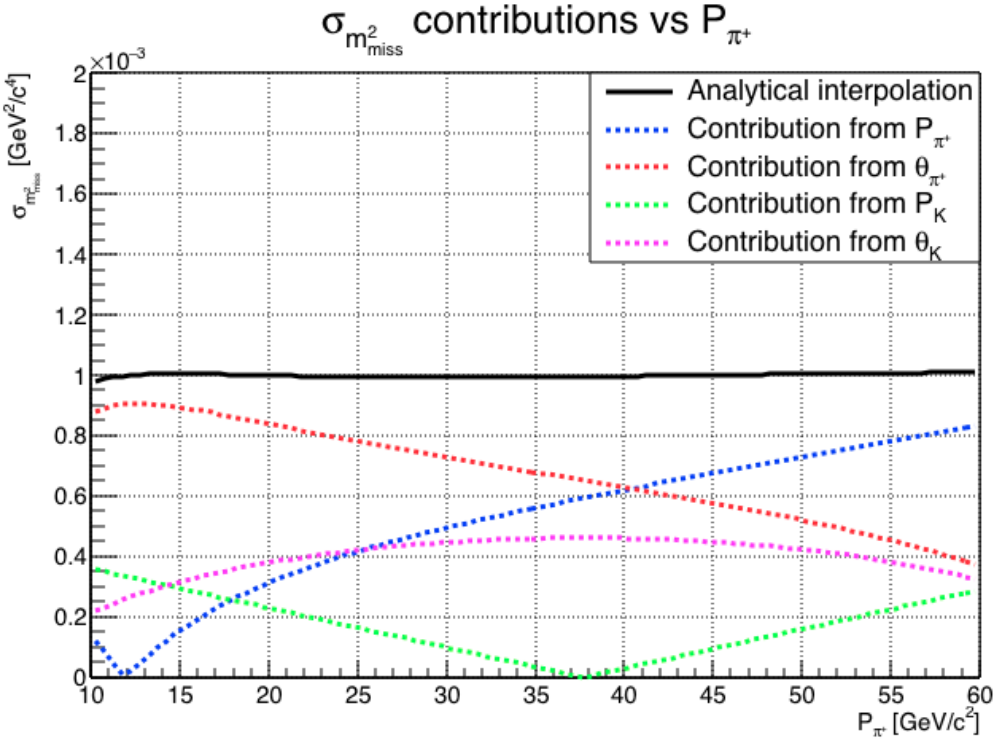

Figure 5.4: The contributions of the kaon and pion directions and momenta resulting in the overall missing-mass resolution.

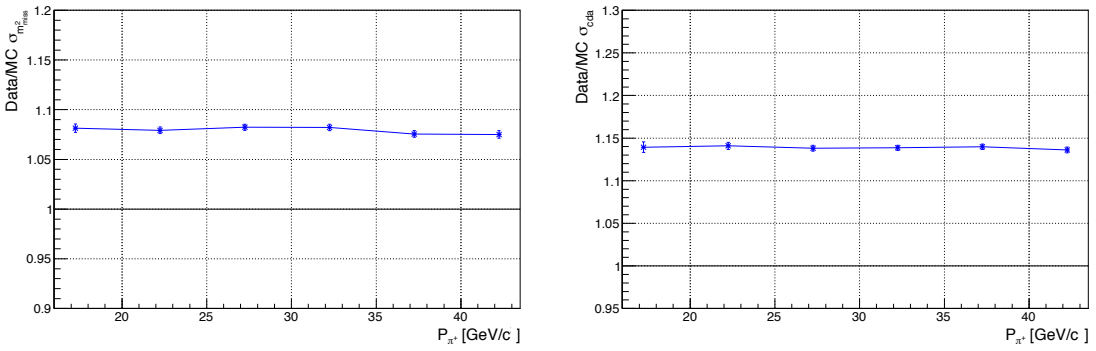

(a) $\sigma_{m^2_{miss}}$ vs. P_{π^+} (b) σ_{CDA} vs. P_{π^+}

Figure 5.5: Data/simulation ratio of the m^2_{miss} (left) and CDA (right) resolutions as a function of the track momentum P_{π^+} for $K_{2\pi}$ events.

To clarify the picture, one can isolate the effect of the downstream track spectrometer using $K^+ \to \pi^+\pi^+\pi^-$ ($K_{3\pi}$) decays, where all three tracks are reconstructed in the STRAW. The sum of the four momenta of the three tracks gives the kaon mass ($m_K = 493.67$ MeV/c^2), where the width of the $K_{3\pi}$ mass ($m_{K_{3\pi}}$) peak can be used to study the resolution of the STRAW tracks' direction and momentum. $K_{3\pi}$ events are selected according to the following criteria:

- Exactly one three track vertex
- Vertex fit $\chi^2 < 25$
- 104 m $< Z_{vertex} <$ 165 m
- Sum of track charges must be +1
- $\left|\left|\sum_{n=1}^{3} P_n\right| - 75\right| < 3$ GeV
- 490 MeV $< m_{K3\pi} <$ 497 MeV
- All three tracks in acceptance of the four STRAW chambers and CHOD
- At least one track spatially matched to a NA48-CHOD candidate
- $T_{K3\pi} - T_{trigger} < 5$ ns.

The first two conditions isolate events with a three charged track vertex, i.e. events with $K_{3\pi}$ decays. The Z_{vertex} cut selects events with decays in the fiducial volume

of the experiment. The next four criteria ensures that three tracks came from the same positive parent particle (a kaon originating from the NA62 beam) by applying charge, momentum, and rest mass conversation. The NA48-CHOD track association requirement ensures, that a time can be assigned to the decay, which can be used match the decay with the trigger. This decay time is used to reject events where the $K_{3\pi}$ decay did not cause the trigger to be fired.

The data and simulation distributions of $m_{K_{3\pi}}$ for $K_{3\pi}$ selected events are plotted in figure 5.6. As in $K_{2\pi}$ decays, the invariant mass peak is narrower in simulation, pointing to better kinematic resolution. The presence of this effect in $K_{3\pi}$ events indicates that resolution of the STRAW in the Monte Carlo does not match that in data, and that at least some of the disagreement observed in figure 5.5 is due to the STRAW.

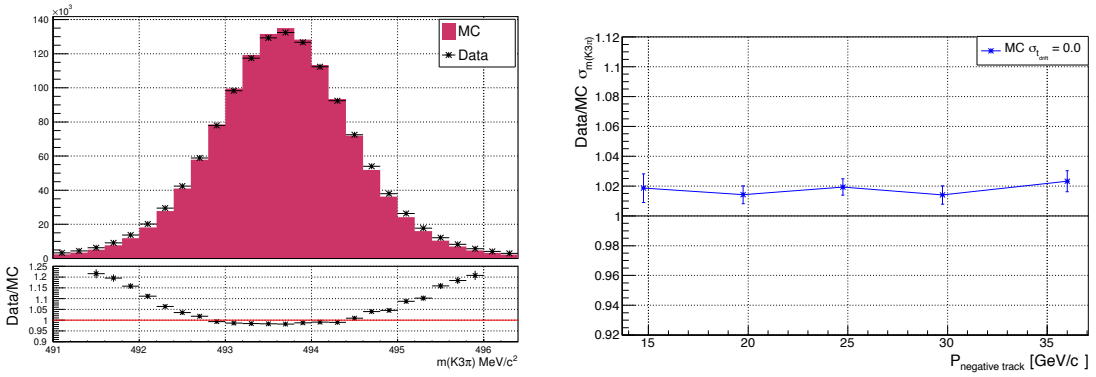

(a) $m_{K3\pi}$ (b) $\sigma_{m_{K_{3\pi}}}$ vs. P_{π^-}

Figure 5.6: Data/simulation comparison of the reconstructed $m_{K_{3\pi}}$ (left), and its resolution as a function of the negative track momentum P_{π^-} (right).

In order improve the agreement between data and simulation, two Gaussian smearing techniques were developed to smear the directions and momenta of STRAW and GTK tracks. The direction and momentum of a reconstructed STRAW track are derived from the spatial positions of the individual hits which constitute the track. The position of a STRAW hit is determined by the distance between the anode wire inside the STRAW tube and the path of the traversing charged particle. This distance is derived from the drift time, t_{drift}, of the ionisation products created by the incident charged particle. The final position of the particle path is calculated by combining the distance from the wire, d_{wire}, with the known position of the STRAW tube. Therefore, by smearing the

measured drift time of the ionisation products inside the straw tube, the direction and momentum of the reconstructed track will also be smeared.

To investigate the effect of the STRAW smearing technique, the t_{drift} of STRAW hits was smeared according to a Gaussian distribution with several different standard deviations ($\sigma_{t_{\text{drift}}}$). The values of $\sigma_{t_{\text{drift}}}$ which were used are 0.5 ns, 1.0 ns, 1.5 ns, 2.0 ns where the typical resolution of the drift time is around 200 ns. Figure 5.7 shows the effect of the t_{drift} smearing on the reconstructed m_K from $K_{3\pi}$ selected events, where the smeared simulation samples are compared with data.

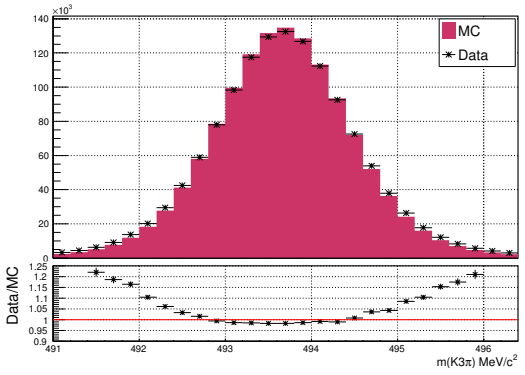

(a) $m_{K3\pi}$, $\sigma_{t_{\text{drift}}} = 0.5$ ns

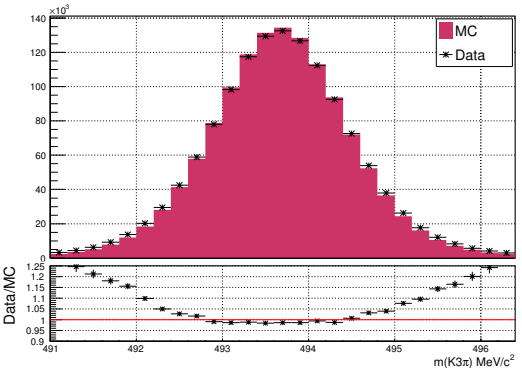

(c) $m_{K3\pi}$, $\sigma_{t_{\text{drift}}} = 1.0$ ns

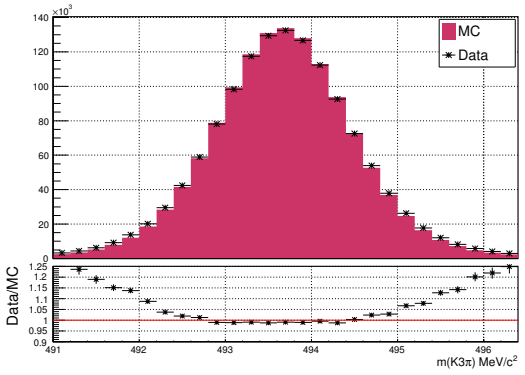

(b) $m_{K3\pi}$ from $K_{3\pi}$ selected events, $\sigma_{t_{\text{drift}}} = 1.5$ ns

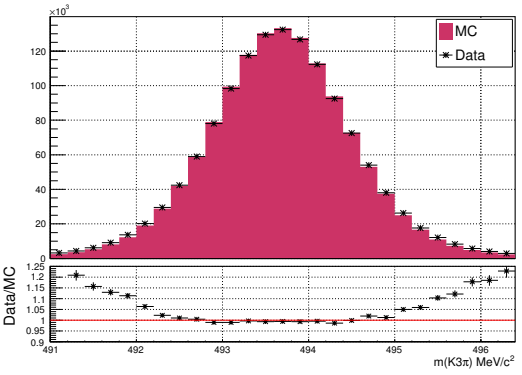

(d) $m_{K3\pi}$, $\sigma_{t_{\text{drift}}} = 2.0$ ns

Figure 5.7: Invariant mass of the three tracks in $K \to \pi^+\pi^-\pi^-$ decays for data and simulation with different t_{drift} smearing.

The data/simulation ratio for the reconstructed kaon mass appears to converge to around 1 for the central region of the invariant mass distribution in figure 5.7d, where $\sigma_{t_{\text{drift}}} = 2.0$. Figure 5.8 also suggests that smearing t_{drift} by 2.0 ns, modifies the STRAW resolution in Monte Carlo, so that it matches the one in data.

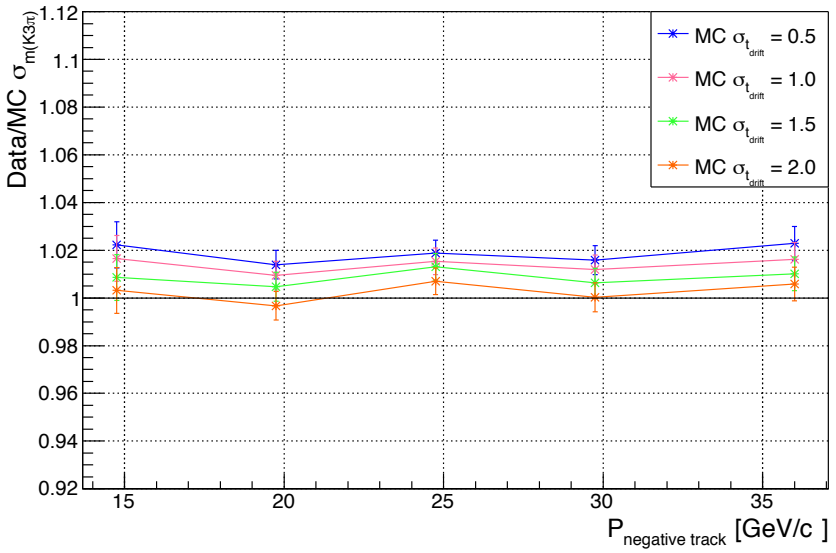

Figure 5.8: Mass resolution of the kaon mass in $K \to \pi^+\pi^-\pi^-$ decays for data and simulation with different $\sigma_{t_{\text{drift}}}$.

The effect of the STRAW smearing on the missing-mass and CDA for $K_{2\pi}$ events can be seen in figures 5.9 and 5.10 respectively. The data/simulation agreement between the two kinematic resolutions is plotted as a function of the π^+ momentum in figure 5.10. Studying these three figures, one can clearly see that while the STRAW smearing does improve the data/simulation ratio, significant differences remain. The fact that the invariant mass resolution in data and simulation matches in $K_{3\pi}$, but not in $K_{2\pi}$ suggests that the residual disagreement comes from the GTK.

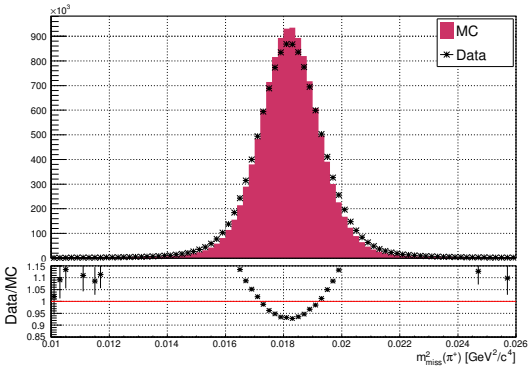

(a) $m^2_{miss}(\pi^+)$, $\sigma_{t_{\text{drift}}} = 0.5$

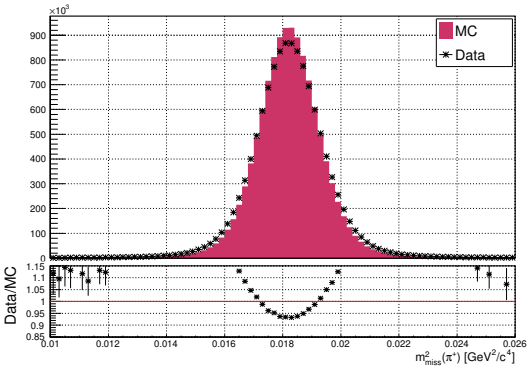

(c) $m^2_{miss}(\pi^+)$, $\sigma_{t_{\text{drift}}} = 1.0$ ns

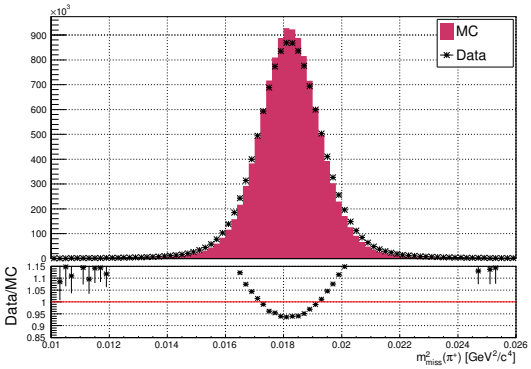

(b) $m^2_{miss}(\pi^+)$, $\sigma_{t_{\text{drift}}} = 1.5$ ns

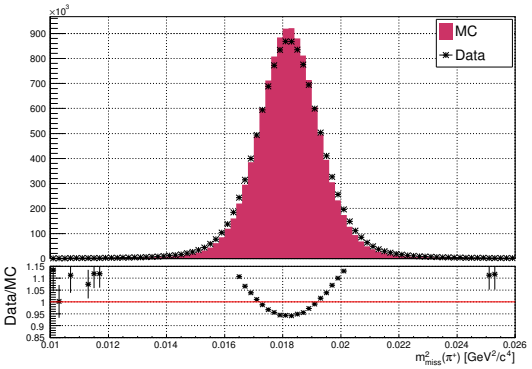

(d) $m^2_{miss}(\pi^+)$, $\sigma_{t_{\text{drift}}} = 2.0$ ns

Figure 5.9: Data/simulation comparison of the $m^2_{miss}(\pi^+)$ for $K \to \pi^+\pi^0$ decays with different values of $\sigma_{t_{\text{drift}}}$.

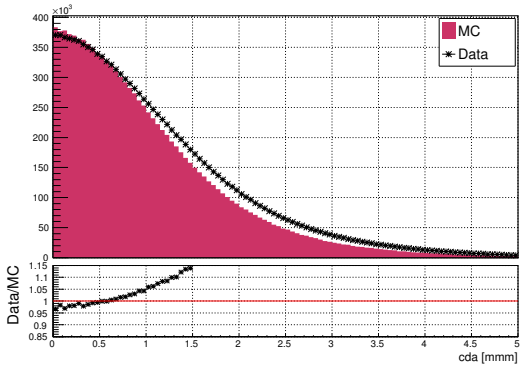

(a) CDA, $\sigma_{t_{\text{drift}}} = 0.5$ ns

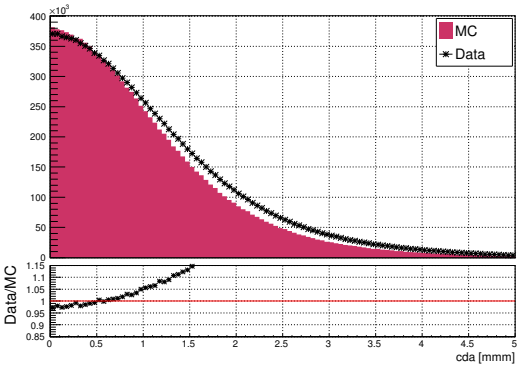

(c) CDA, $\sigma_{t_{\text{drift}}} = 1.0$ ns

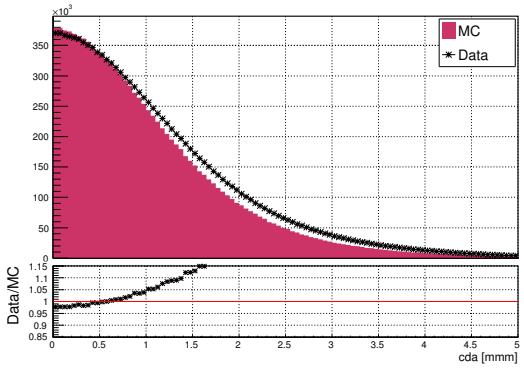

(b) CDA, $\sigma_{t_{\text{drift}}} = 1.5$ ns

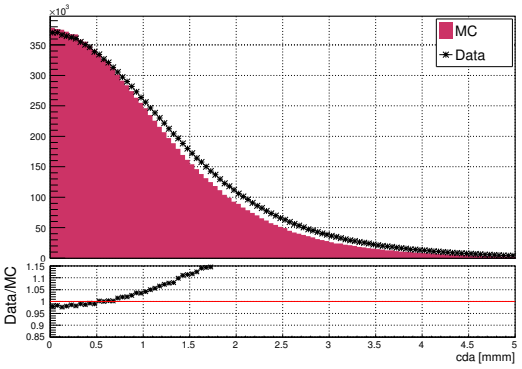

(d) CDA, $\sigma_{t_{\text{drift}}} = 2.0$ ns

Figure 5.10: Data/simulation comparison of the CDA for $K \to \pi^+\pi^0$ decays with different $\sigma_{t_{\text{drift}}}$.

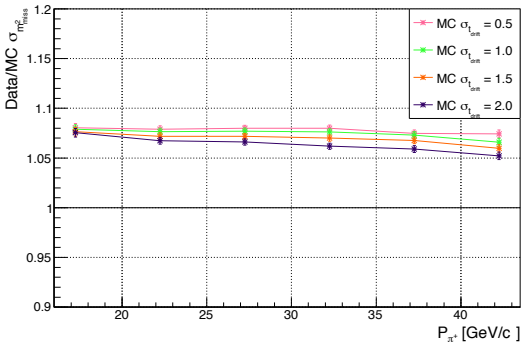

(a) $\sigma_{m^2_{miss}(\pi^+)}$ vs. $P_{\pi+}$

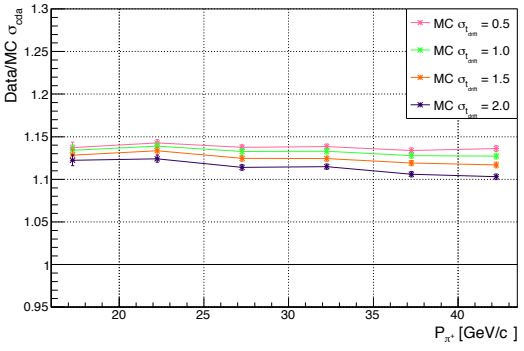

(b) σ_{CDA} vs. $P_{\pi+}$

Figure 5.11: Data/simulation ratio of the missing-mass and CDA resolutions from $K \to \pi^+\pi^0$ decays with different values of $\sigma_{t_{\text{drift}}}$.

To modify the GTK kinematic resolution, a Gaussian smearing was applied to the track direction and momentum separately. The standard deviation of the Gaussian used to smear the track angle was computed using the multiple scattering relation, given in equation 5.6:

$$\sigma_{\theta_{GTK}} = \alpha_{GTK} \cdot \sqrt{\frac{X_{GTK}}{X_0}} \cdot \frac{13.5}{P_{GTK}}, \tag{5.6}$$

where α_{GTK} was the parameter used to tune the amount of smearing added. X_{GTK}/X_0, represents the nominal thickness of the three GTK stations, which is 0.015.

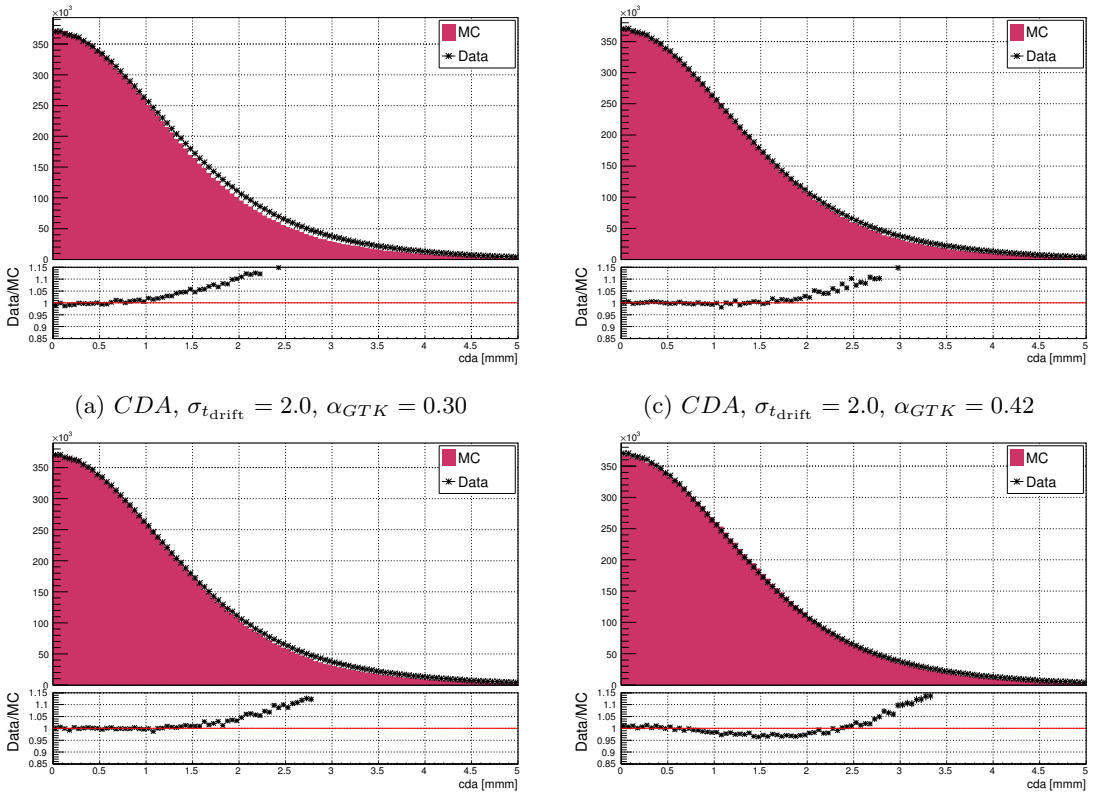

(a) CDA, $\sigma_{t_{\text{drift}}} = 2.0$, $\alpha_{GTK} = 0.30$

(c) CDA, $\sigma_{t_{\text{drift}}} = 2.0$, $\alpha_{GTK} = 0.42$

(b) CDA, $\sigma_{t_{\text{drift}}} = 2.0$, $\alpha_{GTK} = 0.40$

(d) CDA, $\sigma_{t_{\text{drift}}} = 2.0$, $\alpha_{GTK} = 0.50$

Figure 5.12: Data/simulation comparison of CDA for $K \to \pi^+\pi^0$ decays with different values of α_{GTK}.

The initial scan of the GTK slope smearing parameter was done for three values of α_{GTK}: 0.3, 0.4, 0.5. Figure 5.12d shows that a smearing with $\alpha_{GTK} = 0.5$, oversmears the GTK angles, and the CDA resolution in MC becomes significantly worse compared to data. However, figure 5.12b and the green curve in figure 5.14b, where $\alpha_{GTK} = 0.4$, suggest that the CDA agreement could be further improved by a small increase in α_{GTK}.

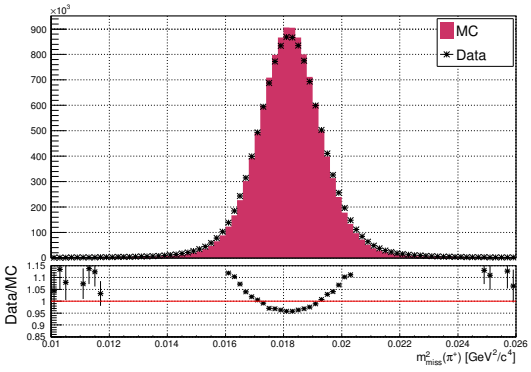

(a) $m^2_{miss}(\pi^+)$, $\sigma_{t_{\text{drift}}} = 2.0$, $\alpha_{GTK} = 0.30$

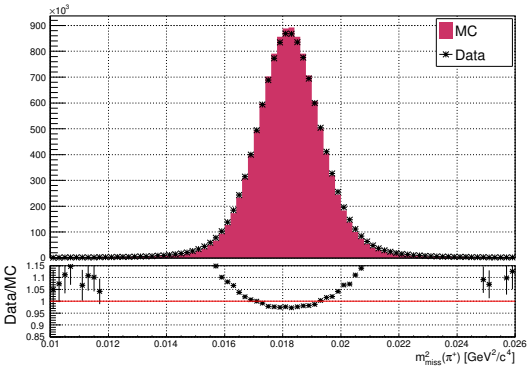

(c) $m^2_{miss}(\pi^+)$, $\sigma_{t_{\text{drift}}} = 2.0$, $\alpha_{GTK} = 0.42$

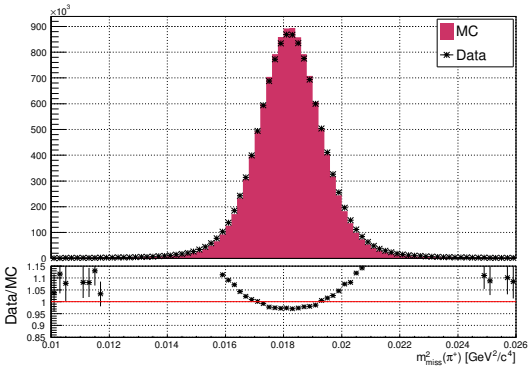

(b) $m^2_{miss}(\pi^+)$, $\sigma_{t_{\text{drift}}} = 2.0$, $\alpha_{GTK} = 0.40$

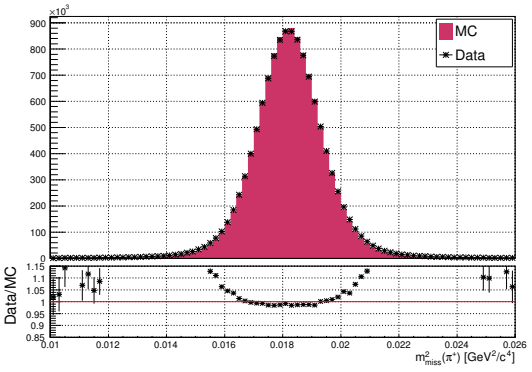

(d) $m^2_{miss}(\pi^+)$, $\sigma_{t_{\text{drift}}} = 2.0$, $\alpha_{GTK} = 0.50$

Figure 5.13: Data/simulation comparison of the $m^2_{miss}(\pi^+)$ for $K \to \pi^+\pi^0$ decays with different values of α_{GTK}.

A second narrower scan in α_{GTK} found that a value of 0.42 extends the region where the data/simulation ratio of σ_{CDA} is 1 to beyond 1.5 mm, figure 5.12c.

As it can be seen from figures 5.13c and 5.14, the angular smearing which gives the best CDA agreement, significantly improves the $m^2_{miss}(\pi^+)$ agreement, however $\sigma_{m^2_{miss}}$ remains around 4% better in simulation than in data. The residual discrepancy can be attributed to the mismatch between the GTK momentum resolution in data and simulation. In order to resolve this difference, the GTK track momentum is smeared according a Gaussian distribution with a standard deviation of $\sigma_{P_{GTK}}$ given by equation 5.7:

$$\sigma_{P_{GTK}} = \beta_{GTK} \cdot P_{GTK}, \tag{5.7}$$

where β_{GTK} is the smearing parameter to be tuned.

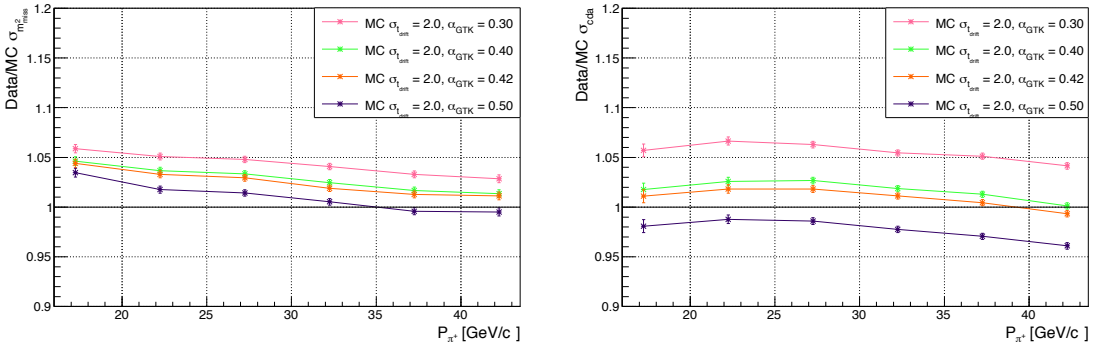

(a) $\sigma_{m^2_{miss}(\pi^+)}$ vs. P_{π^+} (b) σ_{CDA} vs. P_{π^+}

Figure 5.14: Data/simulation ratio of the $m^2_{miss}(\pi^+)$ and CDA resolutions for $K_{2\pi}$ decays as a function of the STRAW track momentum P_{π^+} with different values of α_{GTK}.

An initial scan of β_{GTK} was performed, where three parameter values were tried: 0.001, 0.002, and 0.003. The resulting distributions of $m^2_{miss}(\pi^+)$ from the scan are shown in figure 5.15, with the data/simulation agreement plotted as a function of P_{π^+} in figure 5.16.

According to figure 5.15d, a value of 0.003 for β_{GTK} appears to add too much smearing, whereas 0.002 is not enough. Following this observation, the GTK smearing was repeated with $\beta_{GTK} = 0.0025$, which brings the overall data/MC agreement of two-body missing-mass to within $\mathcal{O}(1\%)$.

Figures 5.14b and 5.16 show that, while $\alpha_{GTK} = 0.42$ and $\beta_{GTK} = 0.0025$ give good overall agreement for the CDA and $m^2_{miss}(\pi^+)$ distributions, $\mathcal{O}(3\%)$ discrepancies, as a function of the track momentum, do remain. These differences can be attributed to shortcomings in the independent smearing of the GTK tracks' direction and momentum.

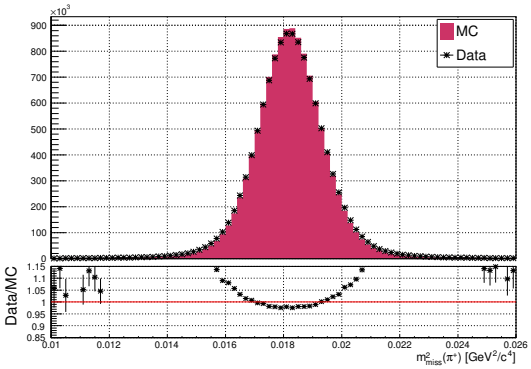

(a) $m^2_{miss}(\pi^+)$, $\sigma_{t_{\text{drift}}} = 2.0$, $\alpha_{GTK} = 0.42$, $\beta_{GTK} = 0.001$

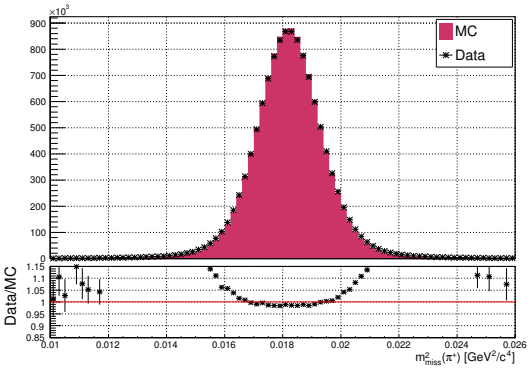

(c) $m^2_{miss}(\pi^+)$, $\sigma_{t_{\text{drift}}} = 2.0$, $\alpha_{GTK} = 0.42$, $\beta_{GTK} = 0.002$

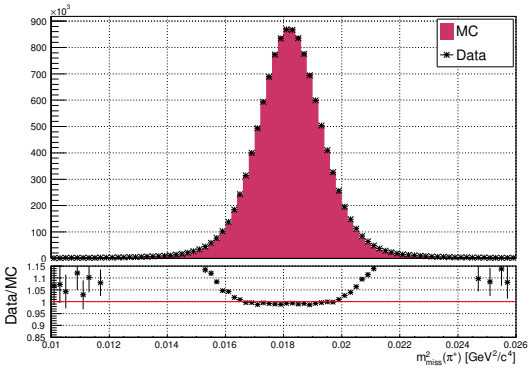

(b) $m^2_{miss}(\pi^+)$, $\sigma_{t_{\text{drift}}} = 2.0$, $\alpha_{GTK} = 0.42$, $\beta_{GTK} = 0.0025$

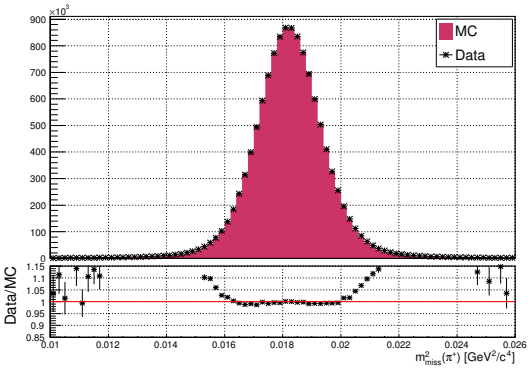

(d) $m^2_{miss}(\pi^+)$, $\sigma_{t_{\text{drift}}} = 2.0$, $\alpha_{GTK} = 0.42$, $\beta_{GTK} = 0.003$

Figure 5.15: Data/simulation comparison of $m^2_{miss}(\pi^+)$ for $K \to \pi^+\pi^0$ decays with different values of β_{GTK}.

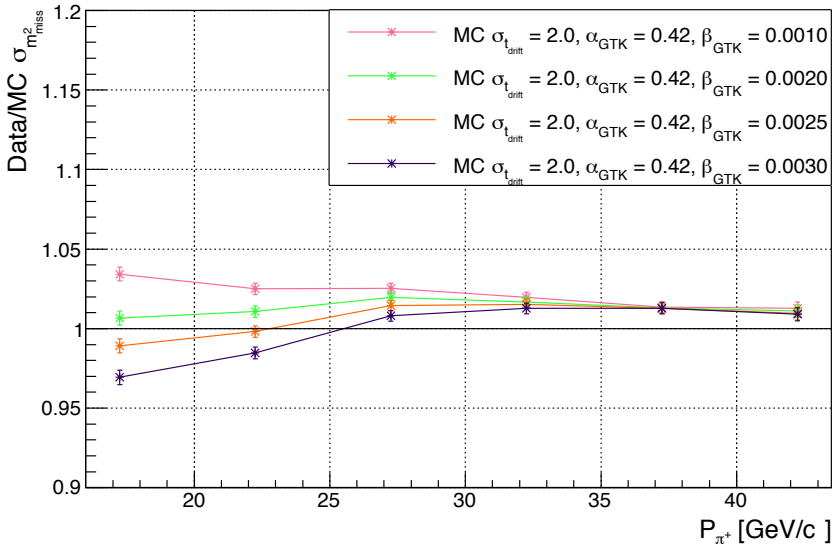

Figure 5.16: Data/simulation ratio of the $m^2_{miss}(\pi^+)$ resolution for $K_{2\pi}$ decays with different values of β_{GTK}.

5.3.2 Pileup

As it can be seen from figure 5.2, adding pileup decays to the simulation significantly improves data/MC agreement. There are however residual "shoulders" which remain in the data/simulation ratio for $m^2_{miss}(\pi)$. Pileup decays also affect the three-body missing-mass distribution, $m^2_{miss}(\pi^+ + \pi^0)$. Figure 5.17 shows the three-body missing-mass for $K_{2\pi}$ decays, with and without pileup injection. The $K_{2\pi}$ selection used for figure 5.17 builds on the fit sample selection, and applies the following cuts:

- $0.000 < m^2_{miss}(\pi^+) < 0.036$ [GeV^2/c^4]
- $E^{LKr}_{track}/P^{STRAW}_{track} < 0.8$
- No MUV3 candidate within 5 ns of T_{KTAG}

Here, fewer cuts are applied compared to the $K_{2\pi}$ selection criteria in section 5.3.1. This allows the control sample selected with the above conditions to be more representative of the eventual fit sample, which is obtained with the criteria described in section 4.1.

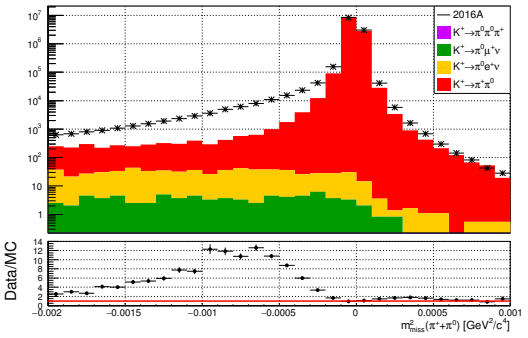

(a) $m^2_{miss}(\pi^+ + \pi^0)$, no pileup

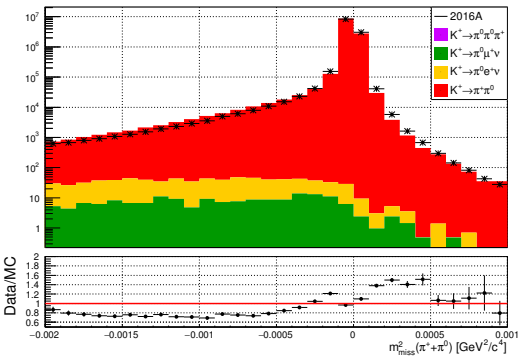

(b) $m^2_{miss}(\pi^+ + \pi^0)$, with pileup

Figure 5.17: Data/simulation comparison of $m^2_{miss}(\pi^+ + \pi^0)$ for $K \to \pi^+\pi^0$ decays without (left) and with (right) pileup injection.

From figure 5.17a it can be seen that there is a clear deficit of Monte Carlo events if there are no pileup particles added. By injecting pileup decays into the simulation, figure 5.17b, the agreement of data with simulation improves significantly, however an excess of simulation events means that the agreement is at level of around 30%.

5.3.3 m_{π^0}

Another effect which contributes to the disagreement in figure 5.17 is the reconstruction of the neutral pion. Figure 5.18 shows the data/simulation agreement of the reconstructed m_{π^0} for $K_{2\pi}$ decays. The mass of the neutral pion is around 1 MeV/c^2 lower in data than Monte Carlo. This causes the $m^2_{miss}(l + \pi^0)$ peak to be offset between data and simulation, with the simulation peak being offset in the negative missing-mass direction.

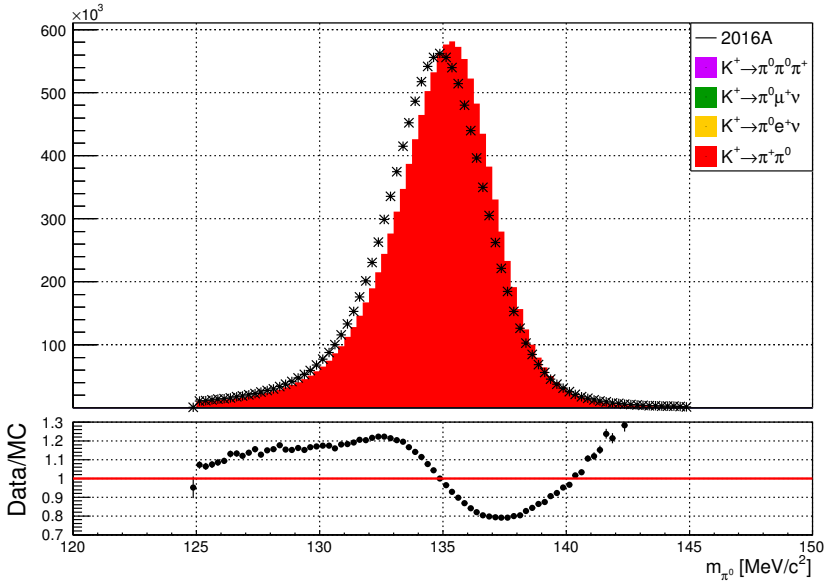

Figure 5.18: Data/simulation comparison of the reconstructed m_{π^0} from $K_{2\pi}$ decays.

Figure 5.19 shows the mean m_{π^0} for the 122 runs used for the data/simulation comparison in figure 5.18. The value of neutral pion mass fluctuates from run to run, where some runs show a downwards fluctuation. Figure 5.20 shows the m_{π^0} for run 6291 where the m_{π^0} is close to the expected PDG value, and run 6343 where the neutral pion mass has a downwards fluctuation. The cause of these downwards fluctuations is not fully understood, but it is likely connected to a variation in the response of the LKr.

To mitigate the effect of the run dependence of the m_{π^0}, the energy of the LKr clusters used for the π^0 were scaled on a per run basis by a factor κ_γ^{run} calculated as:

$$\kappa_\gamma^{run} = \sqrt{\frac{m_{\pi^0}^{PDG}}{m_{\pi^0}^{run}}}, \tag{5.8}$$

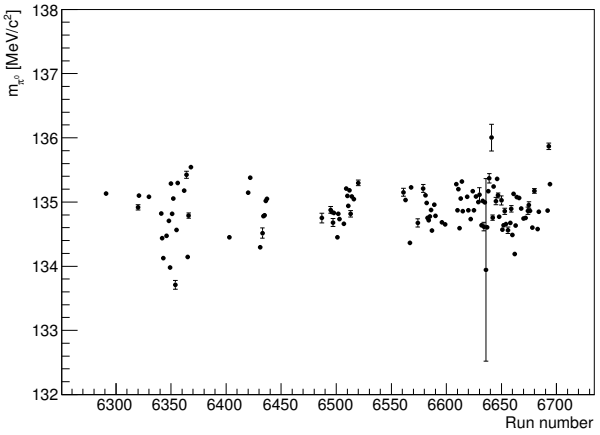

Figure 5.19: Value of the reconstructed m_{π^0} from $K_{2\pi}$ decays per run.

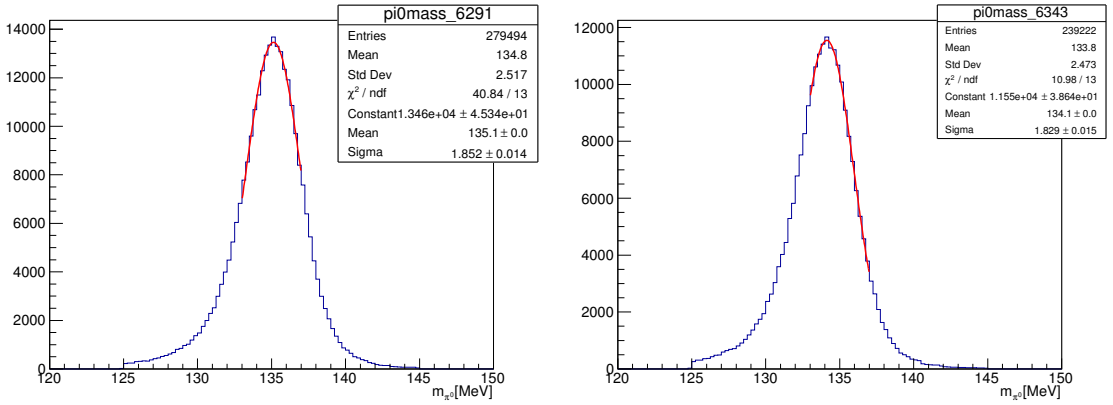

(a) m_{π^0}, run 6291

(b) m_{π^0}, run 6343

Figure 5.20: The reconstructed m_{π^0} distribution for a run 6291 (left), where the neutral pion mass value is close to the PDG value, and run 6343 (right) where m_{π^0} is low.

where $m_{\pi^0}^{run}$ is the mean value of the reconstructed neutral pion mass for the run, from the events passing the $K_{2\pi}$ selection. Figure 5.21a shows the data/simulation agreement for the neutral pion mass after the data energy-scaling has been applied. To reduce the residual offset between data and simulation, a scale factor is applied to the energy of the simulation LKr clusters used to reconstruct the π^0. A simulation scaling factor of 0.9955 was found to bring the data/simulation agreement for the m_{π^0} and $m^2_{miss}(l^+ + \pi^0)$ distributions of $K_{2\pi}$, $K_{\mu 3}$, K_{e3}, and $K_{3\pi^0}$ decays to around 5%.

The m_{π^0} and $m^2_{miss}(l^+ + \pi^0)$ distributions of the isolated samples before and after the simulation E_γ scaling are shown in figures 5.21, 5.22, 5.23, and 5.24. $K_{\mu 3}$ decays were isolated by applying the following criteria on top of the fit sample selection:

- $m^2_{miss}(\pi^+) < 0.0062$ GeV^2/c^4
- $m^2_{miss}(\pi^+) > 0.0302$ GeV^2/c^4
- $|m^2_{miss}(\mu^+)| > 0.0005$ GeV^2/c^4
- At least one MUV3 candidate within 5 ns of T_{KTAG}, geometrically associated to the track [46]

The first three cuts exploit the kinematics of the signal and background decays. The first criterion is used to reject $K_{3\pi^0}$ decays, whereas the next one reduces contributions from $K_{2\pi}$. The third cut rejects events with $K_{\mu 2}$ decays. The requirement of at least one matched MUV3 candidate only selects events with muons in them.

To obtain an enriched sample of K_{e3} decays, the following conditions were used:

- $m^2_{miss}(\pi^+) < 0.0062$ GeV^2/c^4
- $m^2_{miss}(\pi^+) > 0.0302$ GeV^2/c^4
- $E^{LKr}_{track}/P^{STRAW}_{track} > 0.9$
- No MUV3 candidate within 5 ns of T_{KTAG}

The first two conditions plays the same role as in the $K_{\mu 3}$ selection, to reject $K_{3\pi^0}$ and $K_{2\pi}$ decays respectively. The $E^{LKr}_{track}/P^{STRAW}_{track}$ cut identifies electrons, since they leave all of their energy in the LKr, and hence $E^{LKr}_{track}/P^{STRAW}_{track} \approx 1$. The last criterion vetoes events with muons in them.

The sample of $K_{3\pi^0}$ decays was isolated using the following selection

- $m^2_{miss}(\pi^+) > 0.07$ GeV^2/c^4
- $E^{LKr}_{track}/P^{STRAW}_{track} < 0.8$
- No MUV3 candidate within 5 ns of T_{KTAG}

The missing-mass cut in the $K_{3\pi^0}$ selections positively identifies $K_{3\pi^0}$ decays. The next two PID conditions reject events with electrons and muons respectively.

The plots obtained from these control samples demonstrate the overall data/simulation agreement which can be expected from the fit sample.

The fit sample $m^2_{miss}(l)$ distributions are shown in figure 5.25.

The peak at $m^2_{miss}(\mu^+)$ which is seen in data in figure 5.25b is from $K_{\mu 2}$ decays which have been matched with an accidental π^0. Applying the fit selection on a $K_{\mu 2}$ simulation sample with injected pileup results in zero events passing the selection, meaning this particular pileup effect seen in data is not reproduced by the current pileup simulation. In order to remove the $K_{\mu 2}$ decays from the fit sample, events with $-0.005 < m^2_{miss}(\mu^+) < 0.005$ GeV^2/c^4 are rejected.

The three-body missing-mass distributions before and after the LKr cluster energy scaling are shown in figure 5.26. The distributions with the energy scaling applied (right)

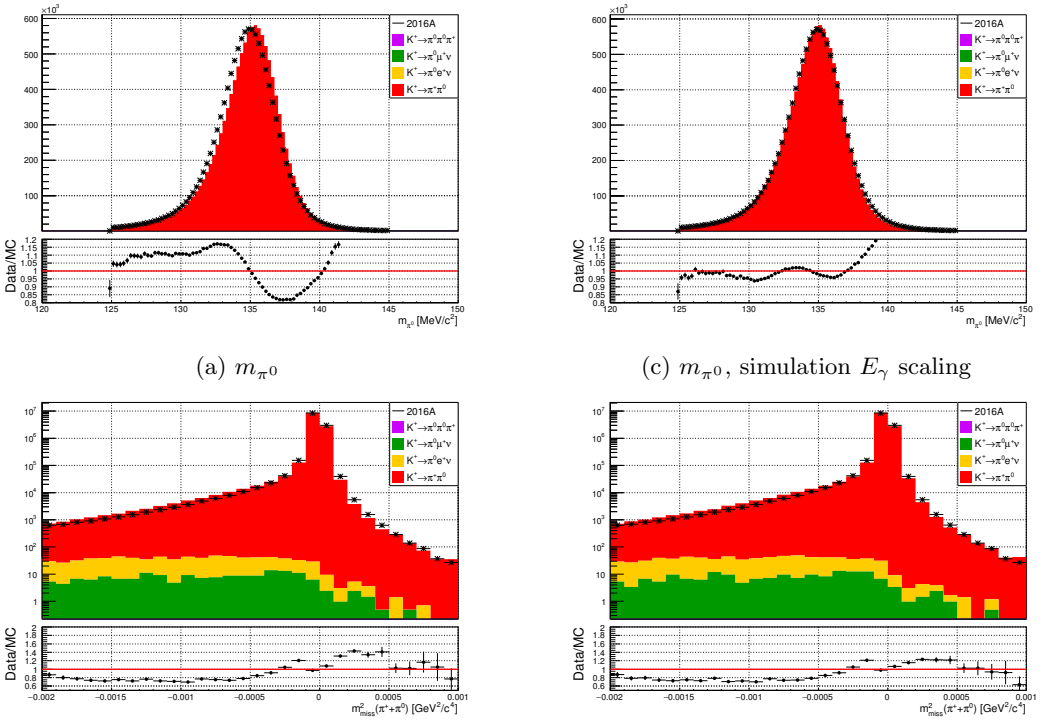

(a) m_{π^0}

(c) m_{π^0}, simulation E_γ scaling

(b) $m^2_{miss}(\pi^+ + \pi^0)$

(d) $m^2_{miss}(\pi^+ + \pi^0)$, simulation E_γ scaling

Figure 5.21: Plots of m_{π^0} and $m^2_{miss}(\pi^+ + \pi^0)$ without (left) and with the simulation photon energy scaling for $K_{2\pi}$.

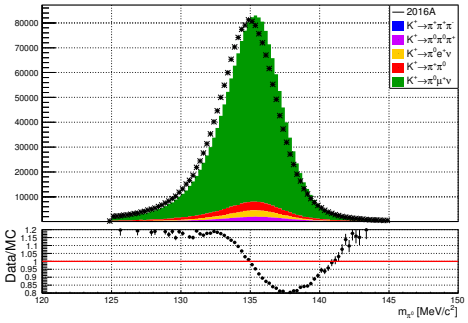

(a) m_{π^0}, data E_γ scaling

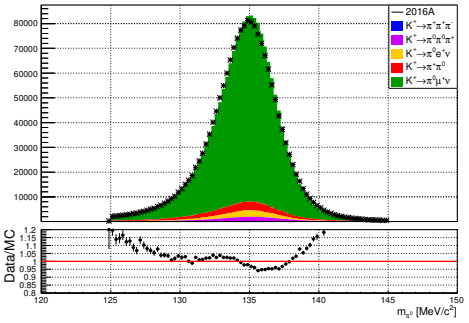

(c) m_{π^0}, data and simulation E_γ scaling

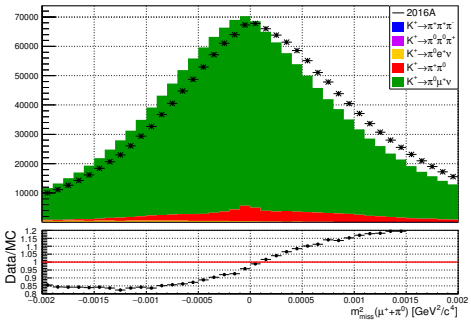

(b) $m^2_{miss}(\mu^+ + \pi^0)$, data E_γ scaling

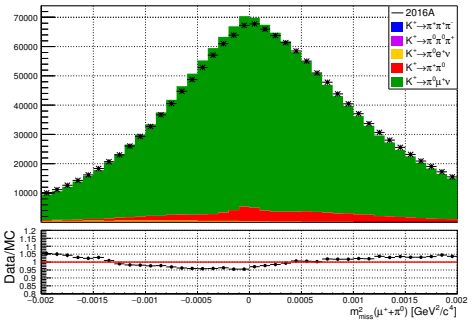

(d) $m^2_{miss}(\mu^+ + \pi^0)$, data and simulation E_γ scaling

Figure 5.22: Plots of m_{π^0} and $m^2_{miss}(\mu^+ + \pi^0)$ without (left) and with the simulation photon energy scaling for $K_{\mu 3}$ decays.

will be the ones used to perform the K_{l3} fit. The number of simulation events surviving the fit selection and corresponding sample acceptances are listed in table 5.1.

Sample	Number of events		Acceptance
	Generated	Fit sel. + $K_{\mu 2}$ cut	Fit sel. + $K_{\mu 2}$ cut
$K^+ \to \pi^+\pi^0$	3.6705×10^7	5.2373×10^6	$0.14268 \pm 5.77 \times 10^{-5}$
$K^+ \to \pi^0\mu^+\nu_\mu$	3.0957×10^7	3.7753×10^6	$0.12195 \pm 5.88 \times 10^{-5}$
$K^+ \to \pi^0 e^+\nu_e$	3.1982×10^7	2.6317×10^6	$0.08229 \pm 4.86 \times 10^{-5}$
$K^+ \to \pi^+\pi^0\pi^0$	5.2576×10^7	4.1038×10^6	$0.07806 \pm 3.70 \times 10^{-5}$
$K^+ \to \pi^+\pi^+\pi^-$	4.5309×10^7	3316	$(7.31858 \pm 0.12709) \times 10^{-5}$

Table 5.1: The GTK fit selection acceptances for each simulation sample.

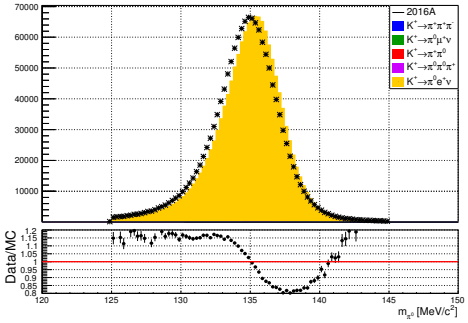

(a) m_{π^0}, data E_γ scaling

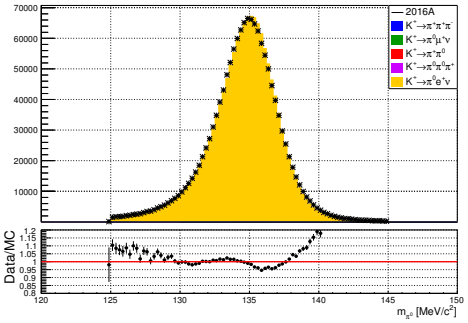

(c) m_{π^0}, data and simulation E_γ scaling

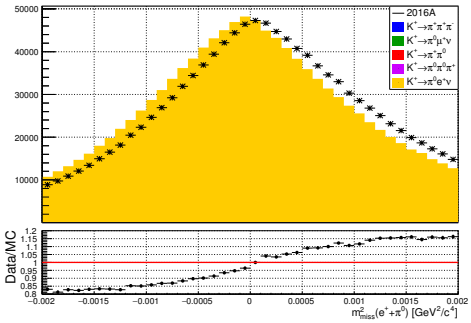

(b) $m^2_{miss}(e^+ + \pi^0)$, data E_γ scaling

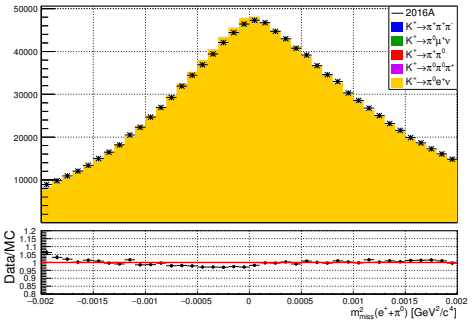

(d) $m^2_{miss}(e^+ + \pi^0)$, data and simulation E_γ scaling

Figure 5.23: Plots of m_{π^0} and $m^2_{miss}(\mu^+ + \pi^0)$ without (left) and with the simulation photon energy scaling for K_{e3} decays.

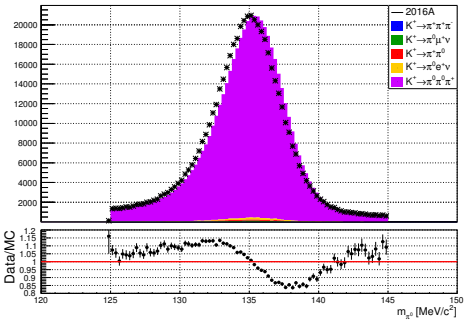

(a) m_{π^0} with data E_γ scaling

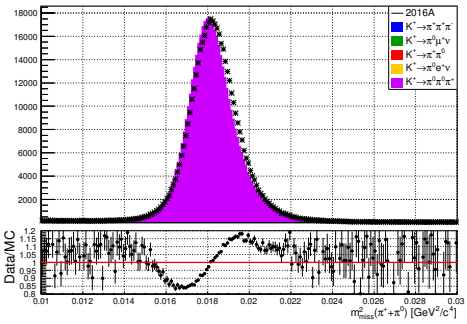

(b) $m^2_{miss}(\pi^+ + \pi^0)$ with data E_γ scaling

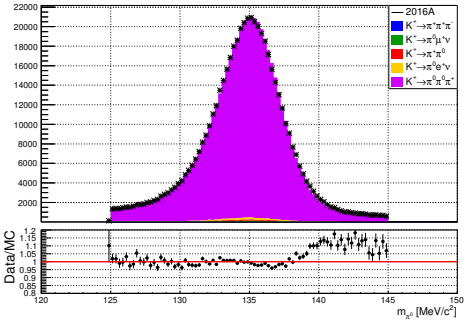

(c) m_{π^0}, data and simulation E_γ scaling

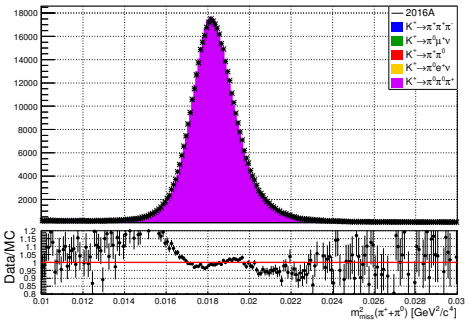

(d) $m^2_{miss}(\pi^+ + \pi^0)$, data and simulation E_γ scaling

Figure 5.24: Plots of m_{π^0} and $m^2_{miss}(\pi^+ + \pi^0)$ without (left) and with the simulation photon energy scaling for $K_{3\pi^0}$ decays.

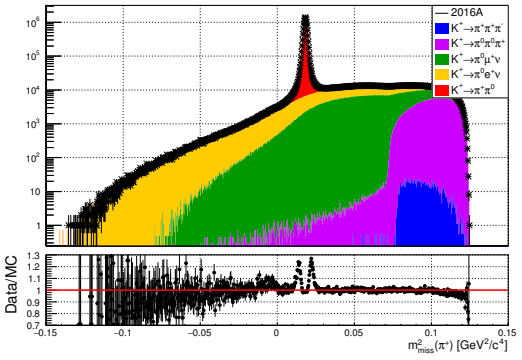

(a) $m^2_{miss}(\pi^+)$

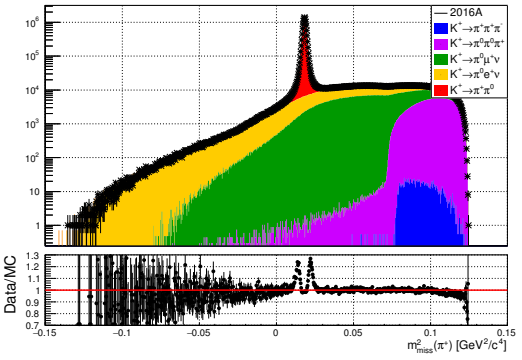

(d) $m^2_{miss}(\pi^+)$, $K_{\mu 2}$ cut.

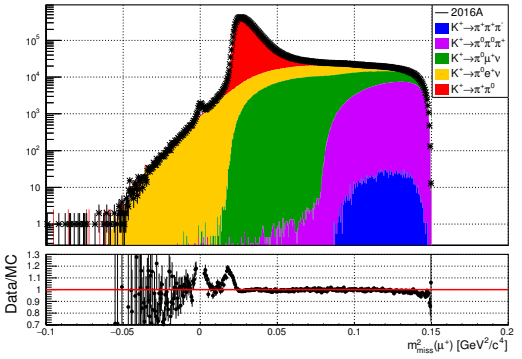

(b) $m^2_{miss}(\mu^+)$

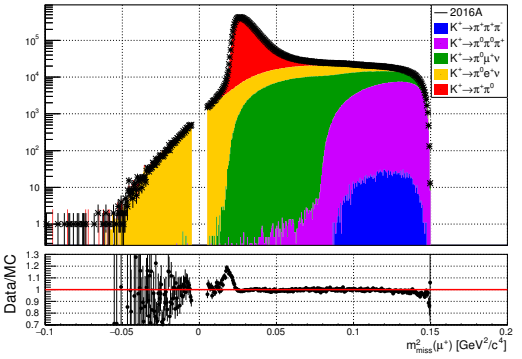

(e) $m^2_{miss}(\mu^+)$, $K_{\mu 2}$ cut.

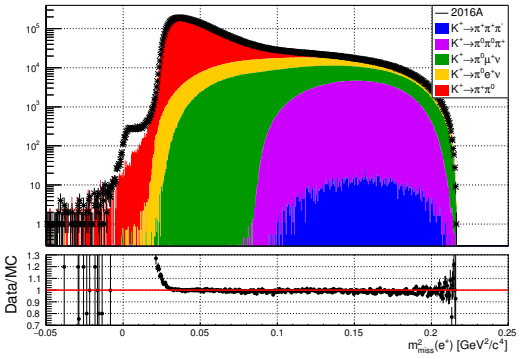

(c) $m^2_{miss}(e^+)$

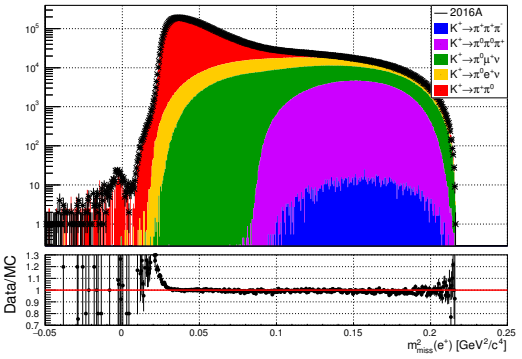

(f) $m^2_{miss}(e^+)$, $K_{\mu 2}$ cut.

Figure 5.25: Plots of the two-body missing-mass, calculated with GTK kaons, for the π^+, μ^+, and e^+ hypotheses for the fit sample.

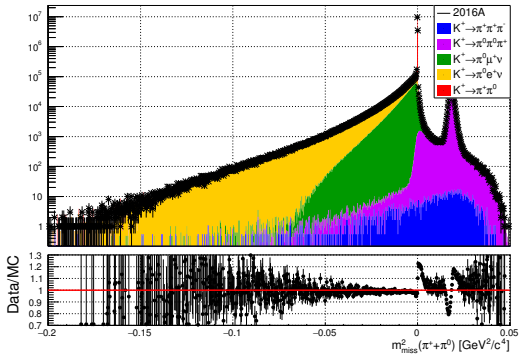

(a) $m^2_{miss}(\pi^+ + \pi^0)$

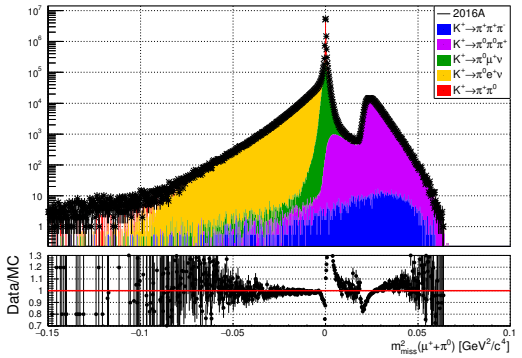

(b) $m^2_{miss}(\mu^+ + \pi^0)$

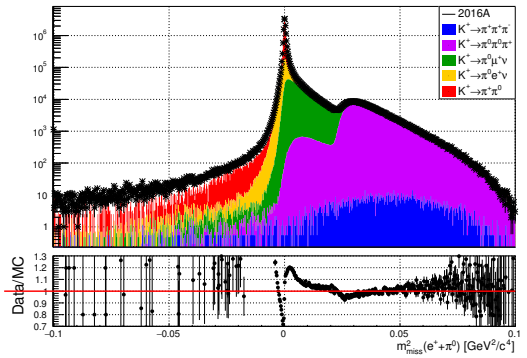

(c) $m^2_{miss}(e^+ + \pi^0)$

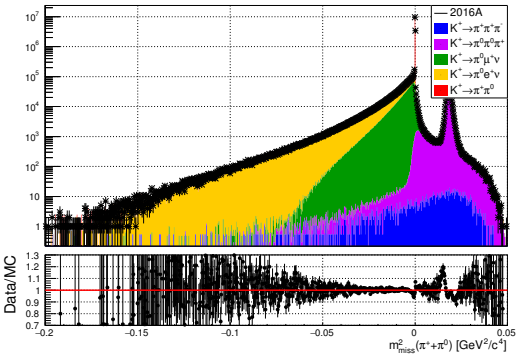

(d) $m^2_{miss}(\pi^+ + \pi^0)$, data and simulation E_γ scaling

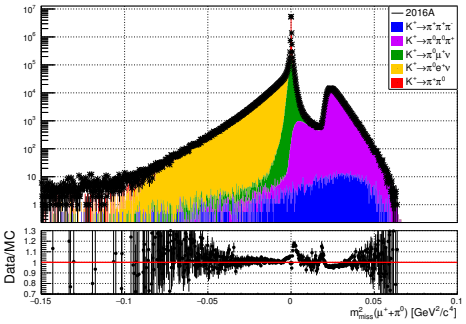

(e) $m^2_{miss}(\mu^+ + \pi^0)$, data and simulation E_γ scaling

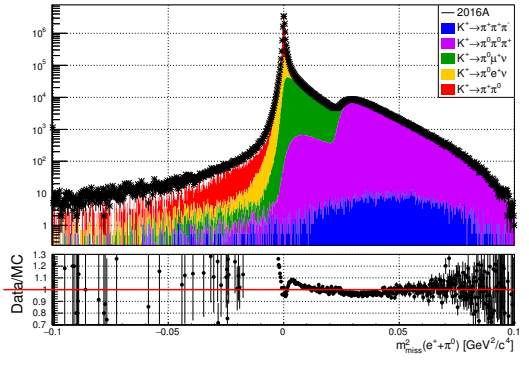

(f) $m^2_{miss}(e^+ + \pi^0)$, data and simulation E_γ scaling

Figure 5.26: Plots of the three-body missing-mass for the π^+, $\mu+$, and e^+ hypotheses for the GTK fit sample, without (left) and with (right) the simulation photon energy scaling.

5.4 Agreement with nominal kaons

As for the GTK, the data/simulation agreement for the nominal koan selection is studied with a focus on the two and three-body missing-mass distributions.

5.4.1 Beam spectrum weighting

Figure 5.27a shows the $m^2_{miss}(\pi)$ distribution for $K_{2\pi}$ decays. The effect of the difference in beam tuning between data and simulation can be seen in the $K_{2\pi}$ peak. The worse m^2_{miss} resolution causes the peak in figure 5.27a to be wider than 5.2b. The nominal kaon-downstream track CDA distribution for data and simulation is shown in figure 5.28, where the higher kinematic resolution is also apparent.

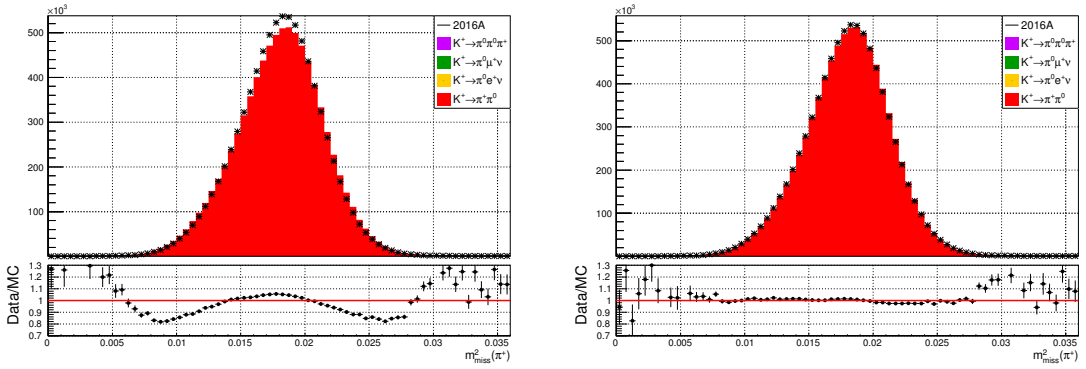

(a) $m^2_{miss}(\pi^+)$ (b) $m^2_{miss}(\pi^+)$, weighted

Figure 5.27: Data/simulation comparison of the $m^2_{miss}(\pi^+)$ for $K_{2\pi}$ selected events using a nominal kaon, with weights w_K applied.

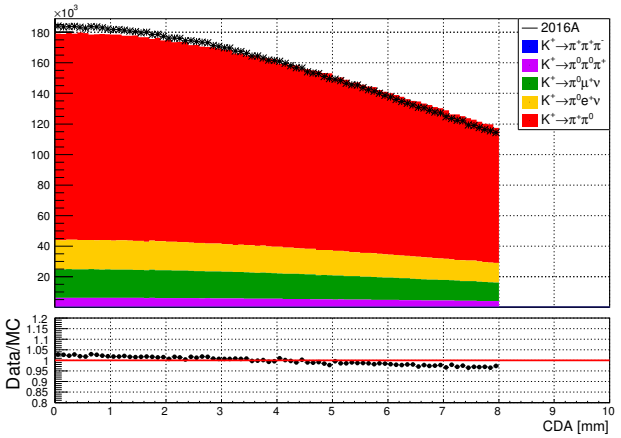

Figure 5.28: Data/simulation comparison of the CDA between a nominal kaon and downstream tracks for events passing the fit selection.

To correct for the difference in beam tuning, simulation events are weighted based on the true kaon momentum and the data/simulation ratio amongst the P_x. P_y, and P_z beam components. The beam spectrum in data and simulation is obtained from reconstructed GTK candidates, which give the maximum discriminant described in equation 4.7. For each simulation event, a weight is calculated using the P_x, P_y and P_z components of the true kaon. The weight for each momentum component is obtained by directly sampling the histograms in figure 5.29, with the final weight being the product of three:

$$w_K = w_{P_x} \cdot w_{P_y} \cdot w_{P_z}. \tag{5.9}$$

The ratios of the P_x, P_y, and P_z beam components for data and Monte Carlo can also be obtained from fully reconstructed $K_{3\pi}$ decays, however the weights based on the GTK candidates were found to give better data/simulation agreement for the current nominal kaon selection. The missing-mass distribution after the weighting is shown in figure 5.27b, where significant improvement can be seen. The effect of weighting on the three-body missing-mass distributions can be seen in figures 5.31, 5.33, 5.35, and 5.37.

5.4.2 m_{π^0}

As for the GTK selection, a run dependent E_γ scaling is applied to the data, along with a constant simulation factor of 0.9975. Figures 5.30, 5.32, 5.34, 5.36 show the m_{π^0} distributions before and after the energy scaling. The weighted and E_γ corrected three-body missing-mass distributions are shown in figures 5.31, 5.33, 5.35, and 5.37.

Applying the fit selection where a nominal kaon is used to perform the upstream-downstream track matching on the data and MC samples, yields the two-body missing-mass plots in figure 5.38. As before, a cut on the $m^2_{miss}(\mu^+)$ is used to reduce the contribution of accidentals $K_{\mu 2}$ decays. Due to the worse missing-mass resolution, the cut is widened to $|m^2_{miss}(\mu^+)| > 0.001$ GeV^2/c^4. The effect of the cut can be seen in figure 5.38.

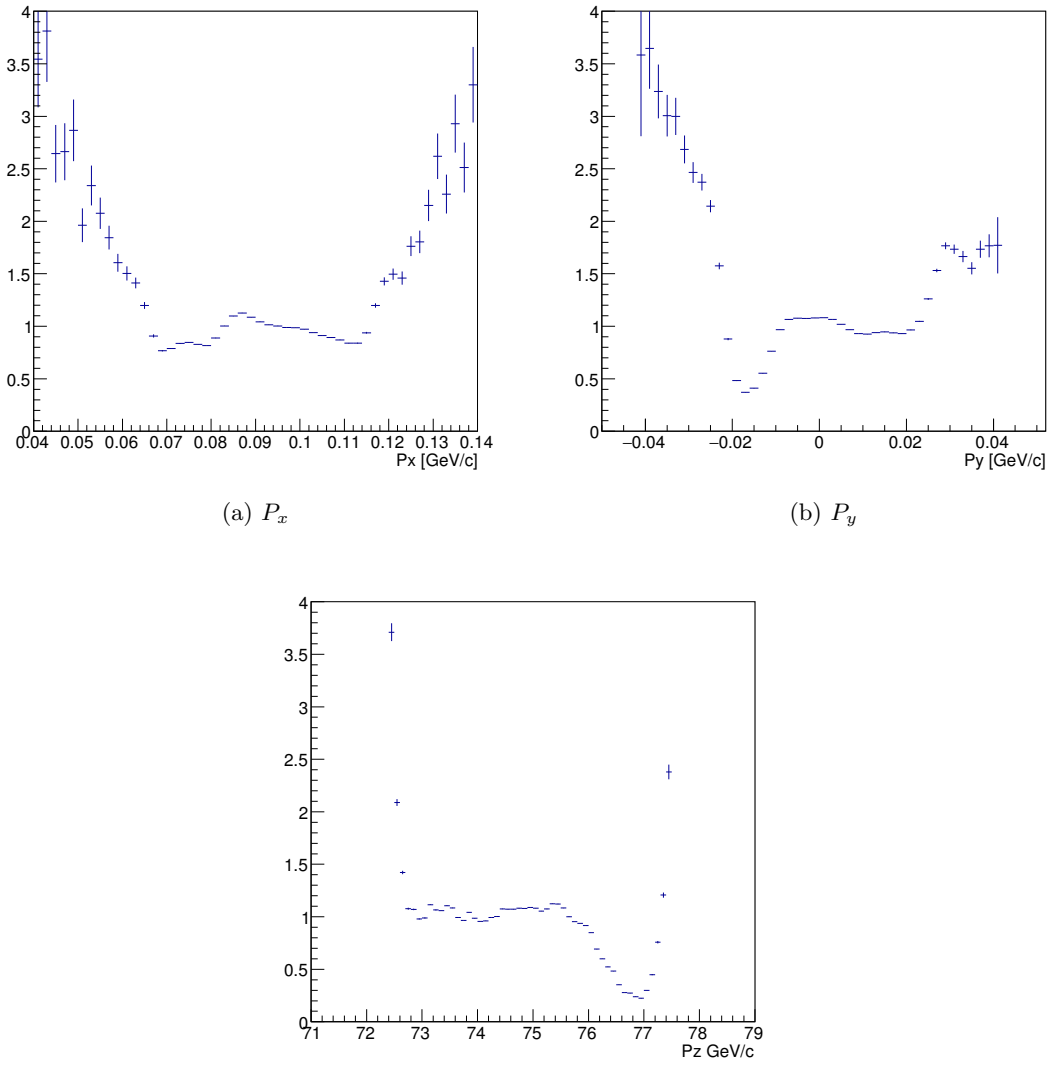

(a) P_x

(b) P_y

(c) P_z

Figure 5.29: Plots of the data/simulation ratio of the x, y, z components of the reconstructed kaon momentum from the GTK.

Figures 5.39 and 5.40 show the comparisons between the unweighted and weighted two and three-body missing-mass distributions for events passing the fit sample selection.

The weighted and E_γ scaled distributions shown on the right of figure 5.41 are the ones used for the fit.

The acceptance of each simulation sample for the nominal kaon fit selection are listed in table 5.2. Several techniques were developed to improve data/simulation agreement, using isolated samples of $K_{2\pi}$, $K_{\mu 3}$, K_{e3}, and $K_{3\pi^0}$ decays; consequently reducing data/simulation discrepancies in the GTK and nominal kaon fit samples distributions to mostly

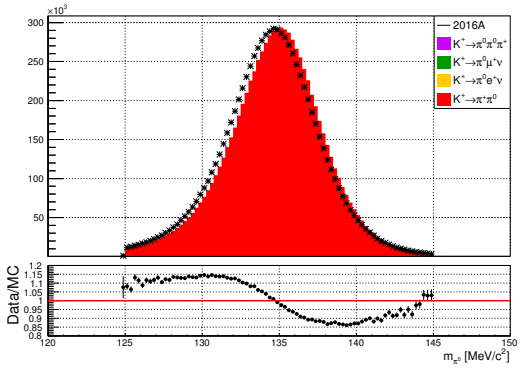

(a) m_{π^0}

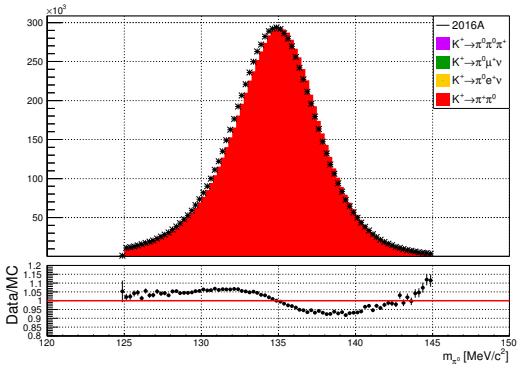

(b) m_{π^0}, data E_γ correction

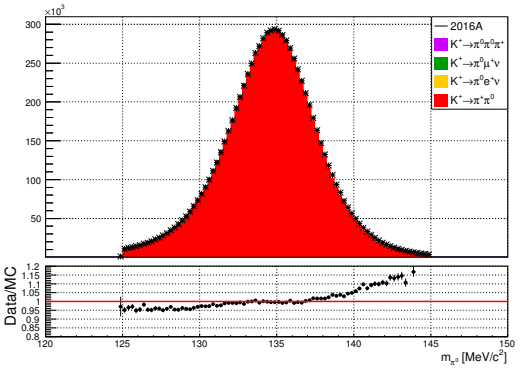

(c) m_{π^0}, data and simulation E_γ correction

Figure 5.30: Data/simulation comparison of the reconstructed m_{π^0} from $K_{2\pi}$ decays.

below 10%. With the improved data/simulation agreement, a sample fraction fit was attempted using the distributions presented in this chapter.

Sample	Number of events		Acceptance
	Generated	Fit sel. + $K_{\mu 2}$ cut	Fit sel. + $K_{\mu 2}$ cut
$K^+ \to \pi^+\pi^0$	3.6705×10^7	4.0617×10^6	$0.11066\pm5.17795\times10^{-5}$
$K^+ \to \pi^0\mu^+\nu_\mu$	3.0957×10^7	2.9132×10^6	$0.09410\pm5.24761\times10^{-5}$
$K^+ \to \pi^0 e^+\nu_e$	3.1982×10^7	2.0123×10^6	$0.06292\pm4.29367\times10^{-5}$
$K^+ \to \pi^+\pi^0\pi^0$	5.2576×10^7	3.1350×10^6	$0.05963\pm3.26572\times10^{-5}$
$K^+ \to \pi^+\pi^+\pi^-$	4.5309×10^7	2506	$(5.53087 \pm 0.11048) \times 10^{-5}$

Table 5.2: The nominal kaon fit selection acceptances for each simulation sample.

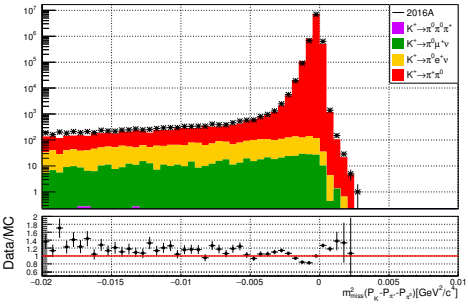

(a) $m^2_{miss}(\pi^+ + \pi^0)$

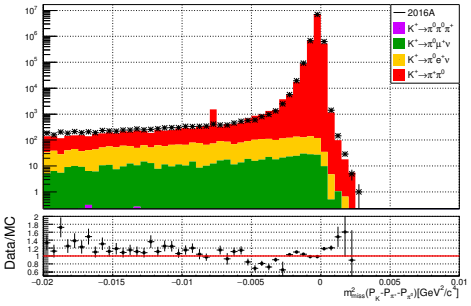

(b) $m^2_{miss}(\pi^+ + \pi^0)$, weighted

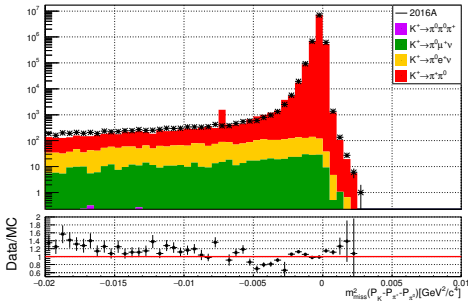

(c) $m^2_{miss}(\pi^+ + \pi^0)$, weighted, E_γ correction

Figure 5.31: Plots of $m^2_{miss}(\pi^+ + \pi^0)$ from $K_{2\pi}$ decays without corrections, with beam weights applied, and finally with both weights and E_γ scaling applied.

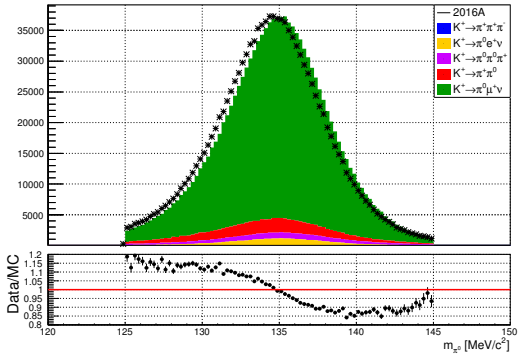

(a) m_{π^0}

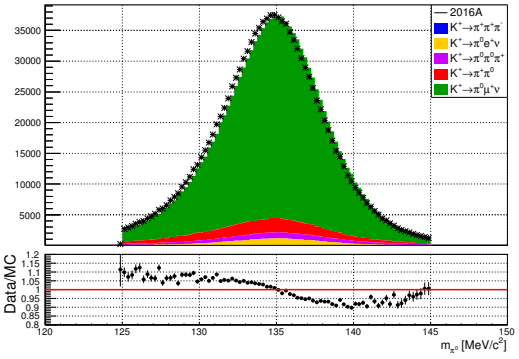

(b) m_{π^0}, data E_γ correction

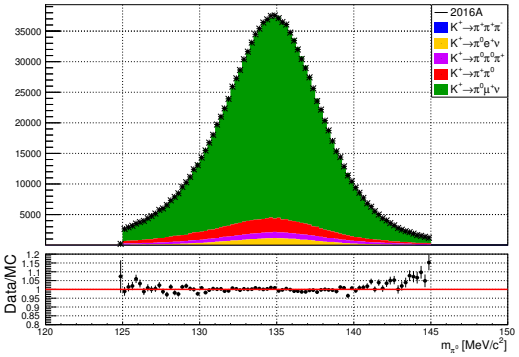

(c) m_{π^0}, data and simulation E_γ correction

Figure 5.32: Data/simulation comparison of the reconstructed m_{π^0} from $K_{\mu 3}$ decays.

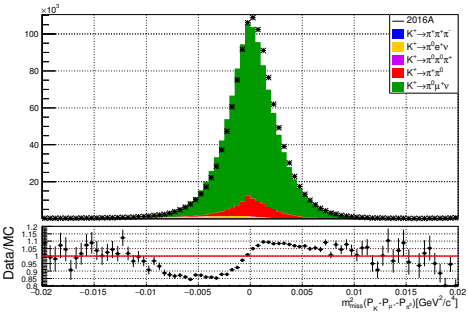

(a) $m^2_{miss}(\mu^+ + \pi^0)$

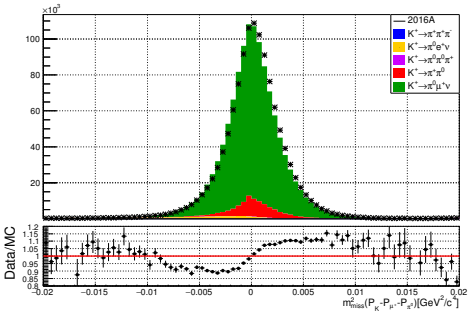

(b) $m^2_{miss}(\mu^+ + \pi^0)$, weighted

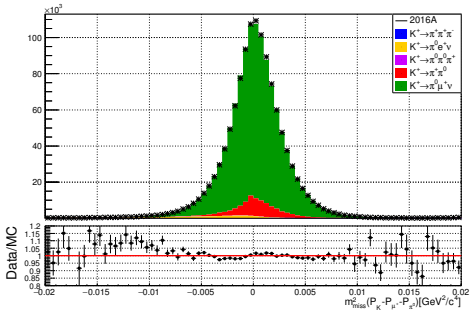

(c) $m^2_{miss}(\mu^+ + \pi^0)$, weighted, E_γ correction

Figure 5.33: Plots of $m^2_{miss}(\mu^+ + \pi^0)$ from $K_{\mu 3}$ decays without corrections, with beam weights applied, and finally with both weights and E_γ scaling applied.

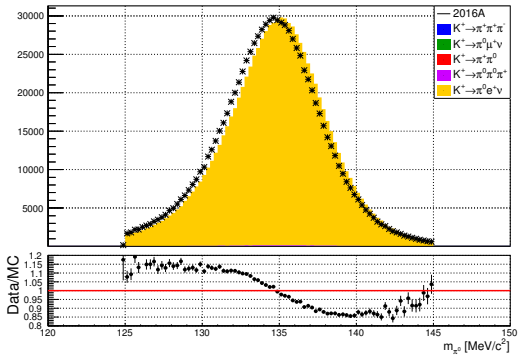

(a) m_{π^0}

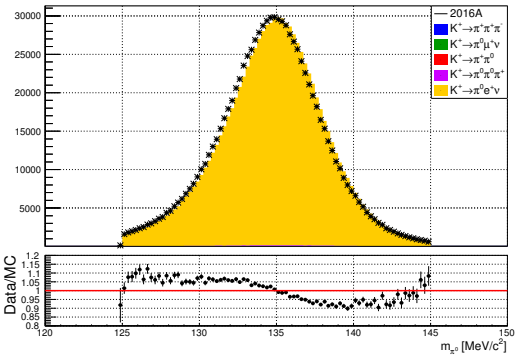

(b) m_{π^0}, data E_γ correction

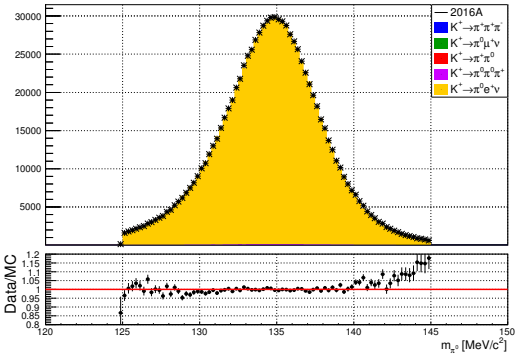

(c) m_{π^0}, data and simulation E_γ correction

Figure 5.34: Data/simulation comparison of the reconstructed m_{π^0} from K_{e3} decays.

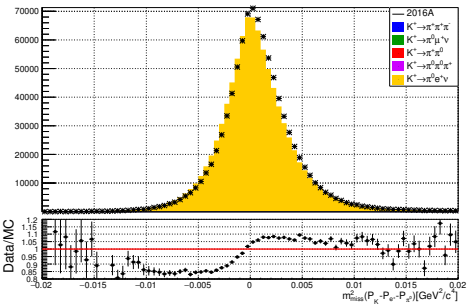

(a) $m^2_{miss}(e^+ + \pi^0)$

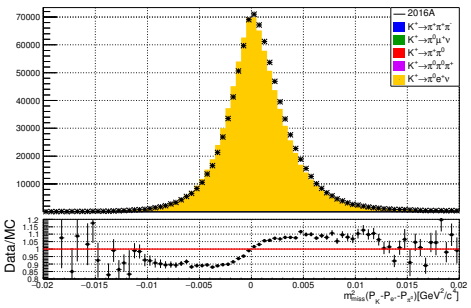

(b) $m^2_{miss}(e^+ + \pi^0)$, weighted

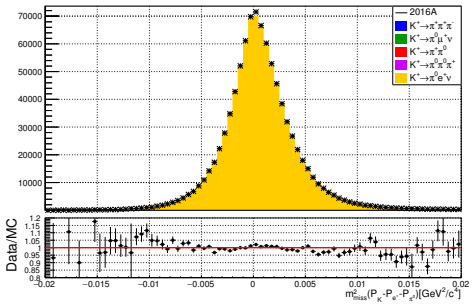

(c) $m^2_{miss}(e^+ + \pi^0)$, weighted, E_γ correction

Figure 5.35: Plots of $m^2_{miss}(e^+ + \pi^0)$ from K_{e3} decays without corrections, with beam weights applied, and finally with both weights and E_γ scaling applied.

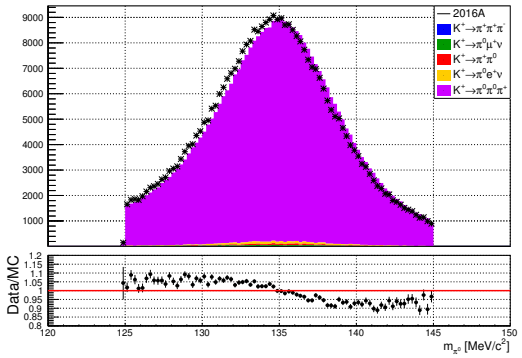

(a) m_{π^0}

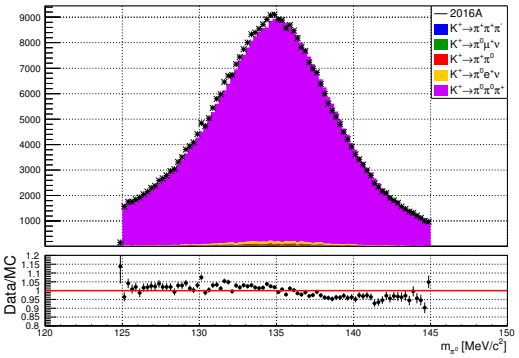

(b) m_{π^0}, data E_γ correction

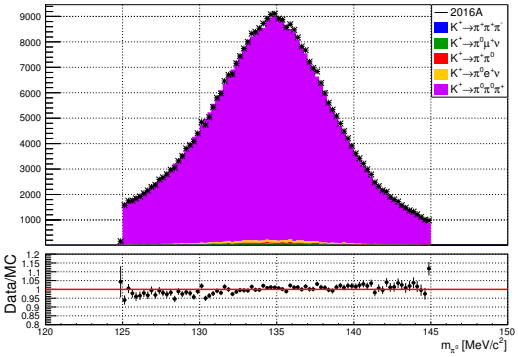

(c) m_{π^0}, data and MC E_γ correction

Figure 5.36: Data/simulation comparison of the reconstructed m_{π^0} from $K_{3\pi^0}$ decays.

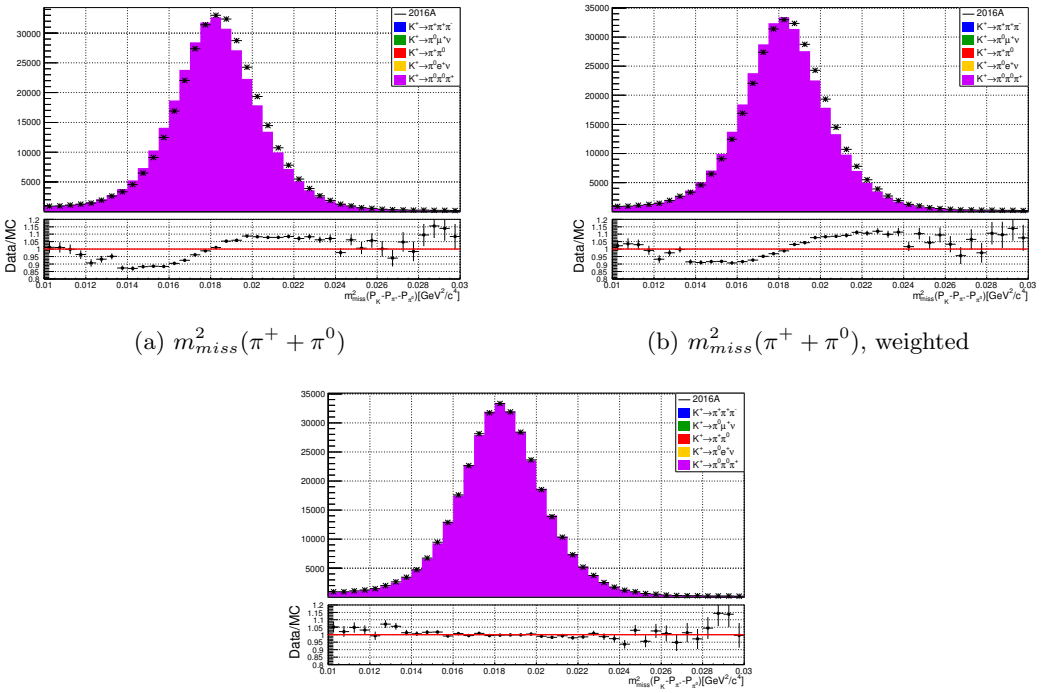

(a) $m^2_{miss}(\pi^+ + \pi^0)$

(b) $m^2_{miss}(\pi^+ + \pi^0)$, weighted

(c) $m^2_{miss}(\pi^+ + \pi^0)$, weighted, E_γ scaling

Figure 5.37: Plots of $m^2_{miss}(\pi^+ + \pi^0)$ from $K_{3\pi^0}$ decays without corrections, with beam weights applied, and finally with both weights and E_γ scaling applied.

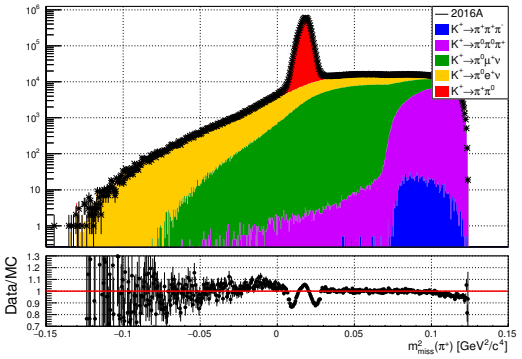

(a) $m^2_{miss}(\pi^+)$

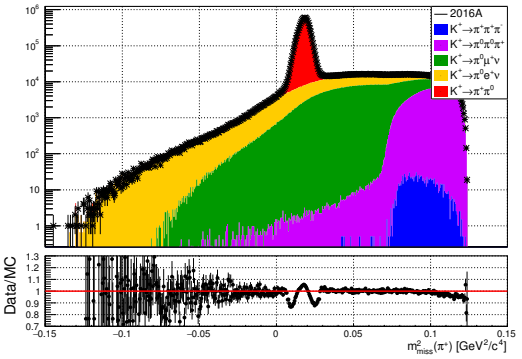

(d) $m^2_{miss}(\pi^+)$, $K_{\mu 2}$ cut

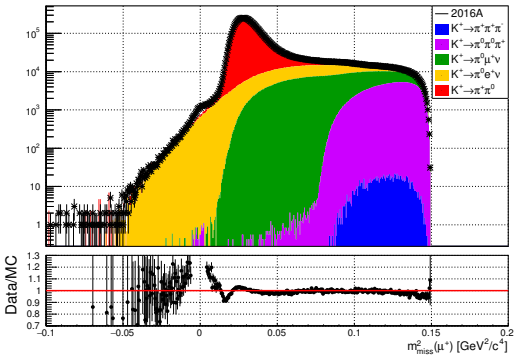

(b) $m^2_{miss}(\mu^+)$

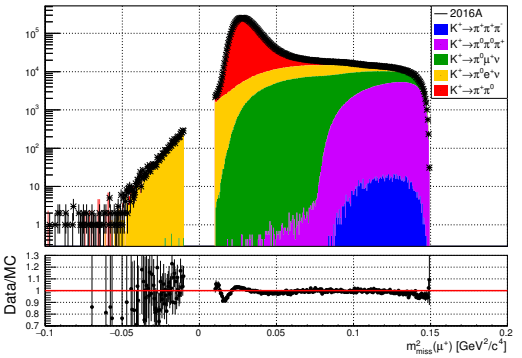

(e) $m^2_{miss}(\mu^+)$, $K_{\mu 2}$ cut

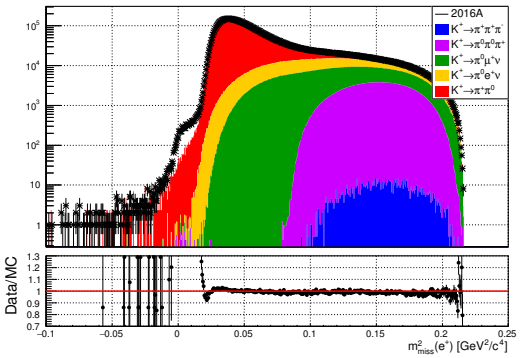

(c) $m^2_{miss}(e^+)$

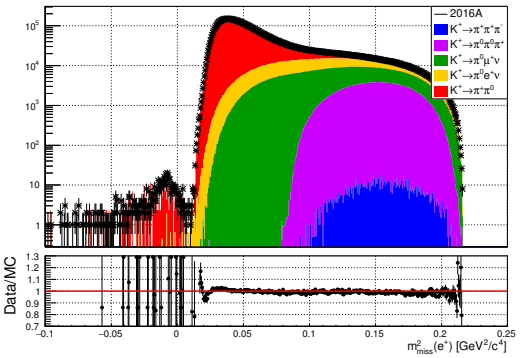

(f) $m^2_{miss}(e^+)$, $K_{\mu 2}$ cut

Figure 5.38: Plots of the two-body missing-mass, calculated with nominal kaon, for the π^+, $\mu+$, and e^+ hypotheses for the fit sample.

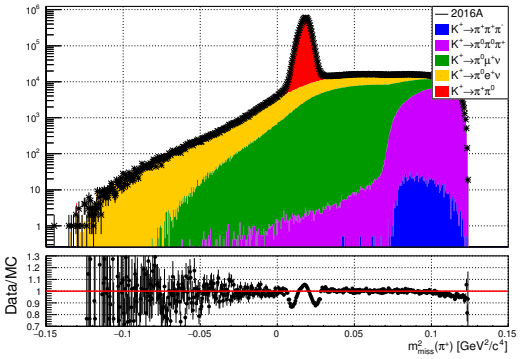

(a) $m^2_{miss}(\pi^+)$

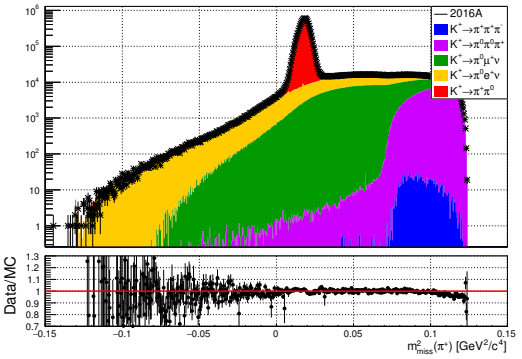

(d) $m^2_{miss}(\pi^+)$, weighted

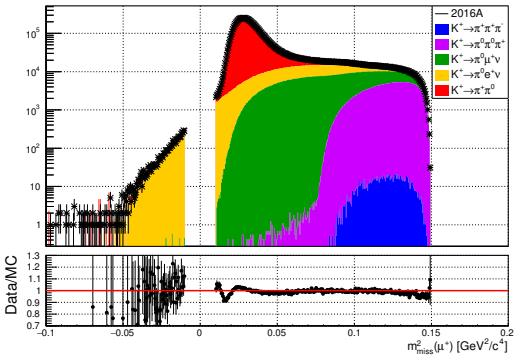

(b) $m^2_{miss}(\mu^+)$

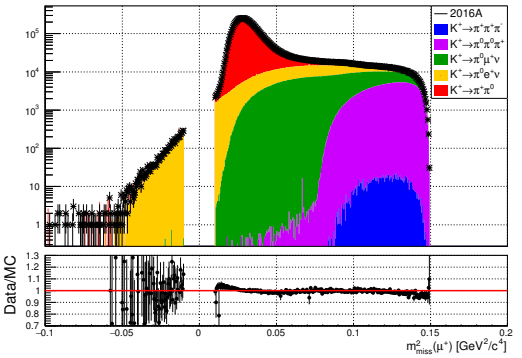

(e) $m^2_{miss}(\mu^+)$, weighted

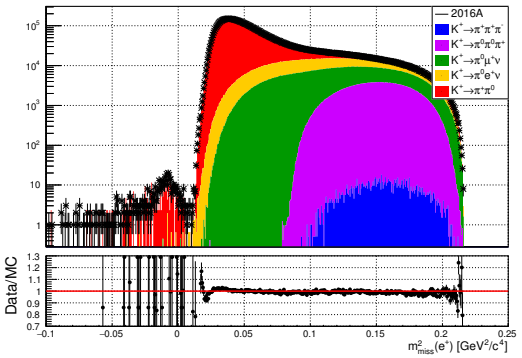

(c) $m^2_{miss}(e^+)$

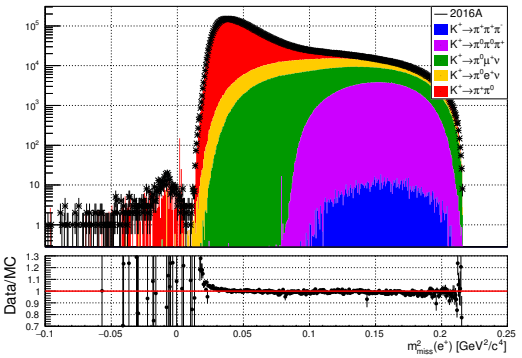

(f) $m^2_{miss}(e^+)$, weighted

Figure 5.39: Plots of the two-body missing-mass for the π^+, $\mu+$, and e^+ hypotheses for the nominal kaon fit sample without (left) and with (right) w_K weights applied.

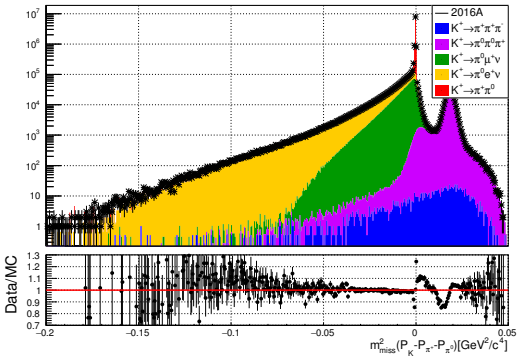

(a) $m^2_{miss}(\pi^+ + \pi^0)$

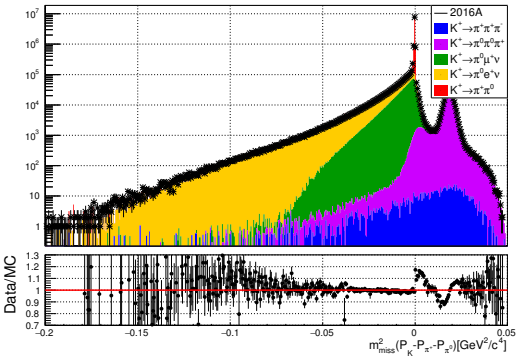

(d) $m^2_{miss}(\pi^+ + \pi^0)$, weighted

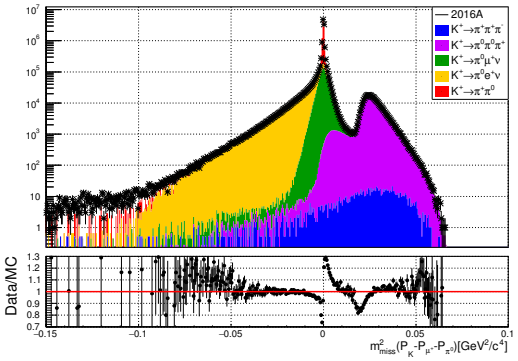

(b) $m^2_{miss}(\mu^+ + \pi^0)$

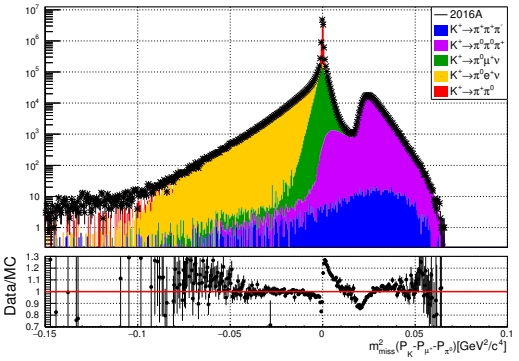

(e) $m^2_{miss}(\mu^+ + \pi^0)$, weighted

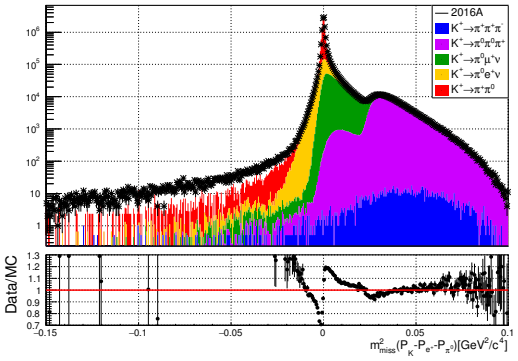

(c) $m^2_{miss}(e^+ + \pi^0)$

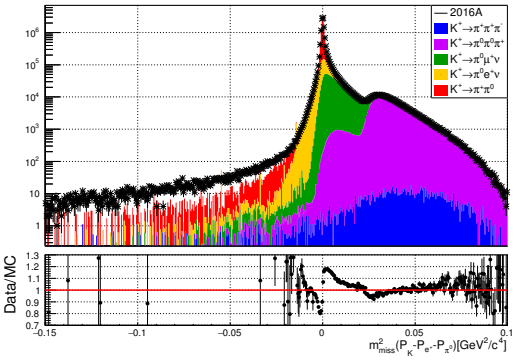

(f) $m^2_{miss}(e^+ + \pi^0)$, weighted

Figure 5.40: Plots of the three-body missing-mass for the π^+, $\mu+$, and e^+ hypotheses for the nominal kaon fit sample without (left) and with (right) w_K weights applied.

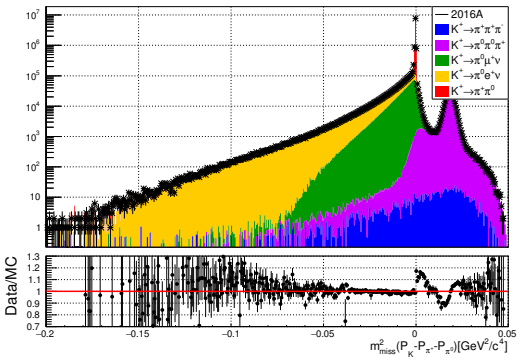

(a) $m^2_{miss}(\pi^+ + \pi^0)$, weighted

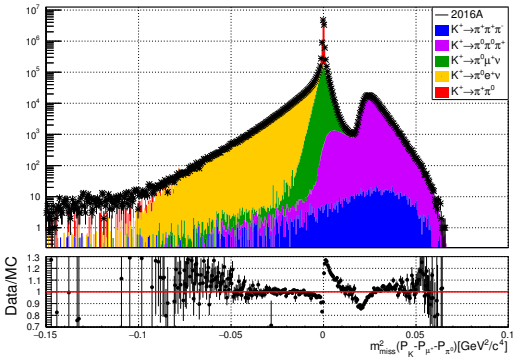

(b) $m^2_{miss}(\mu^+ + \pi^0)$, weighted

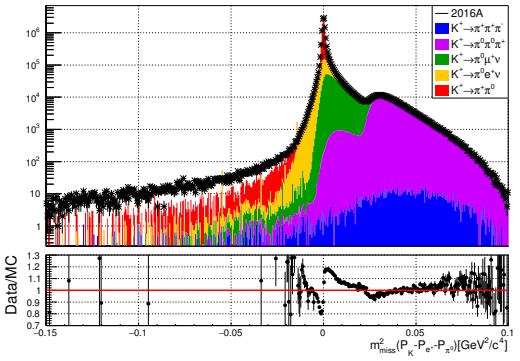

(c) $m^2_{miss}(e^+ + \pi^0)$, weighted

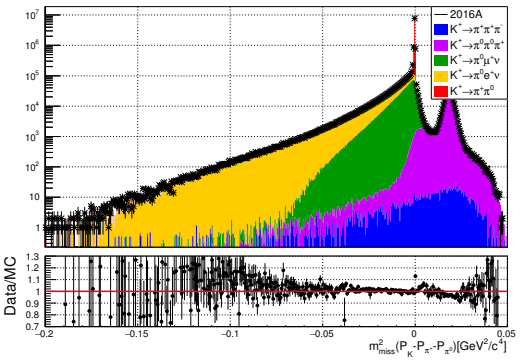

(d) $m^2_{miss}(\pi^+ + \pi^0)$, weighted, data+simulation E_γ scaling

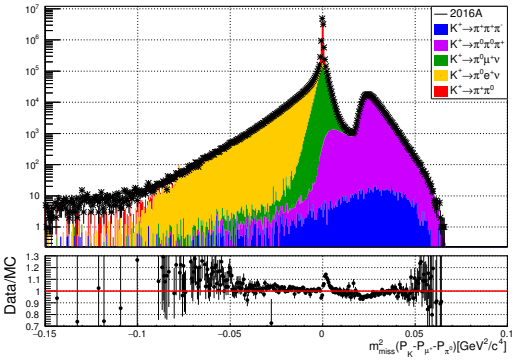

(e) $m^2_{miss}(\mu^+ + \pi^0)$, weighted, data+simulation E_γ scaling

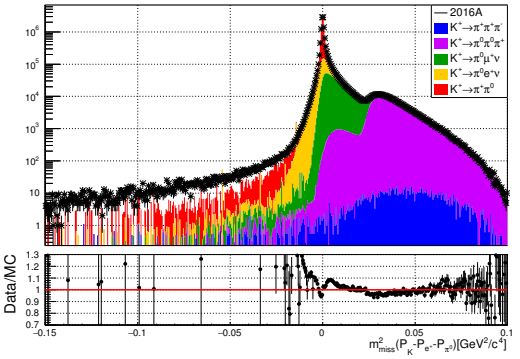

(f) $m^2_{miss}(e^+ + \pi^0)$, weighted, data+simulation E_γ scaling

Figure 5.41: Plots of the three-body missing-mass for the π^+, $\mu+$, and e^+ hypotheses for the nominal kaon fit sample without (left) and with (right) data and simulation photon energy scaling applied.

Chapter 6

K_{l3} branching fractions measurement

The contributions of each simulation sample in figures 5.26 and 5.41 can be determined via the fitting method described in section 4.2.1. Combining the result of the fit with acceptances in tables 5.1 and 5.2 gives the branching fraction of each sample. Past measurements of the branching fractions values present them as the ratios: $BF(K_{\mu 3})/BF(K_{e3})$, $BF(K_{\mu 3})/BF(K_{2\pi})$, and $BF(K_{e3})/BF(K_{2\pi})$. Using the ratio of branching fractions means that the majority of the systematic effects cancel out, e.g. track reconstruction or upstream-downstream track matching. The same methodology is adopted here, where the ratio of the branching fractions are extracted from the fit results.

6.1 Validation of fitting procedure

In order to validate the fitting procedure described in section 4.2.1, and make a preliminary assessment of the performance of the technique, the simulation samples from tables 5.1 and 5.2 were added together to create a "fake" data sample. The resulting dummy data histograms were used as the data input to the fit, along with the real individual simulation sample histograms.

Performing a fit on dummy data is also useful to check whether different combinations of variables, e.g. $m^2_{miss}(\pi^+)$ vs. $m^2_{miss}(\mu^+ + \pi^0)$ or $m^2_{miss}(\pi^+ + \pi^0)$ vs. $m^2_{miss}(e^+ + \pi^0)$, return consistent results. All combination of the four peaking missing-mass distributions, $m^2_{miss}(\pi)$, $m^2_{miss}(\pi + \pi^0)$, $m^2_{miss}(\mu + \pi^0)$, and $m^2_{miss}(e + \pi^0)$ were trialled, resulting in six missing-mass configurations.

The sample strength, S_j, for each simulation sample, j, is calculated as:

$$S_j = \epsilon_j \cdot BF_j^{\mathrm{PDG}}, \tag{6.1}$$

where ϵ_j is the acceptance of sample j, and BF_j^{PDG} is its branching fraction as given by the PDG [7]. Using S_j, the predicted sample fraction for sample j is given by:

$$P_j^{\mathrm{pred.}} = \frac{S_j}{\sum_{j=1}^{m} S_j}. \tag{6.2}$$

Tables 6.1 and 6.2 list the predicted sample fractions, along with the fractions obtained by fitting to the artificial data histograms, for the GTK and nominal kaon samples respectively. During the validation procedure it was found that the fit failed to converge for certain m^2_{miss} combinations if the $K_{3\pi}$ fraction was left to float, in those cases the $K_{3\pi}$ fraction was fixed to the predicted value. Fixed sample fractions in tables 6.1 and 6.2 are followed by "(f)" rather than the fraction uncertainty. The two dimensional plots of the artificial datasets used for the validation fit are shown in figures 6.1 (GTK) and 6.2 (nominal kaon).

Fit variables	Sample fraction				
	$K_{2\pi}$	$K_{\mu 3}$	K_{e3}	$K_{3\pi^0}$	$K_{3\pi}$
Simulation prediction	0.75370	0.10447	0.10662	0.03511	0.00010
$m^2_{miss}(\pi)$ v $m^2_{miss}(\pi + \pi^0)$	0.75376(42)	0.10444(21)	0.10662(21)	0.03511(6)	0.00010(1)
$m^2_{miss}(\pi)$ v $m^2_{miss}(\mu + \pi^0)$	0.75370(43)	0.10447(15)	0.10662(14)	0.03511(6)	0.00010(1)
$m^2_{miss}(\pi)$ v $m^2_{miss}(e + \pi^0)$	0.75372(43)	0.10446(15)	0.10662(16)	0.03511(7)	0.00010(1)
$m^2_{miss}(\pi + \pi^0)$ v $m^2_{miss}(\mu + \pi^0)$	0.75371(43)	0.10447(14)	0.10662(14)	0.03511(6)	0.00010(1)
$m^2_{miss}(\pi + \pi^0)$ v $m^2_{miss}(e + \pi^0)$	0.75373(43)	0.10447(13)	0.10662(13)	0.03511(6)	0.00010(1)
$m^2_{miss}(\mu + \pi^0)$ v $m^2_{miss}(e + \pi^0)$	0.75371(43)	0.10446(13)	0.10661(13)	0.03511(6)	0.00010(1)

Table 6.1: Sample fractions as obtained from a fit to the "dummy" GTK dataset.

Tables 6.1 and 6.2 show that all six variable combinations which were tried are able to separate the simulation samples for both the GTK and nominal kaon selections. The

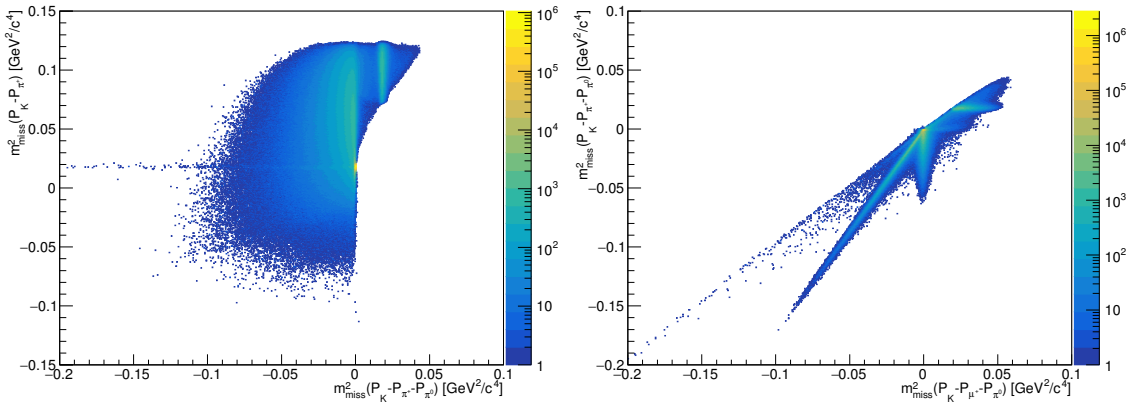

(a) $m^2_{miss}(\pi^+)$ vs. $m^2_{miss}(\pi^+ + \pi^0)$ (d) $m^2_{miss}(\pi^+ + \pi^0)$ vs. $m^2_{miss}(\mu^+ + \pi^0)$

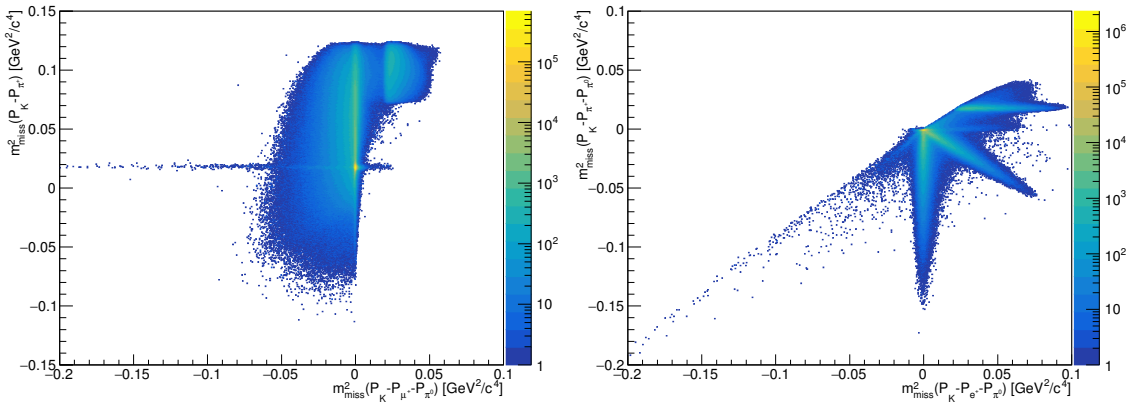

(b) $m^2_{miss}(\pi^+)$ vs. $m^2_{miss}(\mu^+ + \pi^0)$ (e) $m^2_{miss}(\pi^+ + \pi^0)$ vs. $m^2_{miss}(e^+ + \pi^0)$

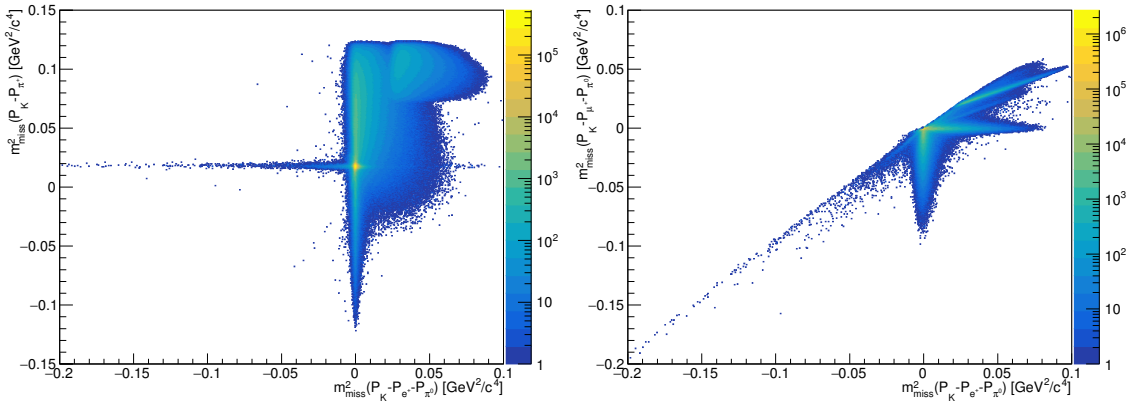

(c) $m^2_{miss}(\pi^+)$ vs. $m^2_{miss}(e^+ + \pi^0)$ (f) $m^2_{miss}(\mu^+ + \pi^0)$ vs. $m^2_{miss}(e^+ + \pi^0)$

2

Figure 6.1: GTK artificial data samples plotted in the six missing-mass combinations.

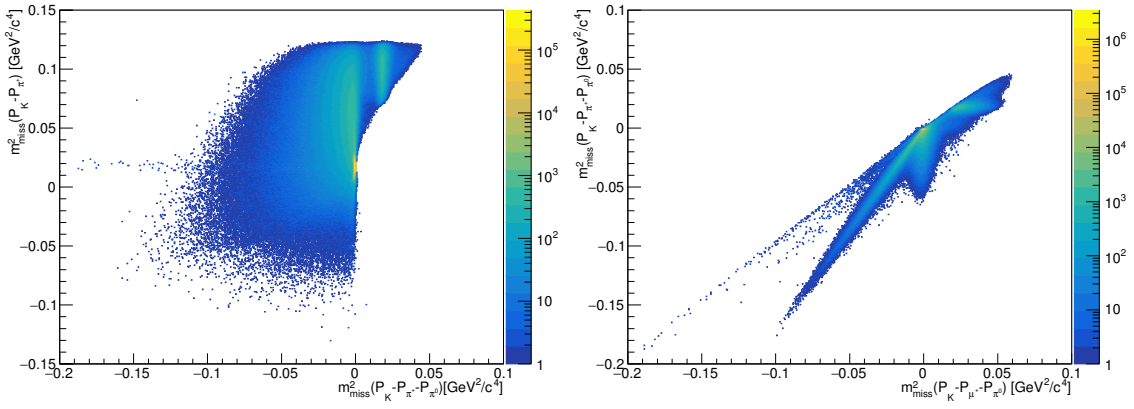

(a) $m^2_{miss}(\pi^+)$ vs. $m^2_{miss}(\pi^+ + \pi^0)$

(d) $m^2_{miss}(\pi^+ + \pi^0)$ vs. $m^2_{miss}(\mu^+ + \pi^0)$

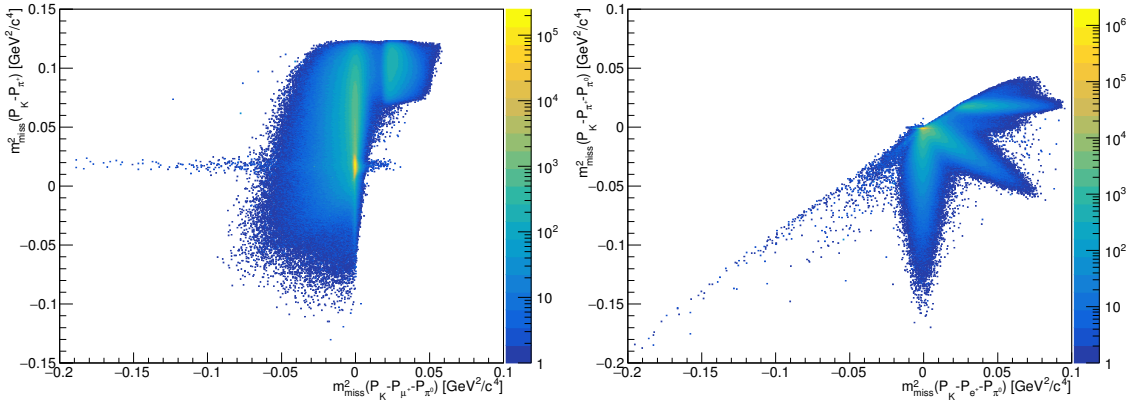

(b) $m^2_{miss}(\pi^+)$ vs. $m^2_{miss}(\mu^+ + \pi^0)$

(e) $m^2_{miss}(\pi^+ + \pi^0)$ vs. $m^2_{miss}(e^+ + \pi^0)$

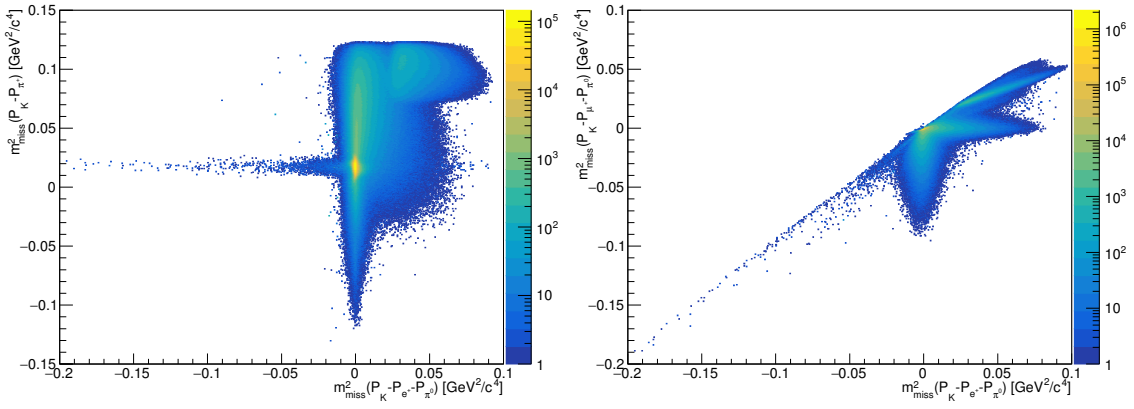

(c) $m^2_{miss}(\pi^+)$ vs. $m^2_{miss}(e^+ + \pi^0)$

(f) $m^2_{miss}(\mu^+ + \pi^0)$ vs. $m^2_{miss}(e^+ + \pi^0)$

2

Figure 6.2: Nominal kaon artificial data samples plotted in the six missing-mass combinations.

Fit variables	Sample fraction				
	$K_{2\pi}$	$K_{\mu 3}$	K_{e3}	$K_{3\pi^0}$	$K_{3\pi}$
Simulation prediction	0.75563	0.10421	0.10539	0.03467	0.00010
$m^2_{miss}(\pi)$ vs. $m^2_{miss}(\pi+\pi^0)$	0.75564(47)	0.10420(25)	0.10539(24)	0.03467(6)	0.00010(f)
$m^2_{miss}(\pi)$ vs. $m^2_{miss}(\mu+\pi^0)$	0.75566(47)	0.10421(17)	0.10539(17)	0.03467(6)	0.00010(f)
$m^2_{miss}(\pi)$ vs. $m^2_{miss}(e+\pi^0)$	0.75563(47)	0.10421(18)	0.10539(19)	0.03467(7)	0.00010(1)
$m^2_{miss}(\pi+\pi^0)$ vs. $m^2_{miss}(\mu+\pi^0)$	0.75563(47)	0.10421(16)	0.10539(16)	0.03467(6)	0.00010(1)
$m^2_{miss}(\pi+\pi^0)$ vs. $m^2_{miss}(e+\pi^0)$	0.75563(47)	0.10421(16)	0.10539(16)	0.03467(6)	0.00010(1)
$m^2_{miss}(\mu+\pi^0)$ vs. $m^2_{miss}(e+\pi^0)$	0.75563(47)	0.10421(16)	0.10539(16)	0.03467(6)	0.00010(1)

Table 6.2: Sample fractions as obtained from a fit to the "dummy" nominal kaon dataset. Sample fraction followed by "(f)" were fixed in that particular fit configuration.

uncertainties for five of the missing-mass configurations are very close to each other, the exception being $m^2_{miss}(\pi^+)$ vs. $m^2_{miss}(\pi^+ + \pi^0)$. In that missing-mass configuration the uncertainties on the $K_{\mu 3}$ and K_{e3} fractions are slightly larger when compared to the rest of the kinematic variables configurations. The larger uncertainties are attributed to the decreased decay mode separation in that particular missing-mass configuration. The fraction uncertainties from the GTK and nominal kaon selections are similar, with the fit on the GTK artificial data performing marginally better.

6.2 Fit to the data

Using the predicted sample proportions in tables 6.1 and 6.2 as initial parameter values, the fit was performed on the GTK and nominal kaon data, yielding the sample fractions in table 6.3 and 6.4 respectively. The fraction of the $K_{3\pi}$ sample was kept fixed at the predicted value of 0.00010. If the $K_{3\pi}$ proportion was left to float, it was consistently "fitted away", with the fit fraction result being $\mathcal{O}(10^{-10})$. The fixing of the $K_{3\pi}$ fraction is treated as a systematic uncertainty, and it is discussed in section 6.3.6.

Fit variables	Sample fraction				
	$K_{2\pi}$	$K_{\mu 3}$	K_{e3}	$K_{3\pi^0}$	$K_{3\pi}$
Simulation prediction	0.75370	0.10447	0.10662	0.03511	0.00010
$m^2_{miss}(\pi)$ v $m^2_{miss}(\pi+\pi^0)$	0.75640(37)	0.10661(19)	0.10283(19)	0.03405(5)	0.00010(f)
$m^2_{miss}(\pi)$ v $m^2_{miss}(\mu+\pi^0)$	0.75503(36)	0.10411(12)	0.10679(12)	0.03397(5)	0.00010(f)
$m^2_{miss}(\pi)$ v $m^2_{miss}(e+\pi^0)$	0.75481(39)	0.10425(11)	0.10698(13)	0.03387(5)	0.00010(f)
$m^2_{miss}(\pi+\pi^0)$ v $m^2_{miss}(\mu+\pi^0)$	0.75558(37)	0.10408(11)	0.10616(11)	0.03408(5)	0.00010(f)
$m^2_{miss}(\pi+\pi^0)$ v $m^2_{miss}(e+\pi^0)$	0.75591(32)	0.10402(11)	0.10589(11)	0.03399(5)	0.00010(f)
$m^2_{miss}(\mu+\pi^0)$ v $m^2_{miss}(e+\pi^0)$	0.75535(34)	0.10427(11)	0.10622(11)	0.03405(5)	0.00010(f)

Table 6.3: Sample fractions as obtained from the K_{l3} fit on the GTK data.

The proportions given in tables 6.3 and 6.4 can be used to calculate the branching fraction ratios using the acceptances from tables 5.1 and 5.2. The resulting branching

Fit variables	Sample fraction				
	$K_{2\pi}$	$K_{\mu 3}$	K_{e3}	$K_{3\pi^0}$	$K_{3\pi}$
Simulation prediction	0.75563	0.10421	0.10539	0.03467	0.00010
$m^2_{miss}(\pi)$ v $m^2_{miss}(\pi+\pi^0)$	0.7582(45)	0.10740(24)	0.10092(24)	0.03340(6)	0.00010(f)
$m^2_{miss}(\pi)$ v $m^2_{miss}(\mu+\pi^0)$	0.75684(43)	0.10503(16)	0.10471(16)	0.03329(6)	0.00010(f)
$m^2_{miss}(\pi)$ v $m^2_{miss}(e+\pi^0)$	0.75643(46)	0.10488(17)	0.10545(18)	0.03314(6)	0.00010(f)
$m^2_{miss}(\pi+\pi^0)$ v $m^2_{miss}(\mu+\pi^0)$	0.75501(46)	0.10639(15)	0.10510(14)	0.03341(6)	0.00010(f)
$m^2_{miss}(\pi+\pi^0)$ v $m^2_{miss}(e+\pi^0)$	0.75534(46)	0.10640(15)	0.10487(14)	0.03330(6)	0.00010(f)
$m^2_{miss}(\mu+\pi^0)$ v $m^2_{miss}(e+\pi^0)$	0.75482(46)	0.10667(15)	0.10503(15)	0.03338(6)	0.00010(f)

Table 6.4: Sample fractions as obtained from the K_{l3} fit on the nominal kaon data.

fractions ratios between the three channels of interest are given in table 6.5, where the assigned uncertainty comes only from the statistical error of the fit and the error on the acceptance.

Fit variables	Branching fraction ratios		
	$K_{\mu 3}/K_{2\pi}$	$K_{e3}/K_{2\pi}$	$K_{\mu 3}/K_{e3}$
PDG	0.1622(17)	0.2453(22)	0.6611(83)
$m^2_{miss}(\pi^+)$ v $m^2_{miss}(\pi^++\pi^0)$	0.1649(3)	0.2357(5)	0.6996(19)
$m^2_{miss}(\pi^+)$ v $m^2_{miss}(\mu^++\pi^0)$	0.1613(2)	0.2453(3)	0.6578(12)
$m^2_{miss}(\pi^+)$ v $m^2_{miss}(e^++\pi^0)$	0.1616(2)	0.2458(4)	0.6575(12)
$m^2_{miss}(\pi^++\pi^0)$ v $m^2_{miss}(\mu^++\pi^0)$	0.1612(2)	0.2436(3)	0.6615(11)
$m^2_{miss}(\pi^++\pi^0)$ v $m^2_{miss}(e^++\pi^0)$	0.1610(2)	0.2431(3)	0.6623(11)
$m^2_{miss}(\mu^++\pi^0)$ v $m^2_{miss}(e^++\pi^0)$	0.1615(2)	0.2438(3)	0.6624(11)

Table 6.5: Branching fraction ratios from the GTK data fit.

Fit variables	Branching fraction ratios		
	$K_{\mu 3}/K_{2\pi}$	$K_{e3}/K_{2\pi}$	$K_{\mu 3}/K_{e3}$
PDG	0.1622(17)	0.2453(22)	0.6611(83)
$m^2_{miss}(\pi^+)$ v $m^2_{miss}(\pi^++\pi^0)$	0.1666(4)	0.2341(6)	0.7116(24)
$m^2_{miss}(\pi^+)$ v $m^2_{miss}(\mu^++\pi^0)$	0.1632(3)	0.2434(4)	0.6705(16)
$m^2_{miss}(\pi^+)$ v $m^2_{miss}(e^++\pi^0)$	0.1630(3)	0.2452(5)	0.6650(17)
$m^2_{miss}(\pi^++\pi^0)$ v $m^2_{miss}(\mu^++\pi^0)$	0.1657(3)	0.2448(4)	0.6768(15)
$m^2_{miss}(\pi^++\pi^0)$ v $m^2_{miss}(e^++\pi^0)$	0.1656(3)	0.2442(4)	0.6783(15)
$m^2_{miss}(\mu^++\pi^0)$ v $m^2_{miss}(e^++\pi^0)$	0.1662(3)	0.2447(4)	0.6791(15)

Table 6.6: Branching fraction ratios from the nominal kaon data fit.

The branching fraction ratios from the fit using the GTK fit sample show good stability, in particular in the $m^2_{miss}(l^+{+}\pi^0)$ vs. $m^2_{miss}(l^+{+}\pi^0)$ configurations. The only significant deviation is in the result from $m^2_{miss}(\pi^+)$ vs. $m^2_{miss}(\pi^++\pi^0)$, which is likely due to a combination of the data/simulation disagreement and the reduced channel separation in that variable combination.

The stability of the branching fraction ratios from the nominal kaon sample is similar to that for the GTK results. As before, a deviation is seen in the result of the

$m^2_{miss}(\pi^+)$ vs. $m^2_{miss}(\pi^+ + \pi^0)$. There also appears to be a systematic effect, where the $BR(K_{\mu 3})/BR(K_{e3})$ ratio is significantly higher than the value from obtained from the GTK results. This effect is attributed to a misalignment in the missing-mass peaks for the nominal kaon sample. Figure 6.3 shows the $m^2_{miss}(\mu^+ + \pi^0)$ distribution zoomed in around zero for the nominal kaon and the GTK fit samples, where the difference in the agreement of position of the missing-mass peak can be seen. If the residual data/simulation shift in the missing-mass peaks is resolved, the nominal kaon fit is expected to be at a similar level in performance and results to the GTK.

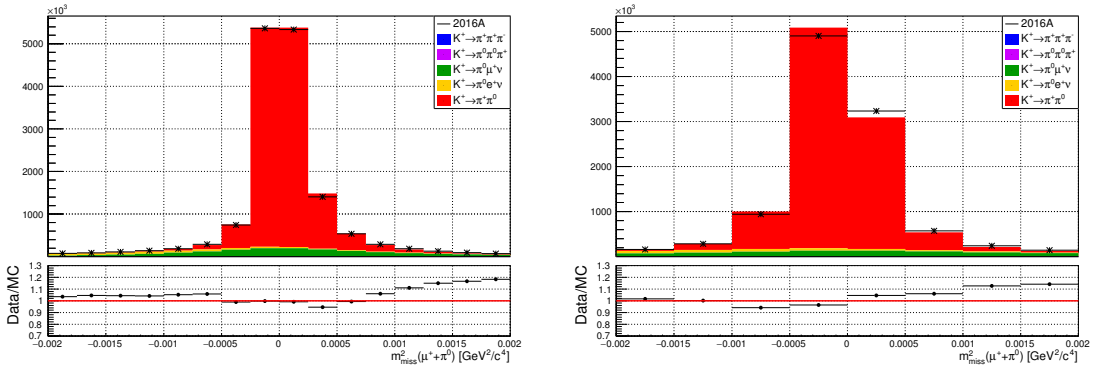

(a) $m^2_{miss}(\mu^+ + \pi^0)$, GTK

(b) $m^2_{miss}(\mu^+ + \pi^0)$, nominal kaon

Figure 6.3: Comparison of the GTK and nominal kaon $m^2_{miss}(\mu^+ + \pi^0)$ distributions used for the K_{l3} fit. A residual misalignment in the nominal kaon distribution is visible.

Considering this, the ratios obtained from the GTK $m^2_{miss}(\pi^+ + \pi^0)$ v $m^2_{miss}(e^+ + \pi^0)$ fit is taken as the measurement result, and used to study systematic effects. The covariance and correlation matrices of the $m^2_{miss}(\pi^+ + \pi^0)$ vs. $m^2_{miss}(e^+ + \pi^0)$ fit are given by equations 6.3 and 6.4 respectively.

$$
\begin{array}{c} \\ K_{2\pi} \\ K_{\mu 3} \\ K_{e3} \\ K_{3\pi^0} \end{array}
\begin{array}{c}
\begin{array}{cccc} K_{2\pi} & K_{\mu 3} & K_{e3} & K_{3\pi^0} \end{array} \\
\begin{pmatrix}
1.0278 \times 10^{-7} & -3.2006 \times 10^{-9} & -8.2325 \times 10^{-9} & -1.2211 \times 10^{-9} \\
-3.2006 \times 10^{-9} & 1.3012 \times 10^{-8} & -2.1249 \times 10^{-9} & 1.2491 \times 10^{-10} \\
-8.2325 \times 10^{-9} & -2.1249 \times 10^{-9} & 1.2555 \times 10^{-8} & -5.8346 \times 10^{-10} \\
-1.2211 \times 10^{-9} & 1.2491 \times 10^{-10} & -5.8346 \times 10^{-10} & 2.5037 \times 10^{-9}
\end{pmatrix}
\end{array}
\tag{6.3}
$$

$$\begin{array}{c} \\ K_{2\pi} \\ K_{\mu 3} \\ K_{e3} \\ K_{3\pi^0} \end{array} \begin{array}{c} \begin{array}{cccc} K_{2\pi} & K_{\mu 3} & K_{e3} & K_{3\pi^0} \end{array} \\ \begin{pmatrix} 1 & -0.08752 & -0.22918 & -0.076125 \\ -0.08752 & 1 & -0.16624 & 0.021884 \\ -0.22918 & -0.16624 & 1 & -0.10407 \\ -0.076125 & 0.021884 & -0.10407 & 1 \end{pmatrix} \end{array} \tag{6.4}$$

6.3 Systematic uncertainties

To estimate the systematic uncertainty in the result from the previous section, the fit was performed using simulation samples, omitting one of various corrections described in chapter 5. The difference between the ratios obtained with and without the correction is taken as the systematic uncertainty. The stability of the ratio with respect to the $K_{\mu 2}$ and m_{π^0} cuts is also studied by varying these cuts separately. Finally the contribution of the $K_{3\pi}$ fraction to the branching fraction ratios is investigated by performing without the $K_{3\pi}$ sample.

6.3.1 Pileup

To evaluate the systematic effect of the injection of pileup effects, the fit was performed on simulation samples where the rate of pileup events added was varied by $\pm\sqrt{\bar{\lambda}}$, where $\bar{\lambda}$ corresponds to the mean instantaneous intensity (280 MHz). The results of the fit with the modified simulation samples are listed in table 6.7.

Pileup rate [MHz]	Branching fraction ratios		
	$K_{\mu 3}/K_{2\pi}$	$K_{e3}/K_{2\pi}$	$K_{\mu 3}/K_{e3}$
263	0.1612(2)	0.2430(3)	0.6634(11)
280 (nom.)	0.1610(2)	0.2431(3)	0.6623(11)
297	0.1611(2)	0.2427(3)	0.6640(11)

Table 6.7: K_{l3} branching fraction ratios obtained using simulation samples with different rates of pileup events.

6.3.2 Kinematic smearing

The influence of the kinematic smearing is studied by removing the STRAW and GTK smearing one at a time, and performing the fit again. Table 6.8 shows the fit results ratios obtained without each of the track smearing.

Smearing parameters	Branching fraction ratios		
	$K_{\mu 3}/K_{2\pi}$	$K_{e3}/K_{2\pi}$	$K_{\mu 3}/K_{e3}$
$\sigma_{t_{\rm drift}} = 0$, $\alpha_{GTK} = 0.42$, $\beta_{GTK} = 0.0025$	0.1611(2)	0.2428(3)	0.6634(11)
$\sigma_{t_{\rm drift}} = 2.0$, $\alpha_{GTK} = 0$, $\beta_{GTK} = 0$	0.1612(2)	0.2435(3)	0.6621(11)
$\sigma_{t_{\rm drift}} = 2.0$, $\alpha_{GTK} = 0.42$, $\beta_{GTK} = 0.0025$ (nom.)	0.1610(2)	0.2431(3)	0.6623(11)

Table 6.8: K_{l3} branching fraction ratios obtained using simulation samples with different smearing configurations.

6.3.3 LKr cluster energy correction

The effect of the photon energy correction is estimated by considering the error of the m_{π^0} peak positions for $K_{2\pi}$ decays in data and simulation, since the calibration described in section 5.3.3 relies on those values. To estimate the systematic error of the m_{π^0} peak positions, the other three calibration samples, $K_{\mu 3}$, K_{e3}, and $K_{3\pi^0}$, are used. Table 6.9 shows the m_{π^0} peak position for the four calibration samples from data and simulation.

Calibration sample	m_{π^0} peak position [MeV/c^2]	
	Data	Simulation
$K_{2\pi}$	134.899(1)	134.956(2)
$K_{\mu 3}$	134.904(3)	135.006(3)
K_{e3}	134.932(4)	135.008(2)
$K_{3\pi^0}$	135.020(8)	135.075(3)

Table 6.9: The neutral pion mass peak positions for the four calibration samples in data and simulation.

Taking the $K_{2\pi}$ positions as the central values, the datasets in table 6.9 give a standard deviation of 0.072 MeV/c^2 for data, and 0.080 MeV/c^2 for simulation. Assigning these values as systematic error on the $K_{2\pi}$ m_{π^0} peak positions, and adding them in quadrature, gives an overall error on the m_{π^0} peak position of 0.108 MeV/c^2. This error can be converted to an error on photo energy scaling by using equation 5.8, as shown in equation 6.5.

$$\epsilon_{\gamma_E \text{scaling}} = 1 - \sqrt{\frac{m_{\pi^0}^{PDG}}{m_{\pi^0}^{PDG} + 0.108}} = 0.0004, \tag{6.5}$$

where $m_{\pi^0}^{PDG} = 134.977$ MeV/c^2.

To evaluate the systematic uncertainties on the branching fraction ratios, the branching fraction fit was performed with the simulation scaling factor from section 5.3.3, varied by ± 0.0004, with the results shown in table 6.10. For each ratio, the larger difference from the two alternate fits is taken as the systematic uncertainty.

Simulation E_γ scaling	Branching fraction ratios		
	$K_{\mu 3}/K_{2\pi}$	$K_{e3}/K_{2\pi}$	$K_{\mu 3}/K_{e3}$
0.9951	0.1606(2)	0.2436(3)	0.6594(12)
0.9955 (nom.)	0.1610(2)	0.2431(3)	0.6623(11)
0.9959	0.1613(2)	0.2431(3)	0.6652(12)

Table 6.10: K_{l3} branching fraction ratios obtained using a simulation photon energy scaling varied by its error.

6.3.4 $K_{\mu 2}$ cut

In order to measure the influence of the $K_{\mu 2}$ cut, $|m^2_{miss}(\mu^+)| > 0.005$ GeV^2/c^4, on the branching fraction ratios, the measurement was repeated with two different cut values, 0.003 and 0.007, corresponding to $\pm 2\sigma$ of the $m^2_{miss}(\mu^+)$ resolution, which is around 1×10^{-3} GeV^2/c^4. Table shows the branching fraction ratios obtained with the lower and higher $K_{\mu 2}$ cut. The larger difference in the ratios between the higher/lower cut and the nominal one is taken as the systematic uncertainty.

$m^2_{miss}(\mu)$ cut [GeV^2/c^4]	Branching fraction ratios		
	$K_{\mu 3}/K_{2\pi}$	$K_{e3}/K_{2\pi}$	$K_{\mu 3}/K_{e3}$
0.003	0.1601(2)	0.2431(3)	0.6623(12)
0.005 (nom.)	0.1610(2)	0.2431(3)	0.6623(11)
0.007	0.1610(2)	0.2432(3)	0.6622(12)

Table 6.11: K_{l3} branching fraction ratios obtain using a looser and a tighter $K_{\mu 2}$ cut.

6.3.5 m_{π^0} cut

The m_{π^0} cut was varied by $\pm 2\sigma_{m_{\pi^0}}$, where the resolution of the neutral pion mass was measured to be around 2 MeV/c^2. A conservative estimate of the effect of the m_{π^0} cut is obtained by varying the cut by $\pm 2\sigma$. The K_{l3} ratios with the modified m_{π^0} cut are listed in table 6.12. As before, the larger ratio difference from the two cut values is taken as the systematic uncertainty.

m_{π^0} cut [MeV/c^2]	Branching fraction ratios		
	$K_{\mu 3}/K_{2\pi}$	$K_{e3}/K_{2\pi}$	$K_{\mu 3}/K_{e3}$
6	0.1609(2)	0.2427(3)	0.6630(11)
10 (nom.)	0.1610(2)	0.2431(3)	0.6623(11)
14	0.1609(2)	0.2431(3)	0.6617(11)

Table 6.12: K_{l3} branching fraction ratios obtained using the modified neutral pion mass cut.

6.3.6 $K_{3\pi}$ fraction

To study the effect of fixing the $K_{3\pi}$ fraction on the K_{l3} ratios, the fit was performed with the $K_{3\pi}$ excluded. The ratios without $K_{3\pi}$ are shown in table 6.13.

$K_{3\pi}$ inclusion	Branching fraction ratios		
	$K_{\mu 3}/K_{2\pi}$	$K_{e3}/K_{2\pi}$	$K_{\mu 3}/K_{e3}$
With $K_{3\pi}$ (nom.)	0.1610(2)	0.2431(3)	0.6623(11)
No $K_{3\pi}$	0.1610(2)	0.2431(3)	0.6623(11)

Table 6.13: K_{l3} branching fraction ratios obtained with and without including the $K_{3\pi}$ sample.

6.3.7 Summary

Table 6.14 lists the statistical and systematic contributions to the uncertainties of the K_{l3} branching ratios. The two dominating effects are the simulated rate of pileup, and the E_γ scaling. Both of these effects directly impact the level of the data/simulation agreement discussed in section 5.3. This highlights the importance of good data/simulation agreement to the fraction fit technique used for the analysis. The rest of the systematic effects are at the level of the statistical uncertainty, where the K_{l3} ratios appear to be stable with respect to simulation smearing parameters and cut variations.

Systematic errors dominate the uncertainty on the branching fraction ratios, being around three times larger than the statistical uncertainty. Improvements to the LKr energy calibration, i.e. the introduction of run-by-run fine data calibration, and a more accurate pileup simulation, are both forthcoming due NA62 collaboration-wide effort. These improvements are expected to reduce the disagreements seen between data and simulation, and reduce effect of the two dominating systematic errors. In such a scenario, other systematic effects become important, and would warrant study.

Two such effects are the accuracy of the radiative corrections, and the values of the form factors used to generate the simulation samples. These effects enter into the analysis via the missing-mass distributions, and sample acceptances. The two effects can be studied by either generating new simulation samples, or reweighing existing ones based on the simulation truth information. Additional contributions to the systematic uncertainty may arise from different trigger efficiencies or random vetoes for the different decay modes studied, however these effects are not expected to be large.

	Branching fraction ratios		
	$K_{\mu 3}/K_{2\pi}$	$K_{e3}/K_{2\pi}$	$K_{\mu 3}/K_{e3}$
Central values	0.1610	0.2431	0.6623
Statistical uncertainties	0.0002	0.0003	0.0011
Systematic uncertainties			
Pileup rate	0.0002	0.0004	0.0017
STRAW smearing	0.0001	0.0003	0.0011
GTK smearing	0.0002	0.0004	0.0002
E_γ scaling	0.0004	0.0005	0.0029
$K_{\mu 2}$ cut	0.0009	<0.0001	0.0001
m_{π^0} cut	0.0001	0.0004	0.0007
$K_{3\pi}$ contribution	<0.0001	<0.0001	<0.0001
Total systematic uncertainty	0.0010	0.0009	0.0036
Total uncertainty	0.0011	0.0010	0.0038

Table 6.14: The different contributions and the overall uncertainty of the K_{l3} branching fraction measurement.

6.4 Comparison with previous results

The K_{l3} branching fraction ratios obtained in this measurement are listed in table 6.15 together with the most precise recent measurement, which is from the NA48/2 experiment [47] [48], and the current values from the PDG [7]. The current measurement improves on the statistical precision of the previous measurement by a factor of three. The systematic uncertainties of this analysis are however, around two to four times larger than those of NA48/2, showcasing the fact, already discussed in section 6.3.7, that this measurement is limited by systematic effects. The expected improvements in systematic errors, detailed in section 6.3.7, combined with the low statistical errors in table 6.14, suggest, that the ratios presented here can improve on the precision of previous results.

Measurement	Branching fraction ratios		
	$K_{\mu 3}/K_{2\pi}$	$K_{e3}/K_{2\pi}$	$K_{\mu 3}/K_{e3}$
Current	$0.1610(2)_{\text{stat}}(10)_{\text{sys}}$	$0.2431(3)_{\text{stat}}(9)_{\text{sys}}$	$0.662(1)_{\text{stat}}(4)_{\text{sys}}$
NA48/2	$0.1637(6)_{\text{stat}}(3)_{\text{sys}}$	$0.2470(9)_{\text{stat}}(4)_{\text{syst}}$	$0.663(3)_{\text{stat}}(1)_{\text{sys}}$
PDG	0.1622(17)	0.2453(22)	0.661(8)

Table 6.15: Comparison of the current K_{l3} branching fraction ratios with previous measurements.

Chapter 7

Conclusions

Several hardware interlocks critical to the safe H_2 operation of the NA62 CEDAR were implemented, interfacing dry contact signals into the relevant CEDAR control circuits. These interlocks reduce the risk of explosion in case of an H_2 leak by shutting down electrical equipment in the vicinity of the detector. A visualisation of the interlock states was added to the KTAG detector control system, allowing monitoring of the interlock status by the NA62 shift crew. With these newly implemented safeguards, the danger arising from operating the CEDAR with H_2 are mitigated to a safe level.

Using the CEDAR with hydrogen, rather than N_2 would reduce the amount of material the beam travels through, and therefore the background rate on downstream detectors. The contribution of the nitrogen inside the CEDAR towards the downstream detector rate was found to be comparable to the contribution of beam related effects, such as tuning, which vary with the normal data taking conditions of the experiment. Filling the CEDAR with H_2 in its current optical configuration is likely to degrade its performance in its role of tagging kaons with 100 ps time resolution. A reduced kaon tagging efficiency and worse time resolution may well cancel out any benefits brought about by a reduction in the downstream detector rates. Therefore, the current CEDAR will not be used with H_2, instead another CEDAR will adapted for H_2 operation, allowing NA62 to take data with the current CEDAR filled with N_2.

The ratios between the K_{l3} branching fractions were measured to be:

$$\frac{BF(K_{\mu 3})}{BF(K_{2\pi})} = 0.1610(2)_{\text{stat}}(10)_{\text{sys}}$$

$$\frac{BF(K_{e3})}{BF(K_{2\pi})} = 0.2431(3)_{\text{stat}}(9)_{\text{sys}}$$

$$\frac{BF(K_{\mu 3})}{BF(K_{e3})} = 0.6623(11)_{\text{stat}}(36)_{\text{sys}}$$

The statistical uncertainty of the ratios improves on previous measurements, demonstrating the power of the Barlow-Beeston method combined with the NA62 dataset and simulation. The structuring of the analysis allows for the measurement to be performed with or without the GTK, where both techniques have shown to be viable. The reported K_{l3} measurement used the GTK. The precision of the measurement is presently limited by the systematic uncertainty which stems mainly from data/simulation differences in the calibration of the LKr, and the simulation of pileup. Further focus and effort in these areas from the NA62 collaboration should allow a reduction of the systematic effects, making the measurement competitive with previous results.

Bibliography

[1] Y. Fukuda *et al.*, "Evidence for oscillation of atmospheric neutrinos," *Phys. Rev. Lett.*, vol. 81, pp. 1562–1567, 1998.

[2] Q. R. Ahmad *et al.*, "Direct evidence for neutrino flavor transformation from neutral current interactions in the Sudbury Neutrino Observatory," *Phys. Rev. Lett.*, vol. 89, p. 011301, 2002.

[3] L. Canetti, M. Drewes, and M. Shaposhnikov, "Matter and Antimatter in the Universe," *New J. Phys.*, vol. 14, p. 095012, 2012.

[4] A. D. Sakharov, "Violation of CP Invariance, C asymmetry, and baryon asymmetry of the universe," *Pisma Zh. Eksp. Teor. Fiz.*, vol. 5, pp. 32–35, 1967.

[5] M. Thomson, *Modern particle physics*. New York: Cambridge University Press, 2013.

[6] V. Cirigliano, J. P. Jenkins, and M. González-Alonso, "Semileptonic decays of light quarks beyond the standard model," *Nuclear Physics B*, vol. 830, no. 1, pp. 95 – 115, 2010.

[7] M. Tanabashi *et al.*, "Review of particle physics," *Phys. Rev. D*, vol. 98, p. 030001, Aug 2018.

[8] M. Antonelli *et al.*, "An Evaluation of $|V_{us}|$ and precise tests of the Standard Model from world data on leptonic and semileptonic kaon decays," *Eur. Phys. J.*, vol. C69, pp. 399–424, 2010.

[9] M. Moulson, "Experimental determination of V_{us} from kaon decays," in *8th International Workshop on the CKM Unitarity Triangle (CKM 2014) Vienna, Austria, September 8-12, 2014*, 2014.

[10] S Towner, I and C Hardy, J, "The evaluation of V_{ud} and its impact on the unitarity of the Cabibbo–Kobayashi–Maskawa quark-mixing matrix," *Reports on Progress in Physics*, vol. 73, p. 046301, 03 2010.

[11] M. Moulson, "Experimental determination of V_{us} from kaon decays," *PoS*, vol. CKM2016, p. 033, 2017.

[12] S. Aoki *et al.*, "Review of lattice results concerning low-energy particle physics," *Eur. Phys. J.*, vol. C77, no. 2, p. 112, 2017.

[13] L. Maiani, G. Pancheri, and N. Paver, eds., *The second DAPHNE physics handbook. Vol. 1, 2.* Frascati, Italy: INFN, 1995.

[14] C. Lazzeroni *et al.*, "Measurement of the form factors of charged kaon semileptonic decays," *JHEP*, vol. 10, p. 150, 2018.

[15] J. Gasser and H. Leutwyler, "Chiral perturbation theory: Expansions in the mass of the strange quark," *Nuclear Physics B*, vol. 250, no. 1, pp. 465 – 516, 1985.

[16] V. Cirigliano, M. Giannotti, and H. Neufeld, "Electromagnetic effects in K_{l3} decays," *Journal of High Energy Physics*, vol. 2008, pp. 006–006, nov 2008.

[17] A. Sirlin, "Large m(W), m(Z) Behavior of the O(α) Corrections to Semileptonic Processes Mediated by W," *Nucl. Phys.*, vol. B196, pp. 83–92, 1982.

[18] G. Anelli *et al.*, "Proposal to measure the rare decay $K^+ \to \pi^+\nu\nu$ at the CERN SPS," 2005.

[19] A. J. Buras, D. Buttazzo, J. Girrbach-Noe, and R. Knegjens, "$K^+ \to \pi^+\nu\nu$ and $K_L \to \pi^0\nu\nu$ in the Standard Model: status and perspectives," *JHEP*, vol. 11, p. 033, 2015.

[20] A. V. Artamonov *et al.*, "Study of the decay $K^+ \to \pi^+\nu\nu$ in the momentum region $140 < P_\pi < 199$ MeV/c," *Phys. Rev.*, vol. D79, p. 092004, 2009.

[21] E. Cortina Gil *et al.*, "The Beam and detector of the NA62 experiment at CERN," *JINST*, vol. 12, no. 05, p. P05025, 2017.

[22] C. Bovet, R. Maleyran, L. Piemontese, A. Placci, and M. Placidi, "The Cedar Counters for Particle Identification in the SPS Secondary Beams: A Description and an Operation Manual," 1982.

[23] P. A. Čerenkov, "Visible radiation produced by electrons moving in a medium with velocities exceeding that of light," *Phys. Rev.*, vol. 52, pp. 378–379, Aug 1937.

[24] E. Goudzovski *et al.*, "Development of the kaon tagging system for the NA62 experiment at CERN," *Nucl. Instrum. Meth.*, vol. A801, pp. 86–94, 2015.

[25] P. Golonka, V. Falaleev, R. Fantechi, M. Gonzalez-Berges, N. Lurkin, R. Page, and F. Varela, "Detector and Run Control Systems for the NA62 Fixed-Target Experiment at CERN," in *Proceedings, 15th International Conference on Accelerator and Large Experimental Physics Control Systems (ICALEPCS 2015): Melbourne, Australia, October 17-23, 2015*, p. MOPGF020, 2015.

[26] Siemens AG, "SIMATIC WinCC Open Architecture." `https://w3.siemens.com/mcms/human-machine-interface/en/visualization-software/simatic-wincc-open-architecture/pages/default.aspx`. Accessed: 2019-08-25.

[27] O. Holme, M. Gonzalez-Berges, P. Golonka, and S. Schmeling, "The JCOP framework," *Conf. Proc. C051010:WE*, vol. 2, 01 2005.

[28] CAEN, "SY 4527 power supplies." `https://www.caen.it/products/sy4527/`. Accessed: 2019-09-18.

[29] Aim-TTi, "PL series manual." `http://resources.aimtti.com/manuals/New_PL+PL-P_Series_Instruction_Manual-Iss18.pdf`. Accessed: 2019-09-18.

[30] The European Parliament and the Council of the European Union, "ATEX Directive 2014/34/EU." `https://eur-lex.europa.eu/legal-content/EN/TXT/?uri=CELEX:32014L0034`. Accessed: 2019-09-18.

[31] Pepperl+Fuchs AG, "Manual Zener Barriers Z-System." `https://files.pepperl-fuchs.com/webcat/navi/productInfo/doct/tdoct0185j_eng.pdf?v=20160302160136`. Accessed: 2019-09-18.

[32] V. Agoritsas, "A sealed metal argon ionization chamber (argonion)," *IEEE Transactions on Nuclear Science*, vol. 28, pp. 2243–2245, June 1981.

[33] R. Barlow and C. Beeston, "Fitting using finite monte carlo samples," *Computer Physics Communications*, vol. 77, no. 2, pp. 219 – 228, 1993.

[34] NA62 Collaboration, "SpectrometerCHODAssociation Class Reference." `https://na62-sw.web.cern.ch/sites/na62-sw.web.cern.ch/files/doxygen/d9/d99/classSpectrometerCHODAssociation.html`. Accessed: 2019-09-19.

[35] NA62 Collaboration, "SpectrometerNewCHODAssociation Class Reference." `https://na62-sw.web.cern.ch/sites/na62-sw.web.cern.ch/files/doxygen/d3/d13/classSpectrometerNewCHODAssociation.html`. Accessed: 2019-09-19.

[36] NA62 Collaboration, "SpectrometerCalorimetersAssociation Class Reference." `https://na62-sw.web.cern.ch/sites/na62-sw.web.cern.ch/files/doxygen/d7/d64/classSpectrometerCalorimetersAssociation.html`. Accessed: 2019-09-19.

[37] R. Marchevski, *First measurement of the $K^+ \to \pi^+\nu\nu$ decay with the NA62 experiment at CERN*. PhD thesis, Johannes Gutenberg-Universit"at Mainz, Mainz, 2018.

[38] NA62 Collaboration, "BeamParameters Class Reference." `https://na62-sw.web.cern.ch/sites/na62-sw.web.cern.ch/files/doxygen/db/d45/classBeamParameters.html`. Accessed: 2019-09-19.

[39] F. Filthaut and B. Wijngaarden, "TFractionFitter." `https://root.cern.ch/doc/v606/classTFractionFitter.html`. Accessed: 2019-09-18.

[40] R. Brun and F. Rademakers, "ROOT: An object oriented data analysis framework," *Nucl. Instrum. Meth.*, vol. A389, pp. 81–86, 1997.

[41] NA62, Collaboration, "2017 NA62 status report to the CERN SPSC," Tech. Rep. CERN-SPSC-2017-013. SPSC-SR-208, CERN, Geneva, Mar 2017.

[42] D. C. Carey, "TURTLE (trace unlimited rays through lumped elements) : A Computer program for simulating charged particle beam transport systems," 1971.

[43] S. Agostinelli *et al.*, "Geant4—a simulation toolkit," *Nuclear Instruments and Methods in Physics Research Section A: Accelerators, Spectrometers, Detectors and Associated Equipment*, vol. 506, no. 3, pp. 250 – 303, 2003.

[44] C. Gatti, "Monte Carlo simulation for radiative kaon decays," *Eur. Phys. J.*, vol. C45, pp. 417–420, 2006.

[45] NA62 Collaboration, "NA62 software." `https://na62-sw.web.cern.ch/software`. Accessed: 2019-09-18.

[46] NA62 Collaboration, "SpectrometerMUV3Association Class Reference." `https://na62-sw.web.cern.ch/sites/na62-sw.web.cern.ch/files/doxygen/dc/deb/classSpectrometerMUV3Association.html`. Accessed: 2019-09-19.

[47] J. Batley *et al.*, "Measurements of charged kaon semileptonic decay branching fractions $K^{\pm} \to \pi^0 \mu^{\pm} \nu$ and $K^{\pm} \to \pi^0 e^{\pm} \nu$ and their ratio," *The European Physical Journal C*, vol. 50, pp. 329–340, Apr 2007.

[48] J. Batley *et al.*, "Measurements of charged kaon semileptonic decay branching fractions $K^{\pm} \to \pi^0 \mu^{\pm} \nu$ and $K\pm \to \pi^0 e^{\pm} \nu$ and their ratio," *The European Physical Journal C*, vol. 52, pp. 1021–1023, Dec 2007.